Doctoral Dissertation
Doctoral Program in Chemical Engineering (38thcycle)

Multiscale computational and theoretical modeling of electrochemical processes in lithium-ion batteries

By

Alessio Lombardo Pontillo

******

Supervisor(s):
Prof. Daniele Marchisio, Supervisor
Prof. Gianluca Boccardo, Co-Supervisor
Prof. Antonio Buffo, Co-Supervisor

Doctoral Examination Committee:
Prof. Matteo Icardi , Referee, University of Nottingham
Prof. Ferran Brosa Planella, Referee, University of Warwick

Politecnico di Torino
2026

Declaration

I hereby declare that, the contents and organization of this dissertation constitute my own original work and does not compromise in any way the rights of third parties, including those relating to the security of personal data.

Alessio Lombardo Pontillo
2026

* This dissertation is presented in partial fulfillment of the requirements for **Ph.D. degree** in the Graduate School of Politecnico di Torino (ScuDo).

Abstract

Lithium-ion batteries (LIBs) are the backbone of today's portable electronics, electric mobility and grid integration thanks to intercalation chemistries supplanting metallic-lithium anodes. However, accelerating innovation is hampered by costly, material-intensive experimentation and by models that either oversimplify electrode morphology or are too slow for decision-making. This thesis addresses both challenges by (i) building a high-fidelity, pore-scale 4D model (3D in space + time) that resolves morphology-induced heterogeneity of concentration and potential; and (ii) deriving a fast, physics-based surrogate via rigorous homogenization to predict charge–discharge behavior with quantified accuracy. The most employed computational model for charge-discharge simulation of LIBs is the so called pseudo-2D Doyle–Fuller–Newman (P2D/DFN) framework, which assumes monodisperse spherical particles and lateral uniformity. While effective for long cycling, this approximation is inadequate for graphite anodes: their flake-like, anisotropic microstructure alters transport pathways, reaction surface availability, and local overpotentials. To capture these effects, we developed an automated workflow that automatically generates pore-scale COMSOL Multiphysics models through the Java API. All geometric and physicochemical inputs, such as particle positions, size distributions, anisotropic diffusion, kinetics and electrolyte properties, are supplied via human- and machine-readable text files, enabling rapid, reproducible campaign design and large-scale dataset creation. We employed this script to construct three anode morphologies of increasing realism: monodisperse spheres, polydisperse spheres, and polydisperse triaxial ellipsoids. This last kind of geometrical representation was selected to approximate the flat morphology of graphite while preserving credible inter-particle contacts. Transient simulations resolved the coupled mass and charge transport in solid and liquid phases with Butler-Volmer boundary condition enforced on the solid–electrolyte interfaces. We quantified intra-particle lithiation patterns, pore-scale concentration gradients, and the resulting voltage response. Discharge curves and morphological quantities were compared with experimental data, demonstrating that the three system generated were similar enough to be compared. We concluded that ellipsoidal ensembles reproduce spatial heterogeneity and effective kinetics more faithfully than sphere-based models, highlighting the sensitivity of performance to porosity and particle size dispersion. Second, to enable near-real-time inference without sacrificing morphological insight, we searched for a an accurate model, that can deliver the requested response in few seconds. Therefore we decided to adopt homogenization via multiple-scale asymptotic expansion to derive macroscopic equations for coupling diffusion–electromigration–reaction with a rigorous mathematical framework. Under standard LIB scale separation (pore size ℓ « electrode thickness L) and periodicity assumptions, we obtained closed-form cell-scale balances augmented by morphology-dependent effective transport tensors. Boundary conditions at the current collectors were included explicitly, obtaining a mathematical relationship that links micro-scale geometry, represented by the geometrical scale parameter $\varepsilon = \ell/L$, to macro-scale operating conditions, expressed by the external applied electric current density. The upscaled model has been verified against pore-scale simulations for concentration and voltage, and we mapped applicability regimes and error estimation in terms of the geometrical scale parameter ε. Within these regimes the reduced-order predictive model well reproduces full-order dynamics at a fraction of the cost, with a designable control over the error, supporting in-line estimation tasks such as state-of-health tracking where latencies of seconds are required.

Contents

List of Figures

List of Tables

Nomenclature

$(.)^{\ell}$	Referred to liquid phase
$(.)^{s}$	Referred to solid phase
$(.)_{\mathrm{P}}$	Referred to a solid particle
$(.)_{\mathrm{a}}$	Referred to anode side
$(.)_{\mathrm{cc}}$	Referred to current collector
$(.)_{\mathrm{c}}$	Referred to cathode side
$(.)_{\mathrm{max}}$	Maximum value considered
$(.)_{\mathrm{min}}$	Minimum value considered
$(.)_{\mathrm{ref}}$	Reference value
$(.)_{0}$	Initial condition
$(.)_{x\%}$	Referred to $x\%$ of the state of charge
A	Surface area
F	Faraday constant
R	Ideal gas constant
T	Temperature
V	Volume
ϕ	Electric potential

c	Concentration
$\mathbf{D}$	Diffusion coefficient
$\mathbf{K}$	Electrical conductivity
i	Electric current
M	Molar mass
η	Overpotential
$f_{\pm}$	Mean molar activity
m	Mass
t	time
t_{+}	Lithium-ion transference number
$\mathbf{F}$	Force
$\mathbf{I}$	Inertia
$\mathbf{g}$	Gravitational acceleration
$\mathbf{x}$	Spatial position
E	Young module
d	Distance
r	Radius
ω	Angular velocity
L	Characteristic cell-scale length
ε	Scale parameter
l	Characteristic pore-scale length
Da	Damköhler number
N_{ohm}	dimensionless IR-drop number
Pe	electric Peĺet number

Acronyms

AR Aspect Ratio. 40, 41

BCC Body Centered Cubic. 46, 58

BPL Bullet Physics Library. 14

DEM Discrete Element Method. 8, 39, 40

DFN Doyle–Fuller–Newman. 2

DoF Degree of Freedom. 32, 34

FEM Finite Element Method. 8, 29–34

FESEM Field Emission Scanning Electron Microscopy. vii, 3, 36, 38, 40, 45, 51, 52, 66

GITT Galvanostatic Intermittent Titration Technique. vii, 37, 38

LiB Lithium-ion Battery. vii, 1, 2, 4, 6–10, 16, 20, 24, 67, 69, 104

PDE Partial Differential Equation. 25, 30, 31

PSD Particle Size Distribution. vii, 6, 39–41, 51

REV Representative Elementary Volume. viii, 46

RL Refinement Level. 43, 45

SEI Solid Electrolyte Interphase. 57, 68

SoC	State of Charge. vii, 2, 8, 9, 13, 37, 38, 68
SoH	State of Health. 2, 6

Chapter 1

Introduction

The demand for lightweight, high-energy rechargeable batteries led to the development of lithium-based electrochemical systems in the 1970s. Early attempts using metallic lithium anodes offered high capacity but suffered from several safety issues. A major breakthrough was achieved with the introduction of intercalation electrodes: M.S. Whittingham proposed titanium disulfide as a cathode material [1], J.B. Goodenough demonstrated lithium cobalt oxide as a high-voltage cathode [2], and A. Yoshino introduced a carbonaceous anode to replace metallic lithium [3]. These advances culminated in Sony's commercialization of the first lithium-ion rechargeable battery in 1991 and in the recent Nobel prize for the three researchers in 2019 [4]. Since then, lithium-ion batteries have become the state-of-the-art energy storage technology, enabling the rapid expansion of portable electronics, electric mobility, and renewable energy integration. Nowadays, LiB are currently the dominant electric energy storage system adopted at all scales: from portable electronic devices to urban and aerospace vehicles, and likely they will play a major role in the construction of net zero energy buildings. Studies have predicted an increase of approximately 27% per year until 2030 in the global battery demand [5–7]. Compared with alternative battery technologies, Li-ion batteries provide an excellent energy-to-weight ratios and experience low self-discharge when not in use. These properties have established Li-ion batteries as a leading candidate for the next generation of non-fossil fuel-powered systems [8]. The design of Li-ion batteries has been primarily based on (1) matching the capacity of anode and cathode materials to find the best material combination, (2) trial-and-error investigation of thickness, porosity, active materials, electrolyte, and additive loading, (3) manufacturing convenience and cost, (4) detailed microscopic models to understand, optimize, and design these systems [9–11]. However, experimental tests, which include assembling, forming, and cycling of batteries, require an enormous amount of materials with a non-negligible cost. Recent studies had estimated that in the total price of a battery cell, materials account for about 47% [12] and this could be a huge limitation for the experimental exploration of the phenomena involved in LiB. To avoid this problem, the solution is a good and accurate planning of the experimental campaign in order to minimize the waste of materials and time as well. In this context, the use of computational tools has become increasingly important. Computational models for LiBs offer enormous support in the design of experiments, in studying complex phenomena, not observable with classical experiments [13], for in-line monitoring, and State of Health (SoH) prediction. The use of these models ensures a saving in time and resources by minimizing experiments, and reduce battery aging with a real-time measurement of the State of Charge (SoC) which is fundamental at all scales of energy storage. They are multiscale-multiphysics models [14] because the macroscopic behavior at the cell scale of a variable of interest, like lithium concentration and electric potential in both liquid and solid phases, is strongly influenced by the microscopic behavior that acts at the pore-scale [15]. Furthermore, several physics principles are involved in LiB models since the solution of mass, charge, and thermal transport is required[16, 17]. Unfortunately, often these models are too simple or require a long amount of time, which can span between minutes or hours, to obtain a solution. They rely on a reduced-order description (e.g. one-dimensional in the collector-separator direction) of the electrochemical behavior in the electrode, justified by the assumption that the behavior in the other two dimensions is uniform. One of the models that follows this assumption is the Doyle–Fuller–Newman (DFN) model [18, 19]. The DFN model solves a set of non-linear partial differential equations that describe the mass and charge transport in the solid (i.e. electrode particles) and liquid (i.e. electrolyte) phases. An extension of the Newman model is its homogenized version, the pseudo-2D model, and in which all electrode particles are considered spheres of the same size (i.e. monodisperse) [18, 20], neglecting the complex and rich heterogeneity characterizing by real electrodes, constituted by polydisperse non-spherical particles. In fact, batteries often exhibit a non-uniform behavior in the current distribution, with local heterogeneities which can adversely affect battery performance and lifetime. As mentioned, one of the aspects that is the most responsible for this non-uniformity is the electrode morphology [21].The P2D

(DFN) framework is excellent for simulating long sequences of charge–discharge cycles and capturing long-term trends. By contrast, its simplifying assumptions lead to unavoidable uncertainties when used for first-cycle optimization where formation, wetting, and parameter transients dominate; it is also typically too slow to support in-line monitoring or control across both the initial formation and the aging process. Motivated by this observation, we pursued two complementary goals: (1) to develop a high-fidelity 4D model (3D in space + time) that resolves morphology-induced, local variations in concentration; and (ii) to derive a fast, physics-based surrogate that predicts charge–discharge behavior within seconds without overly simplifying the electrode microstructure.

Starting from point (i), we note that the P2D model's assumption of isotropic, spherical particles may be reasonable for some cathodes (e.g., NMC), but it is not appropriate for graphite anodes, whose platelet-like morphology and strongly anisotropic transport violate this approximation. This carbon form, which is the most stable one, is an anisotropic material, as atoms are arranged in a hexagonal pattern forming a layered structure [22], with the valence electrons thus free to move within the carbon layers, being therefore able to conduct electricity [23]. Due to their layered structure, the graphite particles are flake-shaped, with one characteristic dimension smaller than the other two, as shown in the Field Emission Scanning Electron Microscopy (FESEM) image reported in Figure 1.1.

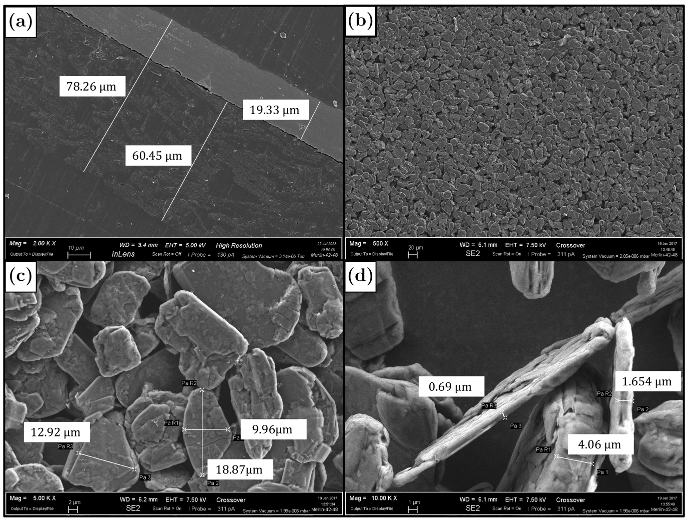

Fig. 1.1 a) FESEM image of an electrode of a half cell: graphite and separator; b) FESEM image of a graphite layer. c) Zoomed FESEM image of a graphite layer. d) FESEM image of a graphite particle.

For this material the spherical shape is therefore a strong approximation and very far from the real form of graphite flakes, and is nonetheless still widely used in literature [24–26]. Furthermore, [27] recently concluded that a correct representation of an *in-silico* electrode geometry, to be used in computational models, has a great impact on the intra-particle lithiation prediction. Nowadays, electrode morphology is one of the most studied aspects to improve the performances of LiBs [28–32] but this analysis often requires complex coding when performed with computational modelling means, or expensive experimental tools.

These reasons well delineate the challenge of this dissertation's work, whose focus firstly lies in trying to build more accurate models for describing the chemical and electrochemical transport at the pore-scale, with an emphasis on an accurate description of the active material at the forefront. This objective quickly led to the difficulty previously identified, namely that manual efforts in building non-standard (e.g.: uniform-spheres models) heterogeneous models are complex, costly, and ultimately impractical in the repeated testing campaigns necessary for manufacturing design optimization. This then in turn, led to the decision of tackling this issue by means of developing an automatic script in Java for the generation of a pore-scale, three-dimensional (3D) transient computational model, also known as 4D model, of a LiB half-cell. The script interfaces with the software COMSOL Multiphysics 6.1 API and simplifies user input in setting up the simulation, gathering all relevant input parameters explicitly in text files. These input text files contain all the information needed to run the simulation, such as the position of the particles or the physicochemical properties of the material of interest. The use of this script has several advantages, especially in added flexibility for the user, such as being able to easily vary both the physical and geometric properties of the system, leading to easier automated data set creation. One example of the possibilities offered by this more flexible approach would be in allowing to study and treat the different existing types of graphite, having different physical properties, such as particle size distribution, equilibrium potential, and lithium diffusion coefficient inside the active material, among others. Beyond the physicochemical setup of the computational model, this process also makes it easier to represent different anode geometrical morphologies or electrodes with different physical behaviors. These, as it has been mentioned and will be shown later in the Results Chapter, are very impactful parameters on charge-discharge behavior, which could be expanded, by a suitable modification in the code developed in this study, to include other relevant mechanical phenomena during electrode formation, e.g.

cracking, particle rearrangement during packing, surface roughness changes, and so on. In this work, we used this script to produce, in an easy way, three different electrodes of increasing geometric complexity: one with monodisperse spheres, one with polydisperse spheres, and one with polydisperse ellipsoids. The rationale for these choices was led by the search for a geometric shape that could better represent graphite particles. The triaxial ellipsoidal shape was selected as the basic shape most closely similar to the realistic morphology, since other shapes with an oriented face, like a parallelepiped or a cylinder, would not correctly represent the contact points between the particles. An ellipsoid, the generalization of a sphere with three principal semi-axes, provides a convenient way to tune one axis with respect to the other two, mirroring the aspect-ratio variability observed in graphite particles. The pore-scale simulation of the charge-discharge dynamics in the cell involves the separate solution of the mass and charge transport equations in all the specified domains of the battery, and setting the boundary conditions on the actual solid-electrolyte domains interfaces. In the first part of this work three main domains, for a half cell, have been considered: the porous separator, the liquid electrolyte, and the anode electrode. At the pore scale, electrodes are characterized by a porous structure, as it has been widely observed in the literature by means of electron microscopy and X-ray tomography imaging analysis [33]. This means that solid (active material) and liquid (electrolyte) phases coexist, and their relative distribution is quantified by the porosity, which is defined as the liquid volume fraction in the electrode. The porous structure of the electrode is reproduced in-silico and then employed in the electrochemical simulations. The separator is considered an inert porous media filled by the electrolyte. Its function is to avoid the direct contact between anode and cathode active materials, that would lead to dangerous short circuits, but it permits the passage of lithium ions from one side to the other one [34, 35]. The active material particles are assumed to be ellipsoidal or spherical and different geometries have been tested here in order to investigate their effect on the overall cell performance. From this kind of analysis on the three systems, it is possible to demonstrate the importance of an accurate electrode geometrical representation and the flexibility of the code that we developed. To do so, we analyzed the intercalated lithium concentration within the particles and we compared also the discharge curves with experimental ones. The previously described model is well suited for first-cycle optimization, where high fidelity is required and and simulations with high runtimes, performed once (or a few times) off-line, are acceptable. However, its computational burden makes it unsuitable for real-time measurements: solver stiffness and the large state dimension lead to latencies on the order of minutes rather than seconds, preventing closed-loop, in-line use. For in-line monitoring, a tool must deliver SoH estimates within seconds while retaining essential morphological detail. Over-simplifying the electrode morphology (e.g., assuming isotropic spherical particles) can bias transport pathways, distort local overpotentials, and degrade SoH predictions—precisely when early detection matters. Therefore, we sought a model that combines near-real-time inference with morphology-aware physics, preserving predictive accuracy without resorting to coarse geometric abstractions. Up-scaling methods, such as volume averaging, homogenization, extensions to evolving micro-structures, thermodynamically consistent averaging, and renormalization group theory, serve to bridge the gap between pore-scale mechanisms and their continuum-level descriptions [36–39]. A growing body of research has focused on deriving macroscopic models systematically from microscale conservation laws [40]. This trend highlights the importance of validating reduced-order models and understanding how microscopic processes shape the macroscopic behavior of electrochemical systems [41–45]. However, to the best of our knowledge, there has not yet been a rigorous validation of these derived up-scaled equations for charge and mass transport in lithium-ion batteries, which include electro-migration, diffusion, and reaction. To do this, we apply the homogenization via multiple-scale expansion [40, 37, 45, 46]. This mathematical technique allows the derivation of macroscopic equations under two major hypotheses: the separation of scale and the periodicity of the domain of interest [47–49]. The first condition is well satisfied in LiBs since the characteristic dimension of the electrode pores is very low compared to the electrode dimension [50]. Also, the second condition is fulfilled since the Particle Size Distribution (PSD) is not too large and we can easily individuate a unit cell that well describes the morphology of the system [51]. In this work, we mathematically derived the macroscopic equations for LiBs, similarly to what has been done by ref. [45]. For completeness, we reproduce the derivation here and provide a clarified and corrected version of the steps, which streamlines the presentation and avoids potential ambiguities present in earlier accounts. Particularly, we adopted microscale equations for mass and charge transport in the electrolyte that are considered the actual state of the art for LiB modeling, and they differs from the ones of Arunachalam et al.[45]. Furthermore we tried to include the boundary conditions at the anodic and cathodic current collectors in the mathematical homogenization, since they have an influence in the applicability of the method. Subsequently, we tested the concentration, and obtained applicability ranges in which it is possible to employ these upscaled and simplified models, at much lower cost than pore-scale simulations, albeit with a comparable accuracy.

Finally, this thesis is structured in the following way: in the first part, chapter two, we have the theoretical background, divided in four parts. First, we introduce the pore-scale governing equations for transport of mass and charge in Lithium-ions batteries. Then we have a short look of the Discrete element method adopted to generate the active material layer. The third section is about the homogenization technique and it contains the Darcy's law derivation, as an example, and the application to LiBs equations. Finally, a short discussion about Finite Element Method closes the chapter. The third chapter contains the information to reproduce both the simulation and the experimental tests carried out to find the morphological and physical properties of the active material particles. The fourth chapter summarizes the results obtained from the pore scale simulation and the validation of the reduced order model. Finally, the fifth chapter concludes the thesis, discusses the results previously obtained, and proposes some futures perspectives.

Chapter 2

Theoretical Background

In the second chapter of the manuscript, the theoretical background is presented. This is divided in three parts: in the first one, the governing equations for mass and charge transport are presented; the second one describes the Discrete Element Method; the third one contains general information about the homogenization with a particular attention on the multiple-scale expansion variant; finally, the fourth section presents the Finite Element Method used to run the simulations.

2.1 Pore-scale modeling of lithium-ion batteries

The micro-scale 3D modeling of LiBs is centered on the local numerical solution of the charge and mass conservation of intercalated lithium and lithium ion respectively within the electrodes and the electrolyte. Figure 2.1 sketches the typical system modeled and lists the main governing equations. The domain is composed of a liquid electrolyte (yellow), the anode with its current collector (respectively, light gray particles and dark gray area), the cathode with its current collector (respectively, light orange particles and dark orange area), and the separator (central blue area). For clarity, we will refer to the generic solid phase, either anode or cathode, with the $(.)^s$ superscript; the liquid electrolyte will be indicated with the $(.)^\ell$ superscript; the anode and cathode will be represented, respectively, with the $(.)_a$ and $(.)_c$ subscripts; $(.)_{\mathrm{Li}}$ or $(.)_{\mathrm{Li}^+}$ will denote the lithium or the lithium ions; the current collector will be indicated with $(.)_{cc}$. Furthermore, we want to give some definitions that will appear several times in this manuscript. The first is the State of Charge (SoC) that is calculated as follows [52]:

$$\mathrm{SoC} = \frac{(1/V^s)\int_{V^s} c^s dV^s - c^s_{0\%}}{c^s_{100\%} - c^s_{0\%}}, \tag{2.1}$$

where V^s is the active material volume and $c^s_{100\%}$ and $c^s_{0\%}$ are the average intercalated lithium concentration at 100% and 0% SoC. From the mathematical definition, it is clear that the SoC goes from zero to unity. The second definition is the C-rate. In electrochemical systems, the exact current density is geometry-dependent and not readily comparable across cells. We therefore express currents as C-rates, which is a current normalized to cell capacity, to enable fair comparison. Therefore usually the C-rate is defined in relative terms, as the inverse time in hours in which a charge or discharge cycle is completed. Therefore, if we refer to a *C/20 discharge* we mean that the discharge was carried out with a current value such that the discharge was completed in 20 hours. From the C-rate, the current can be approximately calculated as follows:

$$i = c^s_{\max}(\mathrm{SoC}^s_{\max} - \mathrm{SoC}^s_{\min}) F V^s C_{rate}, \tag{2.2}$$

where $c^s_{\max}$ is the maximum intercalated concentration within the electrode, F is the Faraday constant and V^s is the active material volume. As shown by the figure, the

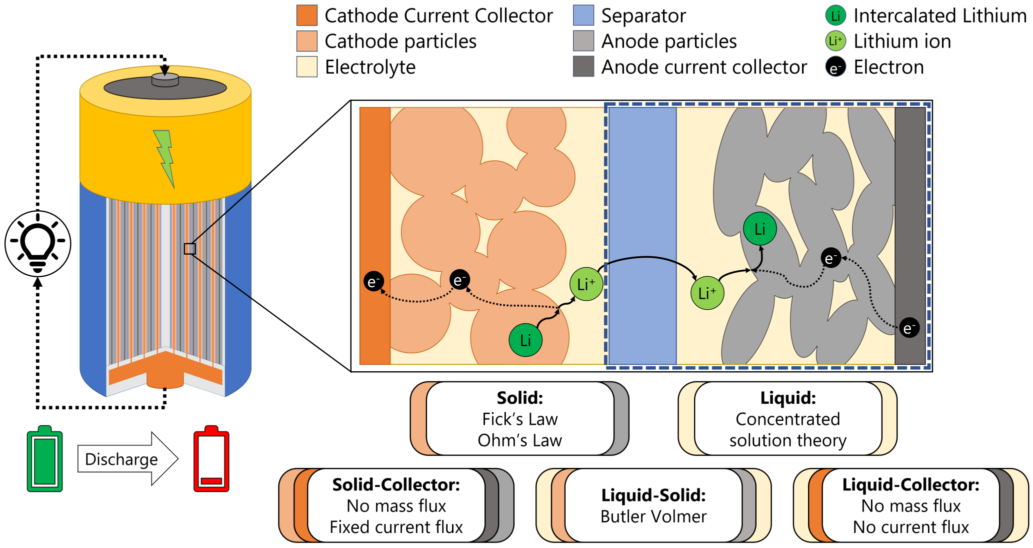

Fig. 2.1 Schematic representation of the LiB cell with the most relevant equations.

mass conservation in the solid phase is implemented through the steady state Fick's law, which describes the diffusion behavior of the intercalated lithium within the solid phases:

$$\frac{\partial c^s}{\partial t} = \nabla \cdot (\mathbf{D}^s \nabla c^s) \tag{2.3}$$

while the charge conservation is expressed through the Ohm law:

$$\nabla \cdot (\mathbf{K}^s \nabla \phi^s) = 0 \tag{2.4}$$

In Eq. 2.3 and 2.4 $\mathbf{K}^s$ is the electric conductivity coefficient in the electrode, ϕ^s is the electric potential, $\mathbf{D}^s$ is the diffusion coefficient in the electrode, and c^s is the intercalated lithium concentration. In parallel, the transport equations related to the charge and mass conservation of lithium ions in the electrolyte are solved by using concentrated solution theory [53] as:

$$\begin{aligned} &\frac{\partial c^\ell}{\partial t} = \\ &\nabla \cdot \left[\left(\mathbf{D}^\ell - \frac{2RT}{F^2} \left(1 + \frac{d(\ln f_\pm)}{d(\ln c^\ell)} \right) (1 - t_+) t_+ \mathbf{K}^\ell \frac{1}{c^\ell} \right) \nabla c^\ell \right. \\ &\left. + \frac{t_+}{F} \mathbf{K}^\ell \nabla \phi^\ell \right], \end{aligned} \tag{2.5}$$

$$0 = \nabla \cdot \left[\left(-\frac{2RT}{F} \left(1 + \frac{d(\ln f_\pm)}{d(\ln c^\ell)} \right) (1 - t_+) \mathbf{K}^\ell \frac{1}{c^\ell} \right) \nabla c^\ell + \mathbf{K}^\ell \nabla \phi^\ell \right], \tag{2.6}$$

where c^ℓ is the lithium-ion concentration in the electrolyte and ϕ^ℓ is the electrolyte potential, $\mathbf{D}^\ell$ and $\mathbf{K}^\ell$ are the diffusion and the electric conductivity coefficients respectively. R is the gas constant, T is the temperature, F is the Faraday constant. Finally, t_+ is the lithium-ion transference number, and $f_\pm$ is the mean molar activity. Since in this work the electrolyte has been considered ideal, this coefficient is not dependent on the concentration and therefore the term: $d(\ln f_\pm)/d(\ln c^\ell)$, goes to zero [52]. In the separator, the same equations as the liquid phase have been applied, but the transport coefficients were calculated through the Bruggeman's correlation:

$$\Psi_{eff} = \Psi \eta^b \tag{2.7}$$

where Ψ is a generic transport coefficient, electrical conductivity or diffusivity for LiBs, η is the porosity, and b is the Bruggeman exponent, equal to 1.5 for the case under consideration. Now we will define the boundary conditions typically applied. Particularly, we will distinguish between the side boundary conditions, faces parallel to the current direction, the current collector boundary conditions, the liquid-solid interface reaction, and the side applied to the faces parallel to the current direction. Starting from the side faces, we have a no-flux condition for the mass transport in both solid and liquid phases:

$$\mathbf{n}_s \cdot (\mathbf{D}^s \nabla c^s) = 0 \tag{2.8}$$

and

$$\mathbf{n}_\ell \cdot \left[\left(\mathbf{D}^\ell - \frac{2RT}{F^2} \left(1 + \frac{d(\ln f_\pm)}{d(\ln c^\ell)} \right) (1 - t_+) t_+ \mathbf{K}^\ell \frac{1}{c^\ell} \right) \nabla c^\ell + \frac{t_+}{F} \mathbf{K}^\ell \nabla \phi^\ell \right] = 0 \tag{2.9}$$

Similarly, for the charge transport we have insulation boundary conditions:

$$\mathbf{n}_s \cdot (\mathbf{K}^s \nabla \phi^s) = 0 \tag{2.10}$$

and

$$\mathbf{n}_\ell \cdot \left[\left(-\frac{2RT}{F} \left(1 + \frac{d(\ln f_\pm)}{d(\ln c^\ell)} \right) (1 - t_+) \mathbf{K}^\ell \frac{1}{c^\ell} \right) \nabla c^\ell + \mathbf{K}^\ell \nabla \phi^\ell \right] = 0, \tag{2.11}$$

For the current collector boundary conditions, we have no-flux and insulation conditions (Eqn. 2.9 and 2.11) for the liquid phase in both anode and cathode sides. For the solid phase, we applied the no-flux condition (Eqn. 2.8) for the mass transport in both anode and cathode sides, while we have a fixed value for the solid electric potential in the anode side:

$$\phi^s = 0, \tag{2.12}$$

and we have a constant density current applied at the solid-current collector interface at the cathode side:

$$-\mathbf{n}_s \cdot \left[\mathbf{K}^s \nabla \phi^s \right] = \pm \mathbf{n}_s \cdot J \tag{2.13}$$

where J [A/m^2] is the average entering current density, defined as:

$$J = F \frac{\int_{\mathbb{S}} \frac{\partial c^s}{\partial t} dV}{\int_{A_{cc}} dA_{cc}} \tag{2.14}$$

where the integral at the denominator is the active material-current collector area. The flux sign could be positive for discharge (lithium diffuses from the anode to the cathode) or negative for charge (lithium diffuses from from the cathode to the anode). The last boundary condition applied in the model is the mass and charge transfer at the liquid-solid interface. Notably, electrochemical charge–transfer reactions cause the continuum exchange between liquid and solid phases of Li ions, intercalated Li, and electrons following the reaction mechanism illustrated in Fig. 2.1. During a charge process, the intercalated lithium in the cathode active material reaches the liquid-solid interface and, thanks to the interfacial reaction, it diffuses in the liquid medium as a lithium ion. Then, it crosses the separator and, at the anode-electrolyte interface, the interfacial reaction transforms the lithium ion in intercalated lithium to balance the charge. The process is reversed during discharge. therefore, the mass and charge interfacial boundary conditions for the solid phase are:

$$-\mathbf{n}_s \cdot \left[\mathbf{D}^s \nabla c^s\right] = \frac{k}{F} f(c^\ell, c^s, \phi^\ell, \phi^s), \tag{2.15}$$

$$-\mathbf{n}_s \cdot \left[\mathbf{K}^s \nabla \phi^s\right] = k f(c^\ell, c^s, \phi^\ell, \phi^s), \tag{2.16}$$

Similarly, for the liquid phase:

$$\begin{aligned} &\mathbf{n}_\ell \cdot \left[\left(\mathbf{D}^\ell - \frac{2RT}{F^2}\left(1 + \frac{\partial \ln f_\pm}{\partial \ln c^\ell / c^s_{max}}\right) t_+ (1 - t_+) \mathbf{K}^\ell \frac{1}{c^\ell}\right) \nabla c^\ell + \frac{t_+}{F} \mathbf{K}^\ell \nabla \phi^\ell)\right] \\ &= \frac{k}{F} f(c^\ell, c^s, \phi^\ell, \phi^s) \end{aligned} \tag{2.17}$$

and

$$\begin{aligned} &\mathbf{n}_\ell \cdot \left[\left(-\frac{2RT}{F}\left(1 + \frac{\partial \ln f_\pm}{\partial \ln c^\ell / c^\ell_{ref}}\right)(1 - t_+) \mathbf{K}^\ell \frac{1}{c^\ell}\right) \nabla c^\ell + \mathbf{K}^\ell \nabla \phi^\ell)\right] \\ &= k f(c^\ell, c^s, \phi^\ell, \phi^s), \end{aligned} \tag{2.18}$$

The current density developed from the electrochemical reaction at the liquid-solid interface is called faradic current density and could be expressed through the well-known Butler-Volmer formalism [54, 53, 55]:

$$f(c^\ell, c^s, \phi^\ell, \phi^s) = 2\sqrt{c^\ell c^s (1 - c^s / c^s_{ref})} \cdot \sinh\left[(\phi^s - \phi^\ell - U) F / 2RT\right]. \tag{2.19}$$

The last term that appears in the Butler-Volmer equation is the overpotential U, an interfacial quantity defined at the liquid/solid boundary and that measures the deviation from local thermodynamic equilibrium of the charge-transfer reaction.

Specifically, at each point on the active surface we define:

$$U(\mathbf{x},t) = \phi^{s}(\mathbf{x},t) - \phi^{\ell}(\mathbf{x},t) - E^{s}_{\mathrm{eq}}(c^{s}(\mathbf{x},t)), \tag{2.20}$$

meaning that in the reversible reaction

$$\mathrm{Li}_{s} \rightleftharpoons \mathrm{Li}^{V}_{s} + \mathrm{Li}^{+}_{\ell} + e^{-}_{s} \tag{2.21}$$

less energy is recovered than what thermodynamics predict. The intercalated lithium in the electrode (Li_{S}) is formed from the reaction between a lithium ion from the liquid phase (Li^{+}_{L}) and an electron from the solid phase (e^{-}_{S}) and in the presence of a vacancy in the electrode (Li^{V}_{S}). Therefore, E^{s}_{eq} is the equilibrium electric potential difference. The overpotential is physically the local driving force for interfacial charge transfer under the constraints imposed by microscale transport. While $U(\mathbf{x},t)$ is not directly measurable, its macroscopic manifestations are reflected in observable polarization losses and terminal voltage. This depends on the SoC of the electrode and could be obtained essentially in two ways: performing a galvanostatic cycling analysis at a very low current, assuming that the cell behavior under this condition is similar to equilibrium, or it could be calculated with semi-empirical relations like the Redlich–Kister expansion [56, 52, 57] in which E^{s}_{eq} is a function also of the temperature.

2.2 Discrete Element Method

The most important information to define the starting state of the DEM simulations is the position (and possibly the pose), shape, and size of the involved elements or objects. For each of the systems explored in this work, the initial conditions were those of a cloud of non-overlapping spheres, subjected to a vertical force along the z-axis comparable to gravity. Given this external force, the DEM code computes the interaction forces between the spheres and integrates the motion equation for each sphere. The code starts reading the position of a certain sphere, $\mathbf{x}_{\mathrm{P}}(t)$, then it calculates the new position at time $t+\Delta t$, integrating Newton's second law for translation and rotation:

$$\mathrm{m}_{\mathrm{P}} \frac{d^{2}\mathbf{x}}{dt^{2}} = \sum_{\mathrm{i}=0}^{\mathrm{n}_{\mathrm{C}}} (\mathbf{F}^{\mathrm{N}}_{\mathrm{i,P}} + \mathbf{F}^{\mathrm{T}}_{\mathrm{i,P}}) + \mathrm{m}_{\mathrm{P}}\mathbf{g}, \tag{2.22}$$

$$\mathbf{I}_{\mathrm{P}}\frac{d\omega}{dt} = \sum_{\mathrm{i}=0}^{\mathrm{n_C}}(\mathbf{F}_{\mathrm{i,P}}^{\mathrm{T}} \times \mathrm{d_P(n)}), \tag{2.23}$$

where $\mathbf{F}_{\mathrm{i,P}}^{\mathrm{T}}$ and $\mathbf{F}_{\mathrm{i,P}}^{\mathrm{N}}$ are the shear and normal components of the contact force between the two spheres considered for the calculation, respectively. The vertical component is calculated as the product between the mass of the object ($\mathrm{m_P}$) and the gravitational acceleration constant ($\mathbf{g}$). In the second equation, $\mathbf{I}_{\mathrm{P}}$ is the moment of inertia and ω is the angular velocity. $\mathrm{d_P}$ is the distance between the contact point and the center of the particle, and n is the contact plane normal. Finally, $\mathrm{n_C}$ is the number of contact points. The interaction between two neighboring particles is modeled by a non-cohesive elastic-frictional contact model [58]. In this modeling approach, the contact force between two spheres can be calculated as the sum of two contributions: the normal component and the shear component. The particles are allowed to overlap at the contact point depending on the Young's modulus of the materials. The normal force is calculated from a difference in linear velocity along the interaction axis:

$$\mathbf{F}_{\mathrm{n}} = 2\frac{\mathrm{E_i r_i E_j r_j}}{\mathrm{E_i r_i + E_j r_j}}\mathbf{u}_{\mathrm{n}}, \tag{2.24}$$

where $\mathbf{u}_{\mathrm{n}}$ is the normal displacement and E is the Young's modules of i and j particles materials and $\mathrm{r_i}$ and $\mathrm{r_j}$ are the radii of particles i and j. In the present work, we considered a unique material for all the interacting particles, then $\mathrm{E_i} = \mathrm{E_j}$ for any i and j particles. The model does not considers long distance interactions, so when $\mathbf{u}_{\mathrm{N}} \geq 0$, the forces are null. The shear force comes from the perpendicular component of the linear velocity difference and the perpendicular component of the rotational velocity summation:

$$\mathbf{F}_{\mathrm{T}} = \mathrm{K_T}\mathbf{u}_{\mathrm{T}}, \tag{2.25}$$

where $\mathrm{K_T}$ is a function of $\mathrm{K_N}$ according to the Poisson's law. In this work, the materials' properties have not been modified from Yade default setting. The Blender simulation is similar to the previous one since it also solves Newton's equations of motion for a system of N particles, also allowing for the objects treated to be non-convex (a classic limitation of most DEM codes) thanks to the implementation of the Bullet Physics Library (BPL) [59] that can take into account the collision and interaction between arbitrarily-shaped particles in a rigid-body simulation [60].

2.3 Homogenization

Homogenization is a mathematical technique that allows the derivation of macroscopic equations and effective transport coefficients, starting from the microscopical governing equations [47–49]. This is possible only when two hypotheses are satisfied: the separation of scales and the periodicity of the domain of interest. The first hypothesis is satisfied if the characteristic length of the domain of interest L is bigger than the characteristic pore scale length l and this is true if the scale parameter ε is much lower than one: $\varepsilon = l/L << 1$. Indeed, as shown by Fig 2.2, when $\varepsilon \to 0$ we can consider the domain of interest homogeneous. The periodicity of the domain of interest is necessary because we can capture the influence of the macroscopic morphology on the effective transport coefficients by solving a closure problem over the defined unit cell. Thanks to the separation of scales we can redefine each variable or differential operator as:

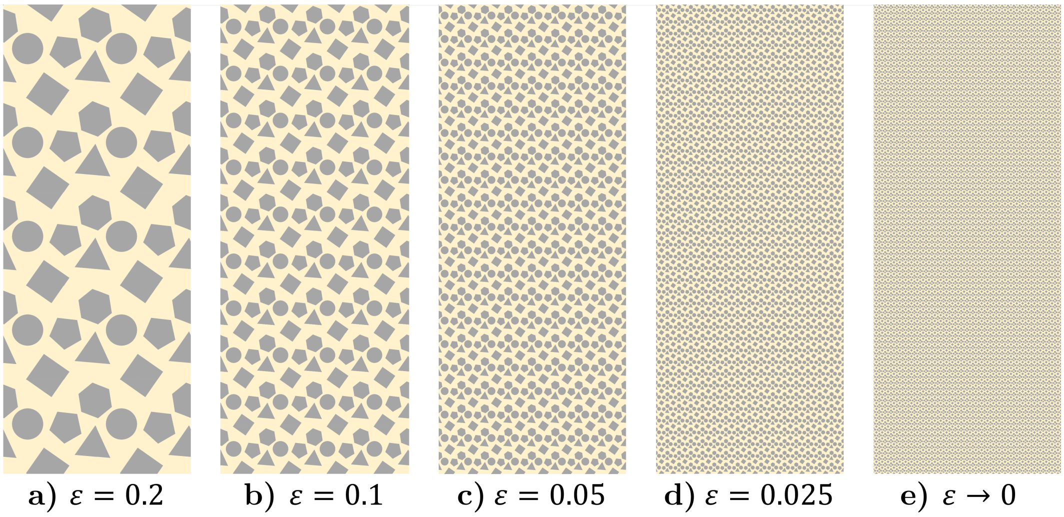
a) $\varepsilon = 0.2$ b) $\varepsilon = 0.1$ c) $\varepsilon = 0.05$ d) $\varepsilon = 0.025$ e) $\varepsilon \to 0$

Fig. 2.2 Homogenization of the porous medium as the limit of $\varepsilon \to 0$.

$$\begin{aligned} \psi_\varepsilon(\mathbf{x},t) &= \psi(\mathbf{x},\mathbf{y},t) \\ \frac{\partial \psi}{\partial t} &= \sum_i \frac{\partial \psi}{\partial \tau_i} \\ \nabla &= \nabla_\mathbf{x} + \varepsilon^{-1}\nabla_\mathbf{y} \end{aligned} \tag{2.26}$$

where ψ is a generic physical quantity of interest, $\mathbf{x}$ is the "slow" spatial variable which acts at the macroscale and captures the macroscopical behavior of the physical quantity, and $\mathbf{y}$ is the "fast" spatial variable which describes the microscopic unit cell and it takes into account all the fluctuations related to the morphology. These two variables are related thought the scale parameter as: $\mathbf{x} = \varepsilon^{-1}\mathbf{y}$. Since we have two separate scales, and we can have more than one characteristic times τ_i (e.g., reaction time, advection time, electric migration time, etc.) we have to also rewrite the derivative operators as shown in Eqn. 2.26. The idea of the homogenization is to rewrite the transport equations to obtain a macroscale equations which depends only on the "slow" variables $\mathbf{x}$. To do so, we apply the asymptotic expansion with respect to the scale parameter ε:

$$\psi(\mathbf{x},\mathbf{y},t) = \sum_{n=0}^{\infty} \varepsilon^n \psi_n(\mathbf{x},\mathbf{y},t) \tag{2.27}$$

and, at the end of all the derivations, we should obtain a reduced order model for the physics of interest. In the following sections, by means of example to the reader, homogenization via multiple scale expansion will be applied to the Stokes' equations to derive Darcy's law. Then, this same mathematical technique will be adopted to derive the upscaled version of charge and mass transport equations for LiBs of interest in this work. Before starting with the discussions, let us introduce some symbols and notations that will be used during the derivations. Let us consider consider a microscopic unit cell $Y = \mathcal{S} \cup \mathcal{L}$ illustrated in Fig. 2.3 constituted by a fluid phase $\mathcal{L}$ that surrounds the solid material $\mathcal{S}$, and let us define $\Gamma = \partial\mathcal{S} \cap \partial\mathcal{L}$ as the smooth surface between the two phases.

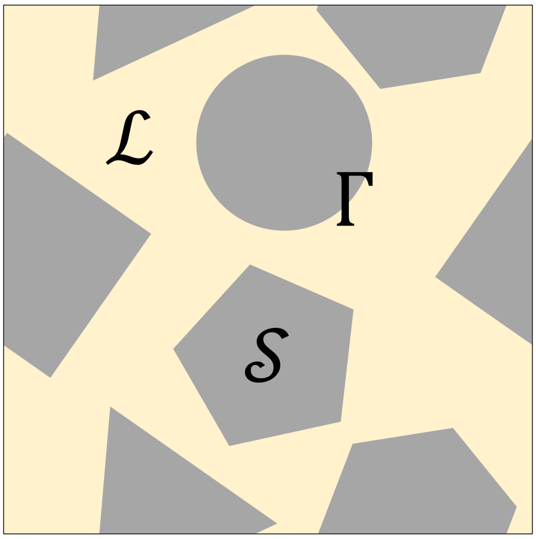

Fig. 2.3 Example of a generic unit cell Y, composed of a gray solid phase $\mathcal{S}$ submerged in the yellow liquid phase $\mathcal{L}$.

Let us define the following local averages of a general quantity $\mathcal{A}(\mathbf{x})$:

$$\begin{gathered}
\langle\mathcal{A}\rangle_\ell \equiv \frac{1}{|Y|}\int_{\mathcal{L}(\mathbf{x})} \mathcal{A} d\mathbf{y}, \quad \langle\mathcal{A}\rangle_s \equiv \frac{1}{|Y|}\int_{\mathcal{S}(\mathbf{x})} \mathcal{A} d\mathbf{y}, \\
\langle\mathcal{A}\rangle_\mathcal{L} \equiv \frac{1}{|\mathcal{L}|}\int_{\mathcal{L}(\mathbf{x})} \mathcal{A} d\mathbf{y}, \quad \langle\mathcal{A}\rangle_\mathcal{S} \equiv \frac{1}{|\mathcal{S}|}\int_{\mathcal{S}(\mathbf{x})} \mathcal{A} d\mathbf{y}, \\
\langle\mathcal{A}\rangle_\Gamma \equiv \frac{1}{|\Gamma|}\int_{\Gamma(\mathbf{x})} \mathcal{A} d\mathbf{y}.
\end{gathered} \tag{2.28}$$

The local averages are related through the porosity $\eta = |\mathcal{L}|/|Y|$, since $\langle\mathcal{A}\rangle_\ell = \eta\langle\mathcal{A}\rangle_\mathcal{L}$ and $\langle\mathcal{A}\rangle_s = (1-\eta)\langle\mathcal{A}\rangle_\mathcal{S}$. Furthermore, dimensional variables will be denoted with a hat (e.g., $\hat{\psi}$), while dimensionless quantities will be written without a hat (e.g., ψ).

2.3.1 From Stokes' to Darcy

The first applications of this mathematical technique comes from the end of 1980' [61–63] and one of the most famous implementation of the homogenization via multiple scale expansion is the derivation of the Darcy law starting from the Stokes' equation. Let us consider a macroscopic domain of length L formed by several periodic unit cells $Y = \mathcal{S} \cup \mathcal{L}$ with characteristic length l. The two phases are non reactive and the liquid one, an incompressible Newtonian fluid of viscosity $\hat{\mu}$ and density $\hat{\rho}$, flows through the pore space with a characteristic velocity U. We postulate that the Reynolds number is much lower than 1 ($Re = \hat{\rho}Ul/\hat{\mu} << 1$). Therefore, the flow is laminar and we can neglect the inertial and transient terms in the Navier-Stokes equations. Employing these assumptions, the fluid motion can be described by the Stokes' equations:

$$\begin{cases} -\hat{\nabla} \cdot \left(\hat{\mu}\hat{\nabla}\hat{\mathbf{u}}_\varepsilon\right) + \hat{\nabla}\hat{p}_\varepsilon = 0 & \hat{\mathbf{y}} \in \mathcal{L}, \\ \hat{\nabla} \cdot \hat{\mathbf{u}}_\varepsilon = 0 & \hat{\mathbf{y}} \in \mathcal{L}, \\ \hat{\mathbf{u}}_\varepsilon = 0 & \hat{\mathbf{y}} \in \Gamma, \end{cases} \tag{2.29}$$

where $\hat{\mathbf{u}}_\varepsilon$ is the fluid velocity and $\hat{p}_\varepsilon$ its pressure. Now we can define the dimensionless quantities that describe the system:

$$\mathbf{x} = \frac{\hat{\mathbf{x}}}{L}, \qquad \mathbf{u}_\varepsilon = \frac{\hat{\mathbf{u}}_\varepsilon}{U}, \qquad p = \frac{\hat{p}l^2}{\hat{\mu}UL} \tag{2.30}$$

Therefore, we can rewrite Eqn. 2.29 as:

$$\begin{cases} -\nabla \cdot \left(\varepsilon^2\nabla\mathbf{u}_\varepsilon\right) + \nabla p_\varepsilon = 0 & \mathbf{y} \in \mathcal{L}, \\ \nabla \cdot \mathbf{u}_\varepsilon = 0 & \mathbf{y} \in \mathcal{L}, \\ \mathbf{u}_\varepsilon = 0 & \mathbf{y} \in \Gamma, \end{cases} \tag{2.31}$$

Due to the separation of scales, we can replace each differential operator with the new one defined in Eqn. 2.26:

$$\begin{cases} -\left(\nabla_\mathbf{x} + \varepsilon^{-1}\nabla_\mathbf{y}\right) \cdot \left[\varepsilon^2\left(\nabla_\mathbf{x} + \varepsilon^{-1}\nabla_\mathbf{y}\right)\mathbf{u}_\varepsilon\right] & \\ \quad + \left(\nabla_\mathbf{x} + \varepsilon^{-1}\nabla_\mathbf{y}\right) p_\varepsilon = 0 & \mathbf{y} \in \mathcal{L}, \\ \left(\nabla_\mathbf{x} + \varepsilon^{-1}\nabla_\mathbf{y}\right) \cdot \mathbf{u}_\varepsilon = 0 & \mathbf{y} \in \mathcal{L}, \\ \mathbf{u}_\varepsilon = 0 & \mathbf{y} \in \Gamma, \end{cases} \tag{2.32}$$

Now, we can apply the asymptotic expansion from Eqn. 2.27 to both velocity and pressure:

$$\begin{cases} -\left(\nabla_{\mathbf{x}}+\varepsilon^{-1}\nabla_{\mathbf{y}}\right)\cdot\left[\varepsilon^{2}\left(\nabla_{\mathbf{x}}+\varepsilon^{-1}\nabla_{\mathbf{y}}\right)\left(\varepsilon^{0}\mathbf{u}_0+\varepsilon^{1}\mathbf{u}_1+\varepsilon^{2}\mathbf{u}_2\right)\right] & \\ \quad +\left(\nabla_{\mathbf{x}}+\varepsilon^{-1}\nabla_{\mathbf{y}}\right)\left(\varepsilon^{0}p_0+\varepsilon^{1}p_1+\varepsilon^{2}p_2\right)=\mathcal{O}(\varepsilon^{3}), & \mathbf{y}\in\mathcal{L}, \\ \left(\nabla_{\mathbf{x}}+\varepsilon^{-1}\nabla_{\mathbf{y}}\right)\cdot\left(\varepsilon^{0}\mathbf{u}_0+\varepsilon^{1}\mathbf{u}_1+\varepsilon^{2}\mathbf{u}_2\right)=\mathcal{O}(\varepsilon^{3}), & \mathbf{y}\in\mathcal{L}, \\ \left(\varepsilon^{0}\mathbf{u}_0+\varepsilon^{1}\mathbf{u}_1+\varepsilon^{2}\mathbf{u}_2\right)=\mathcal{O}(\varepsilon^{3}), & \mathbf{y}\in\Gamma. \end{cases} \tag{2.33}$$

Since we consider $\varepsilon\to 0$, we can collect all the ε^n order terms, for $n\in\mathbb{Z}$, and neglect all the ε^n order terms with $n>0$, Eqn. 2.33 becomes:

$$\begin{cases} \varepsilon^{-1}\left[\nabla_{\mathbf{y}}p_0\right]+\varepsilon^{0}\left[-\nabla_{\mathbf{y}}\cdot\nabla_{\mathbf{y}}\mathbf{u}_0+\nabla_{\mathbf{x}}p_0+\nabla_{\mathbf{y}}p_1\right]=\mathcal{O}(\varepsilon^{1}), & \mathbf{y}\in\mathcal{L}, \\ \varepsilon^{-1}\left[\nabla_{\mathbf{y}}\cdot\mathbf{u}_0\right]+\varepsilon^{0}\left[\nabla_{\mathbf{x}}\cdot\mathbf{u}_0+\nabla_{\mathbf{y}}\cdot\mathbf{u}_1\right]=\mathcal{O}(\varepsilon^{1}), & \mathbf{y}\in\mathcal{L}, \\ \varepsilon^{0}\mathbf{u}_0+\varepsilon^{1}\mathbf{u}_1=\mathcal{O}(\varepsilon^{2}), & \mathbf{y}\in\Gamma. \end{cases} \tag{2.34}$$

To ensure solvability with a bounded behavior as $\varepsilon\to 0$, the $\mathcal{O}(\varepsilon^{-n})$ terms must cancel point wise. Equating coefficients thus enforces a zero coefficient at order ε^{-n}, which fixes the leading-order constraint. Starting from the ε^{-1} order, we have that:

$$\begin{cases} \nabla_{\mathbf{y}}p_0=0, & \mathbf{y}\in\mathcal{L}, \\ \nabla_{\mathbf{y}}\cdot\mathbf{u}_0=0, & \mathbf{y}\in\mathcal{L}, \\ \mathbf{u}_0=0, & \mathbf{y}\in\Gamma. \end{cases} \tag{2.35}$$

Therefore p_0 does not depend on the fast spatial variable: $p_0(\mathbf{x},\mathbf{y})=p_0(\mathbf{x})$. Looking at the ε^0 order terms:

$$\begin{cases} -\nabla_{\mathbf{y}}\cdot\nabla_{\mathbf{y}}\mathbf{u}_0+\nabla_{\mathbf{x}}p_0+\nabla_{\mathbf{y}}p_1=0, & \mathbf{y}\in\mathcal{L}, \\ \nabla_{\mathbf{x}}\cdot\mathbf{u}_0+\nabla_{\mathbf{y}}\cdot\mathbf{u}_1=0, & \mathbf{y}\in\mathcal{L}, \\ \mathbf{u}_1=0, & \mathbf{y}\in\Gamma. \end{cases} \tag{2.36}$$

Let us search a solution in the form:

$$\begin{aligned} \mathbf{u}_0(\mathbf{x},\mathbf{y}) &= -\upsilon(\mathbf{y})\nabla_{\mathbf{x}}p_0(\mathbf{x}) \\ p_1(\mathbf{x},\mathbf{y}) &= \pi(\mathbf{y})\nabla_{\mathbf{x}}p_0(\mathbf{x})+\bar{p}(\mathbf{x}) \end{aligned} \tag{2.37}$$

Substituting Eqn. 2.37 into Eqn. 2.36 and 2.35 we obtain:

$$\begin{cases} \nabla_{\mathbf{y}} \cdot \nabla_{\mathbf{y}} \upsilon + \mathbf{I} + \nabla_{\mathbf{y}} \pi = 0, & \mathbf{y} \in \mathcal{L}, \\ \nabla_{\mathbf{y}} \cdot \upsilon = 0, & \mathbf{y} \in \mathcal{L}, \\ \upsilon = 0, & \mathbf{y} \in \Gamma. \end{cases} \tag{2.38}$$

The Eqn. 2.38 is called a closure problem and it takes into account the effect of the morphology over the velocity and pressure fields, field. The two variables introduced, υ and π, have no direct correspondence to dimensioned physical variables, and they are Y-periodic. We impose also the condition null average of the variable π over the fluid volume ($\langle \pi \rangle_{\mathcal{L}} = 0$) to have a unique solution. If we take the proposed solutions from Eqn. 2.37, particularly the one for the velocity field, and we integrate both members over the fluid volume, with respect to $\mathbf{y}$, we obtain:

$$\int_{\mathcal{L}} \mathbf{u}_0(\mathbf{x}, \mathbf{y}) d\mathbf{y} = - \int_{\mathcal{L}} \upsilon(\mathbf{y}) \nabla_{\mathbf{x}} p_0(\mathbf{x}) d\mathbf{y} \tag{2.39}$$

From the second integral, only $\upsilon(\mathbf{y})$ depends on $\mathbf{y}$ and therefore we can rewrite the previous equation, adopting the local averages definitions mentioned above (Eqn. 2.28) as:

$$\langle \mathbf{u}_0(\mathbf{x}, \mathbf{y}) \rangle_{\mathcal{L}} = -K(\mathbf{y}) \nabla_{\mathbf{x}} p_0(\mathbf{x}) \tag{2.40}$$

Eqn. 2.40 is the so called Darcy's equation and $K(\mathbf{y}) = \int_{\mathcal{L}} \upsilon(\mathbf{y}) d\mathbf{y}$ is the permeability tensor. Darcy's derivation is an easy and particular case of applicability of the homogenization technique, since the Stokes' equation is linear and stationary. Here are all the general steps of the homogenization procedure via multiple scale expansion that have been followed for the mathematical derivation of LiBs reduced order model:

1. Identification of the pore scale governing equations and the related boundary conditions
2. Dimensionless formulation of the pore scale governing equations
3. Linearize the equations (if they are not already) with a MacLaurin expansion
4. Substitute the derivative operators in the pore scale governing equations (Eqn.2.26) and apply the asymptotic expansion (Eqn. 2.27)
5. Rewrite the resulting equations in the form: $\sum_{i=1}^{N} \varepsilon^{N-i} f_i(\mathbf{x}, \mathbf{y}, \tau_I, \tau_{II}, ...) = 0$ and solve for $f_i(\mathbf{x}, \mathbf{y}, \tau_I, \tau_{II}, ...) = 0$

6. Derive and solve the closure problem and calculate the effective transport coefficients
7. Define the applicability regimes of the method for the system under consideration
8. Derive reduced order transport equations

2.3.2 Lithium-ions battery reduced order model

Here is the mathematical derivation of the homogenized 1D model for lithium-ion batteries. Even if the derivation is present in other scientific papers [45] we decided to rewrite it for two main reasons. First, the pore scale equation used in other papers may be different and the derivation may not be complete. Additionally, we introduced a homogenization over the boundary conditions at the current collector which might represent a novelty in the field. In this section, only the most relevant steps are reported, while the remaining parts are in the Appendix section:

1) Governing Equations

The governing equations for lithium ion batteries have already been reported in Sec. 2.1 above. The only difference is that the side boundary conditions are periodic instead of having insulation and no-flux conditions for charge and mass respectively.

2) Dimensionless formulation

A crucial step in asymptotic homogenization is to cast the governing equations in non-dimensional form. Non-dimensionalization makes the relative magnitude of the different terms explicit through dimensionless groups and through their dependence on the scale parameter ε. By specifying the regime of the relevant dimensionless numbers (e.g., whether they are the same order of magnitude as ε, smaller or larger), we clarify the range of validity of the homogenized model and the conditions under which it provides an accurate approximation of the pore-scale behavior. During the charge and discharge process, we can define four characteristic time scales, associated to the macroscopic length scale L: the heterogeneous reaction time $\hat{t}_R$, the ionic diffusion time $\hat{t}_{D_j}$, the ionic migration time $\hat{t}_{M_j}$, and the charge-discharge time $\hat{t}_C$ which are calculated as follow:

$$\hat{t}_R = \frac{LF}{k},\ \hat{t}_{D_j} = \frac{L^2}{D^j},\ \hat{t}_{M_j} = \frac{F^2 L^2 \hat{c}^s_{max}}{RTK^j},\ \hat{t}_C = \frac{LF\hat{c}^s_{max}}{J} \tag{2.41}$$

where $j = \ell, s$ and D^j and K^j are the characteristic values of the diffusion coefficient and electrical conductivity tensors in the solid ($j = s$) and liquid ($j = \ell$) phases. Now we can outline the dimensionless Damköhler, electric Péclet and dimensionless IR-drop numbers as:

$$Da_j := \frac{\hat{t}_{D_j}}{\hat{t}_R} = \frac{Lk}{FD^j};\ Pe_j := \frac{\hat{t}_{D_j}}{\hat{t}_{M_j}} = \frac{RTK^j}{F^2 D^j \hat{c}^j_{ref}};\ N_{ohm} := \frac{\hat{t}_{M_s}}{\hat{t}_C} = \frac{JLF}{RTK^s} \tag{2.42}$$

Moreover, we can define $\phi^j_\varepsilon = \hat{\phi}^j_\varepsilon F/2RT$ and $c^j_\varepsilon = \hat{c}^j_\varepsilon/\hat{c}^j_{ref}$ as the dimensionless electric potential and concentration, respectively, and c^j_{ref} is equal to the maximum intercalated lithium concentration ($c^s_{ref} = c^s_{max}$) or the maximum lithium-ions concentration in the electrolyte ($c^\ell_{ref} = c^\ell_{max}$). Furthermore, we can set $\mathbf{D}^j = \hat{\mathbf{D}}^j/D^j$ and $\mathbf{K}^j = \hat{\mathbf{K}}^j/K^j$ as the dimensionless diffusivity and electric conductivity coefficients, respectively. Finally, imposing $t = \hat{t}/\hat{t}_{D_\ell}$ as the dimensionless time and $\mathbf{x} = \hat{\mathbf{x}}/L$ as the dimensionless spatial variable, remembering that $\left(\dfrac{\partial \ln f_\pm}{\partial \ln \hat{c}^\ell_\varepsilon/\hat{c}^s_{max}}\right) = 0$, we can rewrite the mass and charge transport equations, with the corresponding boundary conditions, as follows. For the electrolyte (Eqn. 2.5 and Eqn. 2.6, subject to Eqn. 2.17 and Eqn. 2.18) we obtain:

$$\frac{\partial c^\ell_\varepsilon}{\partial t} = \nabla \cdot \left[\left(\mathbf{D}^\ell - 2t_+(1-t_+)Pe_\ell \mathbf{K}^\ell \frac{1}{c^\ell_\varepsilon}\right)\nabla c^\ell_\varepsilon + 2t_+ Pe_\ell \mathbf{K}^\ell \nabla \phi^\ell_\varepsilon\right], \tag{2.43}$$

and

$$0 = \nabla \cdot \left[\left(-2(1-t_+)Pe_\ell \mathbf{K}^\ell \frac{1}{c^\ell_\varepsilon}\right)\nabla c^\ell_\varepsilon + Pe_\ell \mathbf{K}^\ell \nabla \phi^\ell_\varepsilon\right], \tag{2.44}$$

subject to:

$$\begin{aligned} &\mathbf{n}_\ell \cdot \left[\left(\mathbf{D}^\ell - 2t_+(1-t_+)Pe_\ell \mathbf{K}^\ell \frac{1}{c^\ell_\varepsilon}\right)\nabla c^\ell_\varepsilon + 2t_+ Pe_\ell \mathbf{K}^\ell \nabla \phi^\ell_\varepsilon)\right] \\ &\quad = Da_\ell f(c^\ell_\varepsilon, c^s_\varepsilon, \phi^\ell_\varepsilon, \phi^s_\varepsilon) \end{aligned} \tag{2.45}$$

and

$$\begin{aligned}\mathbf{n}_\ell \cdot \left[\left(-2(1-t_+)Pe_\ell \mathbf{K}^\ell \frac{1}{c_\varepsilon^\ell}\right)\nabla c_\varepsilon^\ell + Pe_\ell \mathbf{K}^\ell \nabla \phi_\varepsilon^\ell)\right] \\ = Da_\ell f(c_\varepsilon^\ell, c_\varepsilon^s, \phi_\varepsilon^\ell, \phi_\varepsilon^s),\end{aligned} \tag{2.46}$$

where

$$f(c_\varepsilon^\ell, c_\varepsilon^s, \phi_\varepsilon^\ell, \phi_\varepsilon^s) = 2\sqrt{c_\varepsilon^\ell c_\varepsilon^s (1-c_\varepsilon^s)} \cdot \sinh\left[\phi_\varepsilon^s - \phi_\varepsilon^\ell - U\right]. \tag{2.47}$$

where $U = \hat{U}F/2RT$ is the dimensionless equilibrium potential. The no-flux and insulation conditions in the electrolyte (Eqn. 2.9 and Eqn. 2.11) assume the form of:

$$\mathbf{n}_\ell \cdot \left[\left(\mathbf{D}^\ell - 2t_+(1-t_+)Pe_\ell \mathbf{K}^\ell \frac{1}{c_\varepsilon^\ell}\right)\nabla c_\varepsilon^\ell + 2t_+ Pe_\ell \mathbf{K}^\ell \nabla \phi_\varepsilon^\ell)\right] = 0 \tag{2.48}$$

and

$$\mathbf{n}_\ell \cdot \left[\left(-2(1-t_+)Pe_\ell \mathbf{K}^\ell \frac{1}{c_\varepsilon^\ell}\right)\nabla c_\varepsilon^\ell + Pe_\ell \mathbf{K}^\ell \nabla \phi_\varepsilon^\ell)\right] = 0, \tag{2.49}$$

Similarly, the dimensionless formulation of the mass and charge transport equations in the electrode (Eqn. 2.3 and Eqn. 2.4, subject to Eqn. 2.15 and Eqn. 2.16) is given by:

$$\frac{\partial c_\varepsilon^s}{\partial t} = Da_\ell Da_s^{-1} \nabla \cdot \left[\mathbf{D}^s \nabla c_\varepsilon^s\right], \tag{2.50}$$

$$0 = \nabla \cdot \left[\mathbf{K}^s \nabla \phi_\varepsilon^s\right], \tag{2.51}$$

subject to

$$-\mathbf{n}_s \cdot \left[\mathbf{D}^s \nabla c_\varepsilon^s\right] = Da_s f(c_\varepsilon^\ell, c_\varepsilon^s, \phi_\varepsilon^\ell, \phi_\varepsilon^s), \tag{2.52}$$

$$-\mathbf{n}_s \cdot \left[2Pe_s \mathbf{K}^s \nabla \phi_\varepsilon^s\right] = Da_s f(c_\varepsilon^\ell, c_\varepsilon^s, \phi_\varepsilon^\ell, \phi_\varepsilon^s), \tag{2.53}$$

and the boundary conditions at the current collectors assume the form

$$-\mathbf{n}_s \cdot \left[\mathbf{D}^s \nabla c_\varepsilon^s\right] = 0 \tag{2.54}$$

$$\phi_\varepsilon^s = 0, \tag{2.55}$$

$$-\mathbf{n}_s \cdot \left[\mathbf{K}^s \nabla \phi_\varepsilon^s\right] = -\mathbf{n}_s \cdot N_{ohm} \tag{2.56}$$

Once the dimensionless formulations have been defined, we can proceed with the multiple-scale asymptotic expansion [40, 45, 46] to derive a continuous model that can approximate the pore-scale equations. Furthermore, we are going to individuate the applicability regimes and the error estimation.

3) Linearization of the equations

Before applying the asymptotic expansion, all the non-linear terms must be linearized, if any appear. For the physics under consideration, we have non-linear terms in the mass and charge transport equations in the liquid phase due to the electro-migration, and the Butler-Volmer term in all the liquid-solid boundary conditions. This linearization is mathematical, and it does not restrict the validity of the homogenization to near-equilibrium regimes. Indeed, the dependence of the electric current with respect to the electric potential remains exponential. As will be shown later, the model is still valid at high current value. The linearization has been done with a MacLaurin series, for $\varepsilon \to 1$ and is reported in Appendix A (Eqn. A5).

4) Asymptotic expansion

The method of asymptotic expansion consists of the introduction of a fast space variable $\mathbf{y} \in Y$ and four time variables: one related to the reaction (τ_r), two related to the electric migration in the electrolyte ($\tau_{m\ell}$) and in the active material particles (τ_{ms}) and, the last one associated to the discharge time (τ_c). Remembering that $t = \hat{t}_{D_\ell}^{-1}\hat{t}$ we obtain several definitions. According to Eqn. 2.26, specifically for LiB models, following the characteristic times definition from Eqn. 2.41, they assume the form:

$$\begin{aligned} &\mathbf{y} := \varepsilon^{-1}\mathbf{x} \quad \tau_r := \hat{t}_R^{-1}\hat{t} = Da_\ell t \quad \tau_{m\ell} := \hat{t}_{M_\ell}^{-1}\hat{t} = Pe_\ell t \\ &\tau_{ms} := \hat{t}_{M_s}^{-1}\hat{t} = Pe_\ell Da_\ell Da_s^{-1} t \quad \tau_c := \hat{t}_C^{-1}\hat{t} = Pe_\ell Da_\ell Da_s^{-1} N_{ohm} t \end{aligned} \tag{2.57}$$

Then, we can replace each pore-scale quantity $\psi_\varepsilon(\mathbf{x},t)$ with $\psi_\varepsilon(\mathbf{x},\mathbf{y},t,\tau_r,\tau_{m\ell},\tau_{ms},\tau_c)$ and obtain the following relations for the space and time derivatives:

$$\begin{aligned} &\nabla\psi_\varepsilon = \nabla_{\mathbf{x}}\psi + \varepsilon^{-1}\nabla_{\mathbf{y}}\psi \\ &\frac{\partial\psi_\varepsilon}{\partial t} = \frac{\partial\psi}{\partial t} + Da_\ell\frac{\partial\psi}{\partial\tau_r} + Pe_\ell\left(\frac{\partial\psi}{\partial\tau_{me}} + \frac{Da_\ell}{Da_s}\left(\frac{\partial\psi}{\partial\tau_{ms}} + N_{ohm}\frac{\partial\psi}{\partial\tau_c}\right)\right) \end{aligned} \tag{2.58}$$

Additionally, we represent $\psi = \{c^\ell;\phi^\ell;c^s;\phi^s\}$ as an asymptotic series in integer powers of ε, as explained in Eqn. 2.27 where ψ_n are Y-periodic functions in $\mathbf{y}$. Finally, we set

$$Pe_\ell = \varepsilon^{-\alpha},\ Da_\ell = \varepsilon^{\beta},\ Da_s = \varepsilon^{\gamma},\ Pe_s = \varepsilon^{-\delta},\ N_{ohm} = \varepsilon^{\zeta} \tag{2.59}$$

where the exponents α, β, γ, δ, ζ are arbitrary and determine the system behavior in the electrolyte and electrode phases. With the definitions in Eqn. 2.59, we are going to find the applicability regimes of the method. These conditions strictly depend on the separation of scales, and for this reason they were defined as a dependence on the scale variable ε.

5) Rewrite the equations

For solving and simplifying the model it is a good practice rewriting the expanded equations in the following form: $\sum_{i=1}^{N} \varepsilon^{N-i} f_i(\mathbf{x},\mathbf{y},\tau_I,\tau_{II},...) = 0$ and solve for each $f_i(\mathbf{x},\mathbf{y},\tau_I,\tau_{II},...) = 0$. This is a pure mathematical step and is reported in the Appendix A section.

6) Closure problem

Thanks to homogenization, is it possible to obtain a PDE to calculate analytically the effective transport coefficients. In this section, only the closure problem and the transport coefficient formula are reported, while the whole derivation is reported in the Appendix A section. The effective diffusivity and electrical conductivity coefficients are given by:

$$\mathbf{D}^{i\star\star} = \langle \mathbf{D}^i(\mathbf{I} + \nabla_{\mathbf{y}}\chi^i) \rangle \tag{2.60a}$$

$$\mathbf{K}^{i\star\star} = \langle \mathbf{K}^i(\mathbf{I} + \nabla_{\mathbf{y}}\chi^i) \rangle \tag{2.60b}$$

The closure variable $\chi^i(\mathbf{y})$ has zero mean, $\langle \chi^i \rangle_i = 0$ and is defined as the solution of the local problem

$$\nabla_{\mathbf{y}} \cdot \left(I + \nabla_{\mathbf{y}}\chi^i \right) = 0 \tag{2.61a}$$

$$\mathbf{n}_i \cdot \left(I + \nabla_{\mathbf{y}} \chi^i \right) = 0 \tag{2.61b}$$

where $i = \{\ell, s\}$. The variable χ has no physical meaning but it capture the morphological variation in the unite cell.

7) Applicability regimes

Homogenization guarantees that the reduced order model well reproduce the pore scale results with an error of order ε. This statement is always true if the operating regime, defined with the dimensionless numbers, falls into the applicability regimes. They consist in a range of values that the dimensionless numbers can assume to ensure the physical separation of scale. Thanks to the assumption made in Eqn. 2.59, we can determine the order of magnitude, relative to the scale parameter ε, that the dimensionless numbers should have to ensure the model's accuracy. Applicability regimes come out during the mathematical derivation in Appendix A, and here we report only the obtained conditions:

1. $\varepsilon << 1$
2. $Da_\ell < 1$
3. $Pe_\ell < 1$
4. $Da_\ell / Pe_\ell < 1$
5. $Da_s < 1$
6. $Da_s / Pe_s < 1$
7. $N_{ohm} < 1$
8. $\langle \chi^\ell \rangle_\Gamma \approx \langle \chi^\ell \rangle_\mathcal{L}$
9. $\langle \chi^s \rangle_\Gamma \approx \langle \chi^s \rangle_\mathcal{S}$

Constraints 1.-6. ensure separation of scales. While constraint 1. is almost always met in practical applications, since the pore size is generally much smaller than the electrode dimension, constraints 2.-6. depends on the relative importance of the diffusion, electrical migration, and reaction mechanisms, i.e., they impose constraints on the transport regimes that can be appropriately modeled by the continuum scale.

Constraints 8. and 9. are not necessary for scale separation, but facilitate the derivation of the effective parameters. As shown in Appendix A, these constraints allows one to interchange the surface and volume averages within errors on the order of ε^2. A separate discussion is required for the dimensionless IR-drop. This is defined as the ratio between the ohmic voltage loss across the electrode and the thermal voltage ($N_{ohm} = \frac{JL/K}{RT/F} = \frac{\Delta\phi_{ohm}}{RT/F}$). Intuitively, it counts how many thermal-voltage units are dissipated ohmically over the macroscopic length. Small values indicate weak ohmic driving, while large values indicate strong macroscopic fields. Homogenized coefficients and the classical applicability regimes derive from the microscopic boundary conditions at the internal liquid–solid interface and from scale separation. They are independent of how the macroscopic problem is forced. However, macroscopic boundary conditions control the magnitude of the macroscopic gradients. Large imposed currents increase N_{ohm}, which in turn can induce macroscopic boundary layers and spatially varying overpotentials that challenge the assumption of near-uniform sources within a unit cell. Thus, while the regimes are founded on microscopic physics, macroscopic forcing determines whether the solution actually resides in those regimes. Classical homogenization theory presumes that macroscopic gradients are moderate, ensuring that microscopic fields respond approximately linearly to unit macroscopic perturbations and that volumetric source terms remain nearly uniform within each representative cell. When N_{ohm} is large, the macroscopic potential drop is substantial, the overpotential becomes markedly nonuniform, and Butler–Volmer kinetics amplify local reaction heterogeneity; in this regime, the homogenization error can increase. On the other hand, for small N_{ohm}, the macroscopic driving is smooth, the interfacial source remains well distributed at the pore scale, and the upscaled equations give accurate results. Hence, N_{ohm} becomes a direct bridge between geometry and operating conditions: increased tortuosity, anisotropy, binder content, or loss of percolation lower the effective conductivity, thereby increasing N_{ohm}. This makes the metric useful for design: shortening the electrode, improving solid and electrolyte networks, or distributing current injection reduces N_{ohm} and enlarges the parameter space where homogenization is reliable. All the formalized constraints for both both liquid and solid phases are sufficient but not necessary conditions. Indeed, homogenization ensures an error of order ε if the model is within the applicability regimes determined through the constraints over dimensionless numbers, but this does not mean that working outside of these boundaries would lead to an error greater than ε. Suppose the dimensionless numbers are greater than

ε. In that case, we can not predict the error *a priori*, and we are forced to explore the dimensionless numbers space through simulation and calculate the error of the variable of interest. The constraints were imposed considering each term in the dimensionless formulation of order $\mathcal{O}(1)$. This assumption is conservative since the concentrations in the two active materials have been divided by their respective maximum value, and the electric potential is normalized with respect to a value that is greater than the maximum absolute value assumed by the electric potential during the simulation. In the model validation, we will show examples in which the applicability regimes conditions are not met, but the error is still on the order of magnitude of ε.

8) Reduce order transport equations

Mass and charge transport and boundary conditions equations in the electrolyte (Eqn. 2.43- 2.44- 2.45- 2.46- 2.48- 2.49) can be homogenized up to an order of ε^2 by the following effective mass and charge transport equations:

$$\begin{aligned}\eta \partial_t \langle c^\ell \rangle_{\mathcal{L}} = \nabla_{\mathbf{x}} \cdot \Big[\big(\mathbf{D}^{\ell\star\star} - 2t_+(1-t_+) Pe_\ell \mathbf{K}^{\ell\star\star} (1/\langle c^\ell \rangle_{\mathcal{L}}) \big) \nabla_{\mathbf{x}} \langle c^\ell \rangle_{\mathcal{L}} \\ + 2t_+ Pe_\ell \mathbf{K}^{\ell\star\star} \nabla_{\mathbf{x}} \langle \phi^\ell \rangle_{\mathcal{L}} \Big] + 2\eta \varepsilon^{-1} \mathcal{K}^\star Da_\ell f(\langle c^\ell \rangle_{\mathcal{L}}, \langle c^s \rangle_{\mathcal{S}}, \langle \phi^\ell \rangle_{\mathcal{L}}, \langle \phi^s \rangle_{\mathcal{S}})\end{aligned} \tag{2.62}$$

$$\begin{aligned}\nabla_{\mathbf{x}} \cdot \Big[\big(-2(1-t_+) Pe_\ell \mathbf{K}^{\ell\star\star} (1/\langle c^\ell \rangle_{\mathcal{L}}) \big) \nabla_{\mathbf{x}} \langle c^\ell \rangle_{\mathcal{L}} + 2 Pe_\ell \mathbf{K}^{\ell\star\star} \nabla_{\mathbf{x}} \langle \phi^\ell \rangle_{\mathcal{L}} \Big] \\ = -2\eta \varepsilon^{-1} \mathcal{K}^\star Da_\ell f(\langle c^\ell \rangle_{\mathcal{L}}, \langle c^s \rangle_s, \langle \phi^\ell \rangle_{\mathcal{L}}, \langle \phi^s \rangle_s)\end{aligned} \tag{2.63}$$

where:

$$\begin{aligned}& f(\langle c^\ell \rangle_{\mathcal{L}}, \langle c^s \rangle_s, \langle \phi^\ell \rangle_{\mathcal{L}}, \langle \phi^s \rangle_s) = \\ & \langle A_0 \rangle_{\mathcal{L}} \langle B_0 \rangle_{\mathcal{L}} + \varepsilon (\langle A_0 \rangle_{\mathcal{L}} \langle B_1 \rangle_\Gamma + \langle A_1 \rangle_\Gamma \langle B_0 \rangle_{\mathcal{L}}) = \\ & 2\sqrt{\langle c^\ell \rangle_{\mathcal{L}} \langle c^s \rangle_s (1 - \langle c^s \rangle_s)} \sinh\left((\langle \phi^s \rangle_s - \langle \phi^\ell \rangle_{\mathcal{L}} - U) \right)\end{aligned} \tag{2.64}$$

and the dimensionless effective reaction rate constant in the electrolyte phase ($\mathcal{K}^\star$) is determined by the pore geometry:

$$\mathcal{K}^\star = \frac{|\Gamma|}{|\mathcal{L}|}, \tag{2.65}$$

and the mass and charge boundary conditions at the liquid-current collector interface become:

$$\mathbf{n}_\ell \cdot \Big[\big(\mathbf{D}^{\ell\star\star} - 2t_+(1-t_+)Pe_\ell \mathbf{K}^{\ell\star\star}(1/\langle c^\ell\rangle_{\mathcal{L}})\big)\nabla_{\mathbf{x}}\langle c^\ell\rangle_{\mathcal{L}} + 2t_+ Pe_\ell \mathbf{K}^{\ell\star\star}\nabla_{\mathbf{x}}\langle\phi^\ell\rangle_{\mathcal{L}}\Big] = 0 \tag{2.66}$$

$$\mathbf{n}_\ell \cdot \Big[\big(-2(1-t_+)Pe_\ell \mathbf{K}^{\ell\star\star}(1/\langle c^\ell\rangle_{\mathcal{L}})\big)\nabla_{\mathbf{x}}\langle c^\ell\rangle_{\mathcal{L}} + 2 Pe_\ell \mathbf{K}^{\ell\star\star}\nabla_{\mathbf{x}}\langle\phi^\ell\rangle_{\mathcal{L}}\Big] = 0 \tag{2.67}$$

Similarly, mass and charge transport and boundary conditions equations in the electrode (Eqn. 2.50 - 2.51 - 2.52 - 2.53 - 2.54 - 2.55 - 2.56) can be homogenized up to an order of ε^2 by the following effective mass and charge transport equations:

$$\begin{aligned} \partial_t\langle c^s\rangle_s &= Da_\ell Da_s^{-1}\nabla_{\mathbf{x}} \cdot \Big[\mathbf{D}^{s\star\star}\nabla_{\mathbf{x}}\langle c^s\rangle_s\Big] \\ &- 2\varepsilon^{-1}\eta Da_\ell \mathcal{K}^\star f(\langle c^\ell\rangle_{\mathcal{L}}, \langle c^s\rangle_s, \langle\phi^\ell\rangle_{\mathcal{L}}, \langle\phi^s\rangle_s) \end{aligned} \tag{2.68}$$

and

$$\nabla_{\mathbf{x}} \cdot \Big[2Pe_s \mathbf{K}^{s\star\star}\nabla_{\mathbf{x}}\langle\phi^s\rangle_s\Big] = 2\varepsilon^{-1}\eta Da_s \mathcal{K}^\star f(\langle c^\ell\rangle_{\mathcal{L}}, \langle c^s\rangle_s, \langle\phi^\ell\rangle_{\mathcal{L}}, \langle\phi^s\rangle_s) \tag{2.69}$$

where $f(\langle c^\ell\rangle_{\mathcal{L}}, \langle c^s\rangle_s, \langle\phi^\ell\rangle_{\mathcal{L}}, \langle\phi^s\rangle_s)$ is expressed in Eqn. 2.64. The mass and charge boundary conditions at the solid-current collector interface become:

$$-\mathbf{n}_s \cdot \Big[\mathbf{D}^{s\star\star}\nabla_{\mathbf{x}}\langle c^s\rangle_s\Big] = 0 \tag{2.70}$$

and

$$-\mathbf{n}_s \cdot \Big[\mathbf{K}^{s\star\star}\nabla_{\mathbf{x}}\langle\phi^s\rangle_s\Big] = -\mathbf{n}_s \cdot N_{ohm} \tag{2.71}$$

$$\langle\phi^s\rangle_s = 0 \tag{2.72}$$

with Eqn. 2.71 and Eqn. 2.72 applied at the cathode and anode sides, respectively.

2.4 Finite Element Method

In this section the Finite Element Method (FEM) is described. Precursors of the matrix-based discretisation approach appeared in the 1930s by A. R. Collar and W. J.

Duncan[64–67]. Originally, the method was developed to solve structural problems, especially in the aeronautic and civil engineering. Forty years later, during the 1970s, the FEM application moved on others engineering fields, like electromagnetism. Knowing how this method works is crucial to understand how to implement unconventional equations, like the closure problem equations. Furthermore, the world of battery modeling is almost dominated by FEM simulations and in this section we will try to underline the most relevant features of this technique.

2.4.1 Weak formulation

To explain the method, we will take the Poisson's equation as example, one of the most simple and general PDE:

$$-\nabla \cdot (k(x)\nabla u(x)) = f(x) \quad x \in \Omega \tag{2.73}$$

subject to three kinds of boundary conditions. A Dirichlet condition over Γ_D, a Neumann condition over Γ_N, and a Robin condition over Γ_R [68, 69]:

$$\begin{aligned} &u(x) = g_D \quad x \in \Gamma_D \\ &\mathbf{n} \cdot (k(x)\nabla u(x)) = q_N \quad x \in \Gamma_N \\ &\mathbf{n} \cdot (k(x)\nabla u(x)) + \alpha\,(u(x) - u_\infty) = 0 \quad x \in \Gamma_R \end{aligned} \tag{2.74}$$

where $u(x)$ is the unknown variable, and $k(x)$ and $f(x)$ are the transport coefficient and the source term that could depend on the spatial variable x. A PDE of order n, like Eqn. 2.73, is called "strong formulation" and is characterized by a solution $s \in C^n$. Since most of the PDEs of engineering interest do not admit classical solutions we can search for solutions for the weak formulation instead of the strong one. To do so, we multiply the PDE by a test function $v(x)$ which is smooth ($v(x) \in C^\infty$) and regular. Then by integrating over the domain Ω, we can transfer one order of derivation from the unknown function $u(x)$ to the test function $v(x)$ through the integration by parts and we can add the boundary condition, by applying the Gauss theorem, to obtain the week formulation [70, 71, 68]:

$$\int_\Omega k\nabla u \cdot \nabla v \, d\Omega = \int_\Omega fvd\ \Omega + \int_\Gamma \mathbf{n} \cdot (k\nabla u)v \, d\Gamma \tag{2.75}$$

and, according to Eqn. 2.74, we obtain the complete weak formulation: find $u(x)$, with $u(x) = q_D$ for $x \in \Gamma_D$, such that, for any test function with $v = 0$ for $x \in \Gamma_D$ the following equation is verified:

$$\begin{gathered}\underbrace{\int_\Omega k \nabla u \cdot \nabla v d\Omega}_{\text{diffusion}} + \underbrace{\int_{\Gamma_R} \alpha u v d\Gamma}_{\substack{\text{Robin} \\ \text{boundary term}}} = \\ \underbrace{\int_\Omega f v d\Omega}_{\text{sources}} + \underbrace{\int_{\Gamma_N} q_N v d\Gamma}_{\substack{\text{Neumann} \\ \text{prescribed fluxes}}} + \underbrace{\int_{\Gamma_R} \alpha u_\infty v d\Gamma}_{\substack{\text{inhomogeneous} \\ \text{Robin term}}} .\end{gathered} \tag{2.76}$$

The cell problem obtained for the upscaled battery model represent an unconventional equation and must be implemented by hand in COMSOL. To do so, by using the "Weak Form PDE" interface, is it possible to write arbitrary PDE. Starting from Eqn. 2.61a and applying Eqn. 2.75:

$$\begin{cases} -\int_\Omega (I + \nabla_\mathbf{y} \chi^i) \nabla_\mathbf{y} v \, \mathrm{d}\mathbf{y} = 0 & \mathbf{y} \in \Omega, \\ \int_\Omega \chi^i v \, \mathrm{d}\mathbf{y} = 0, & \mathbf{y} \in \Omega, \\ \mathrm{n}_i \cdot (I + \nabla_\mathbf{y} \chi^i), & \mathbf{y} \in \Gamma. \end{cases} \tag{2.77}$$

2.4.2 Mesh and shape function

Once the weak formulation is defined, the domain must be divided in sub elements. An element is defined as the region of the domain enclosed between some point, also known as nodes [68]. In particular, we adopt segments for 1D domains, triangles for 2D domains, and tetrahedrons for 3D domains. If gradients direction is known is it possible to adopt a mesh that follows the gradients, with quadrilaterals (2D) and hexahedrons (3D). During the mesh construction is important avoiding flat or inverted elements that could lead to nonphysical results. FEM places degrees of freedom at mesh nodes on geometry-conforming elements, so the mesh can track curved and irregular boundaries without artificial stair-steps. As a result, complex CAD features are represented more accurately with fewer elements, and adaptive refinement can be focused near corners, interfaces, and thin layers [72]. This is especially helpful for problems with rapid surface-reaction kinetics, where having nodes on the surface makes the coupling and enforcement of boundary conditions straightforward. Indeed, FEM meshes are commonly very refined close to interfaces and boundaries, and coarser in the bulk, as shown by Fig. 2.4.

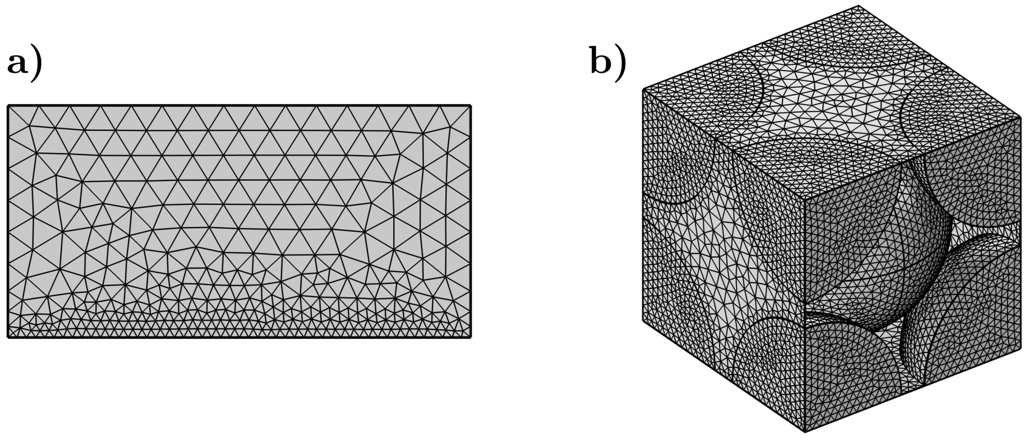

Fig. 2.4 a) example of a 2D mesh with a refinement close to the bottom edge; b) 3D mesh of a unit cell, with a finer refinement for the solid phase.

Since the domain is discretized into elements with nodes, we can approximate the solution with:

$$u(x) \approx u_h(x) = \sum_j U_j N_j(x), \tag{2.78}$$

where the coefficients U_j are the Degree of Freedom (DoF). For nodal (Lagrange) elements they coincide with the point wise values $U_j = u(x_j)$ at the nodes x_j. The functions N_j are the shape functions and, in the nodal case, satisfy the interpolation property

$$N_i(x_j) = \delta_{ij} \qquad \text{(Kronecker delta)}, \tag{2.79}$$

which ensures that evaluating u_h at a node returns the corresponding degree of freedom [73]. Different choices of shape functions define different approximation spaces. The most common choice for scalar fields is the Lagrange family. Let us consider a linear Lagrange approximation on $[x_1, x_2]$ with $h = x_2 - x_1$). The two nodal shape functions are:

$$N_1(x) = \frac{x_2 - x}{h}, \qquad N_2(x) = \frac{x - x_1}{h}, \tag{2.80}$$

and the interpolation function is

$$u_h(x) \;=\; U_1 N_1(x) \;+\; U_2 N_2(x), \tag{2.81}$$

which is piecewise linear and globally C^0 across the mesh. This choice is usually sufficient for weak forms that involve only first derivatives. When higher smoothness is required (e.g., where the weak form involves second derivatives), one may use cubic Hermite shape functions instead of the classical Lagrangian. On $[x_1, x_2]$, introduce the local coordinate $s = (x - x_1)/h \in [0, 1]$ and take as degrees of freedom the endpoint values, like the Lagrangian, and slopes,

$$U_1 := u(x_1), \quad U_1' := u'(x_1), \qquad U_2 := u(x_2), \quad U_2' := u'(x_2). \tag{2.82}$$

The cubic Hermite basis functions are

$$\begin{aligned} H_1(s) &= 1 - 3s^2 + 2s^3, & H_2(s) &= s - 2s^2 + s^3, \\ H_3(s) &= 3s^2 - 2s^3, & H_4(s) &= -s^2 + s^3, \end{aligned} \tag{2.83}$$

and the interpolation function is

$$u_h(x) \;=\; U_1 H_1(s) \;+\; hU_1' H_2(s) \;+\; U_2 H_3(s) \;+\; hU_2' H_4(s). \tag{2.84}$$

Since $\partial_x = (1/h)\,\partial_s$, these basis functions enforce

$$u_h(x_i) = U_i, \qquad u_h'(x_i) = U_i' \qquad (i = 1, 2), \tag{2.85}$$

leading to a globally C^1 function. Both mesh and discretizations influence the model accuracy. To increase it there are two main ways: increasing the interpolating polynomial degree (p-refinement) or decreasing the node distance (h-refinement), even if usually the best choice is an hybrid approach (hp-refinement).

2.4.3 Global system assembly

In a complex mesh, we should evaluate the integrals of the weak formulation in each element and to speed up this process the FEM adopt the quadrature method. To do so, the method defines a map, an iso parametric transformation which brings the local coordinates ξ of a reference element $\hat{K}$ (e.g. the reference 1D element is the

[-1,1] segment) to the physical coordinates x of the element K under consideration. The map has a Jacobian J and we can use it for the coordinate transformation:

$$d\Omega = |J| d\hat{\Omega}; \qquad \nabla N = J^{-T} \hat{\nabla} \hat{N} \tag{2.86}$$

Then the solver uses the connectivity (the relative position of one element with respect to the others, based on the nodes that two elements have in common) to build the final system:

$$\mathbf{KU} = \mathbf{F} \tag{2.87}$$

where, **K** is the sparse matrix of coefficients, **F** is the source vector and **U** is the matrix of the DoF [68].

In a complex mesh, the integrals of the weak formulation are evaluated element-wise. To do this efficiently and uniformly, the FEM adopts numerical quadrature on a reference element. The method defines a map (an isoparametric transformation) that carries the local coordinates $\hat{\xi}$ of a reference element $\hat{K}$ (e.g., $\hat{K} = [-1, 1]$ in 1D) to the physical coordinates $\mathbf{x}$ of the current element K_e:

$$\mathbf{x} \;=\; \mathbf{x}_e(\hat{\xi}) \;=\; \sum_{a=1}^{n_{\text{nodes}}} \mathbf{x}_a \hat{N}_a(\hat{\xi}), \qquad J(\hat{\xi}) \;=\; \frac{\partial \mathbf{x}_e}{\partial \hat{\xi}}. \tag{2.88}$$

The Jacobian J is used to transform measures and gradients:

$$d\Omega \;=\; \left|\det J(\hat{\xi})\right| d\hat{\Omega}, \qquad \nabla_{\mathbf{x}} N \;=\; J(\hat{\xi})^{-T} \hat{\nabla}_{\hat{\xi}} \hat{N}. \tag{2.89}$$

Similarly, boundary integrals use the surface Jacobian:

$$d\Gamma = |J_s(\hat{\xi})| \, d\hat{\Gamma} \tag{2.90}$$

The element contributions are then assembled using the mesh connectivity (the mapping from local element DOF indices to global DOF indices) to form the global linear system

$$\mathbf{KU} \;=\; \mathbf{F}, \tag{2.91}$$

where **K** is the sparse global coefficient (stiffness) matrix, **F** is the global load (source) vector, and **U** is the vector of DoF [74, 68].

2.5 Solver setup

In this section, the numerical methods adopted in the COMSOL simulation are described. Beyond the default formulation of the battery interface, we actively controlled the spatial discretisation through mesh refinement in regions with steep gradients (electrode–electrolyte interfaces and near current collectors), the time discretisation by using adaptive time stepping with user-defined output times, and the nonlinear solution strategy by adjusting damping and relative tolerances to ensure robust convergence over the full operating window. In addition, we verified mesh and time-step independence by systematically refining the mesh and tightening the temporal resolution until the cell voltage changed negligibly. The spatial discretisation used Lagrange finite elements on an unstructured mesh. We employed second-order (quadratic) elements for the primary field variables (concentrations and potentials), which provide improved accuracy for diffusion–electromigration problems at comparable degrees of freedom. For the electrochemical reaction terms imposed on internal boundaries, the same polynomial order was used consistently. The resulting nonlinear algebraic system was solved with a Newton-based method, using COMSOL's consistent Jacobian and automatic damping to enhance global convergence. The multiphysics coupling between charge conservation and species conservation was handled using a fully coupled approach, which was found to be more robust for strongly coupled regimes. We adopted an iterative Krylov method (GMRES) with algebraic multigrid preconditioning.

Chapter 3

Digital Model

This chapter summarizes the main steps for the geometrical model generation and the experimental technique adopted to extract the properties needed to generate the battery models. Specifically, we have a short explanation of the experimental analysis performed, followed by a detailed description of the pore scale model and the code used for its dynamic generation; lastly the reduced order model, with the closure problem. One simplification holding throughout all the presented model formulations is that the geometries considered are static during the charge-discharge process since we are not considering thermal-mechanical effects that can modify the electrode morphology, especially during high current cycling. It is important to clarify that the experimental part has been introduced not only to validate the pore scale model, but also for demonstrating that the developed script is capable on translating realistic geometrical and physical features into reproducible 4D computational models.

3.1 Experimental Analysis

The experimental electrodes employed in this work were used not only for the determination of the discharge curves, but also for the evaluation of the apparent diffusion coefficient within the active material particles, and for the estimation of the experimental porosity from FESEM images. The electrodes were manufactured by using a roll-to-roll coating process on commercial Cu metal foils (Schlenk®). The anode slurry was prepared by mixing 96.5 wt% of the active material (synthetic graphite, TIMREX SLS30, crystallinity Lc: 200 nm, specific surface area: 6.8

$m^2\ g^{-1}$, interlayer distance: 0.3357 nm, Imerys Graphite & Carbon), 0.5 wt% of conductive carbon black (TIMCAL C-NERGY™ Super C45, Imerys Graphite & Carbon), 1 wt% of sodium carboxymethyl cellulose (Na-CMC 2200, DAICEL), and 2 wt% of styrene-butadiene rubber (SBR, TRD 102A, JSR Micro N.V.). After solvent removal, electrode disks with an area of 1.766 cm^2 and a mass loading of 5.3 mg/cm^2 were punched out, vacuum dried at 120°C for 4 hours (Büchi Glass Oven B-585), and then transferred into an argon-filled glovebox (MBraun Labstar, H_2O and O_2 content <1 ppm) for cell assembly. Electrochemical performance evaluation was conducted in a half-cell configuration (Coin cells 2032) by using lithium discs (Ø 16 mm, 0.6 mm thick, MTI Corporation) as counter electrodes. All electrochemical tests were performed at room temperature by using an Arbin BT-2000 battery tester within the voltage range of 0.01–2 V vs. Li/Li^+. Charge/discharge rates were calculated based on the theoretical specific capacity of graphite (375 mAh g^{-1}). The apparent diffusion coefficient was experimentally evaluated with a specific analysis called Galvanostatic Intermittent Titration Technique (GITT) [75–78]. This test consists of intermittent discharge pulses at a low current value (with a $C_{rate} = C/20$), alternated by relaxation times, as illustrated in Fig 3.1. Two values of potential difference could be extracted from each current pulse: ΔE_t, which is the potential change for the discharge pulse, and ΔE_s, which is the steady state voltage change after eliminating the voltage drop originating from the electrical internal resistance. From these, and applying Eq. 3.1, we could obtain the diffusion coefficient in the electrode as a function of the SoC:

$$\mathbf{D}^s = \frac{4}{\pi t_p}\left(\frac{\mathrm{m}^s \mathrm{V}^s_M}{\mathrm{M}^s A^s}\right)^2 \left(\frac{\Delta E_s}{\Delta E_t}\right)^2, \tag{3.1}$$

where m^s, V^s_M, M^s, and A^s are respectively the mass, the molar volume, the molar mass, and the surface all referred to the active material. Instead, t_p is the pulse time, which for the case under exam was equal to 900 s and is equal to one third of the rest period. In this work, we considered a constant value calculated as the average over time of the diffusion coefficient to decrease the computational cost of the simulations but the code we developed is open to take into account also a dynamic diffusion coefficient, dependent on the state of charge.

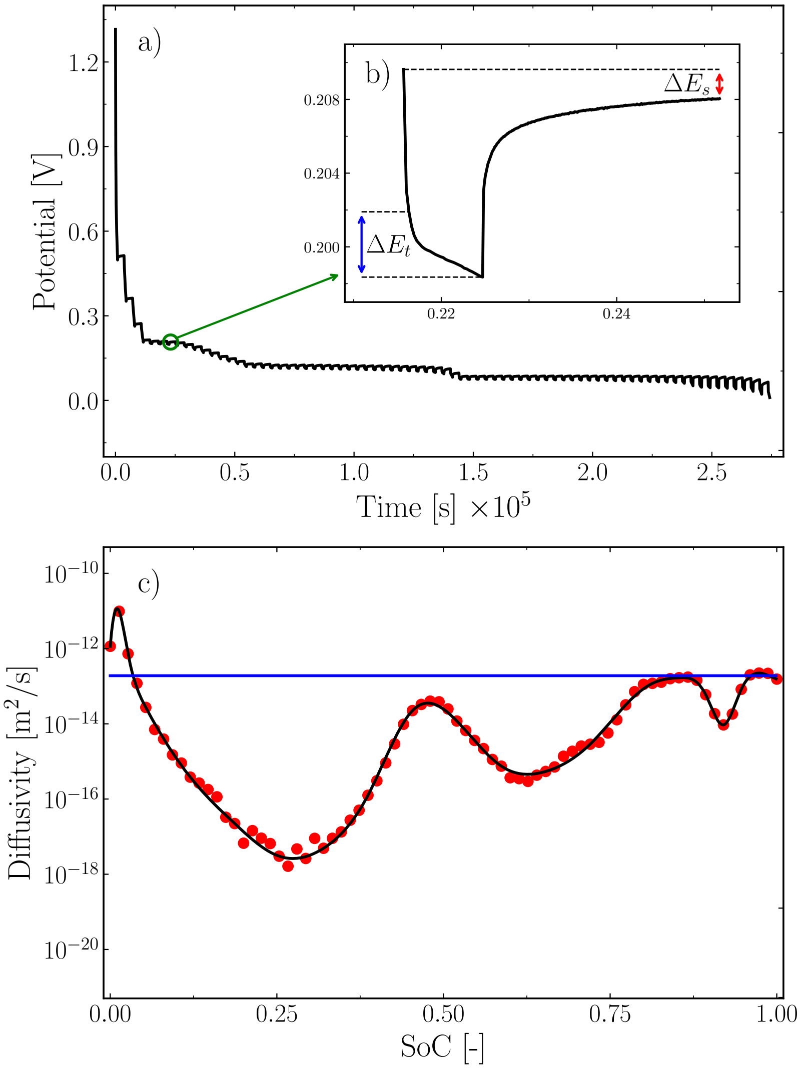

Fig. 3.1 Galvanostatic Intermittent Titration Technique. a) Discharge potential as a function of the time for the complete GITT. b) Discharge potential as a function of the time for one single pulse. ΔE_s (red) and ΔE_t (blue) are the two potential difference that appears in the equation that expresses the lithium diffusion coefficient as a function of the SoC. c) Lithium diffusion coefficient in the active material as a function of the SoC. The red dots are the values obtained from Eq. 3.1. The continuous black line is the interpolation line. The continuous blue line represents the average value.

Morphological analysis of the electrodes was performed using Field Emission Scanning Electron Microscopy (FESEM), Zeiss SUPRA 40 equipped with a Gemini column and Schottky field emission source (W at 1800 K). Electrode porosity was evaluated by extracting the pore network from FESEM cross-sectional micrographs [79, 80]. All the techniques mentioned and the tools adopted for the experimental part are considered part of the modern state of art regarding analysis on graphitic half cell batteries. Furthermore, the discharge curves for validating the modeling part fall in the acceptable ranges for this kind of electrodes[81–84].

3.2 Pore-scale model

Electrodes have been recreated by Discrete Element Method (DEM) simulations using the periodic compression routine implemented in the open-source code Yade [85] (version 2022.01a) coupled with the open-source software Blender [86] (version 4.3.2). The choice of these two pieces of software comes from several reasons: first of all, both of them have a Python API (version 3.10.4) that helped us to produce different geometries in a very simple and automatic way. Moreover, this coupling between a fast DEM code and Blender gives us the possibility to produce packings of particles with complex geometries faster than only using directly a code for the rigid body simulation of non-convex objects (such as Blender). Below we describe the workflow for the geometry reconstruction. Some notions and equations about DEM simulations have already been reported in Sec. 2.2. The first step for this work is to analyze the best shape to reproduce graphite particle with; where the chosen shape is to be the result of a trade-off between adherence to the real morphology and the computational cost in reproducing the actual particle packing.

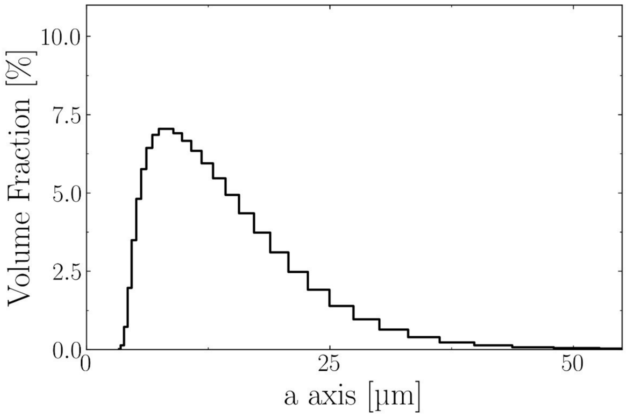

Fig. 3.2 Experimental PSD of commercial graphite powder.

Looking at the FESEM images, from Fig. 1.1 we noticed that the shape with the required characteristics can be an ellipsoidal one with suitably chosen lengths for its axes. Indeed, shapes with one or more non-curved characteristic lengths (e.g. parallelepipeds, cylinders, etc.) would cause non-realistic contact points. To produce a polydispersed particle packing, with ellipsoidal shapes, we need a Particle Size Distribution (PSD) and an Aspect Ratio (AR) that in this case is assumed to be constant. In our case, the PSD comes out from an experimental analysis performed in our laboratory [87], and it is reported in Fig. 3.2; instead, the AR was calculated as an average from FESEM images. We noticed that graphite particles are flake-shaped, with one size much smaller than the other two, and for this reason, we tried to model them through flattened ellipsoids. Each ellipsoid is characterized by the three semi-axes a, b, c, with $a > b >> c$ for the case under consideration. The major axis is taken from the experimental PSD, which allowed to produce a packing of particles with different sizes. Instead the $AR = a/b$ permits to transform each sphere in an ellipsoid. The maximum thickness of the flake, equal to $2c$, is instead kept fixed ($c = 1.5$ [µm]). This value was chosen close to the average thickness measured from the available FESEM images. This brings us to another reason for this modelling choice. Local variations in the thickness of the graphite flakes would influence the charge and mass transport: in this study we have chosen to represent this geometric variations by representing the flakes as ellipsoidal shapes, whose thickness varies along their other two main axes (a and b). Furthermore, the open-source code we developed and used to generate the geometries and setup the simulations is capable of considering a distribution of thicknesses or aspect ratio, should such data become available. Once the input data have been collected, it is possible to run a DEM simulation that can produce and realistic packing of particles.

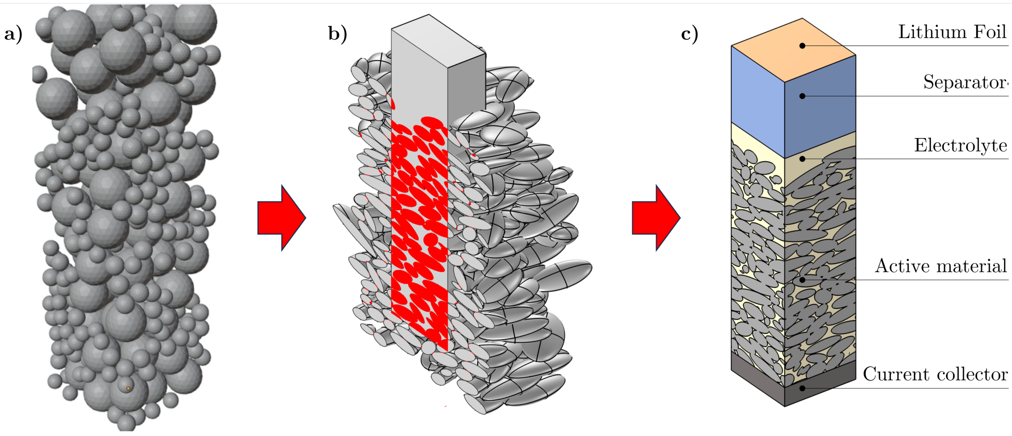

Fig. 3.3 Main steps of the geometry generation process: a) Packing of spheres. b) Layer of ellipsoids. c) Final electrode.

The PSD is the input for Yade, that produces in turn a packed cloud of spheres in a box, each of them characterized by a radius equal to the major axis of the eventual corresponding ellipsoidal particle. This setting is fundamental to avoid particle-particle interpenetration in the next step. Therefore, from Yade, we characterize each particle with three spatial coordinates (its center position) and one radius and these parameters will become, together with the AR, the input for Blender. In Blender, we can substitute in place each sphere with a differently shaped object, an ellipsoid in this case, so that it is inscribed in the sphere itself. With procedure, we are sure that each particle, independently of the final shape, will be free to roll and fall to recreate a packed arrangement (due to virtual gravitational/compaction force). The ellipsoids are initially placed aligning the shorter axes (c) orthogonally with the fall direction. With this choice, we want to emulate the calendering process and the ordering it forces on the final electrode particles or flakes. During this manufacturing operation, graphite particles are compressed to increase the volume density, and, due to the lamellar conformation, they tend to orient themselves parallel to the surface of the current collector [88]. Finally, we can run the Blender rigid-body simulation to increase the compaction of the particle bed and finalizing the particle sedimentation process. Now, from Blender, we characterize each particle with nine degrees of freedom: three for the center position, three for its dimensions, and three for the rotation around the axes, and these are the geometrical input parameters for COMSOL Multiphysics 6.1. The script takes as input the geometrical and the physical parameters, specified in Tab. 3.1. In the first group there is the spatial characterization of each particle and the dimensions of the half cell: thickness and width of both electrode and separator, and are varied for each different packing realization. The physical parameters instead concern everything that is a material property, like equilibrium potential, diffusion coefficient, electrical conductivity and so on. The Java code works in the following way. First of all, the particles are generated with the input procedure just explained, together with a central block whose dimensions depend on the REV analysis, as explained below. In order to facilitate the meshing algorithm in the construction of the grid in the area close to the contact point between two adjacent particles, each of them has been enlarged by the 1% in each dimension to avoid representing contact points as zero-dimensional entities and improve the meshing process by transforming them into surface contact with a but non-zero area, albeit very small to avoid distorting the geometry too much. Then the portion of particles that are outside the block or that are not in touch with the central core of particles are eliminated. Regarding the latter, the reason for their elimination from the geometrical model is that the particle fragments not in any contact with the electrode would lead to a numerical error in the simulation: the developed code automatically recognizes and deletes them. After this, the separator is placed in the

Parameter	**Value**	**Description**
c_0^s	0 [mol/m^3]	Initial Li concentration in solid
c_0^ℓ	1000 [mol/m^3]	Initial Li$^+$ concentration in liquid
$c_{\max}^s$	31507 [mol/m^3]	Maximum Li concentration in solid
$\mathrm{SoC}_{\max}$	0.95	Final particle lithiation level
$\mathrm{SoC}_{\min}$	0	Initial particle lithiation level
$\mathbf{K}^s$	100 [S/m]	Electrode electrical conductivity
$\mathbf{K}^\ell$	0.743 [S/m]	Electrolyte electrical conductivity
$\mathbf{D}^s$	1.317×10^{-14} [m^2/s]	Electrode diffusion coefficient
$\mathbf{D}^\ell$	3.613×10^{-10} [m^2/s]	Electrolyte diffusion coefficient
α_a	0.5	Anodic symmetry factor
α_c	0.5	Cathodic symmetry factor
t_+	0.363	Lithium-ions transference number
$h_{\min}$	0.85 [µm]	Minimum mesh size
$h_{\max}$	6.6 [µm]	Maximum mesh size
Δx	20 [µm]	Electrode thickness along X direction
Δy	20 [µm]	Electrode thickness along Y direction
Δz	60 [µm]	Electrode thickness along Z direction
sep	20 [µm]	Separator thickness

Table 3.1 Parameters used in the 4D resolved electrochemical model

upper part of the domain and all the domains and surfaces are named to associate each of them with the corresponding material and the physics that will be solved in that zone. The code automatically detects each zone or surface using boolean selection operations already implemented in COMSOL Multiphysics. In particular, it identifies three domains: (i) the liquid electrolyte, where the concentrated solution theory (Eqs. 2.5 and 2.6) is applied; (ii) the separator, where the same equations as in the liquid phase are used, but with effective parameters calculated through the Bruggeman correlation (Eqn. 2.7); and (iii) the solid active material, where Fick's law and Ohm's law (Eqs. 2.3 and 2.4, respectively) are solved. For the boundary conditions, the no-flux constraint (Eqs. 2.8 and 2.9) is imposed on all external faces, while the insulation constraint (Eqs. 2.10 and 2.11) is applied except at the separator top face, treated as an infinite lithium source, and at the solid–current collector faces, which allow electron transfer to ensure charge balance. At the liquid-solid interface, the exchange of mass and charge is allowed thanks to Eqn. 2.19. Finally, the domain is meshed and even this step is automatically operated by the script. The user can select an initial mesh Refinement Level (RL), ranging from 1 (Extremely Coarse) to 9 (Extremely Fine), following in COMSOL own classification of meshing strategies. Starting from this setting, the code attempts to generate the mesh for the domains. If one or more surfaces can not be meshed at the chosen RL, the code identifies them, discards the previous mesh, and restarts the procedure by first meshing the problematic faces. If distorted elements persist, the RL is automatically increased, and the meshing process restarts, proceeding stepwise from faces back to domains. If the code can not produce a mesh at all, an error message is printed. Fig. 3.4 summarizes the mesh generation process.

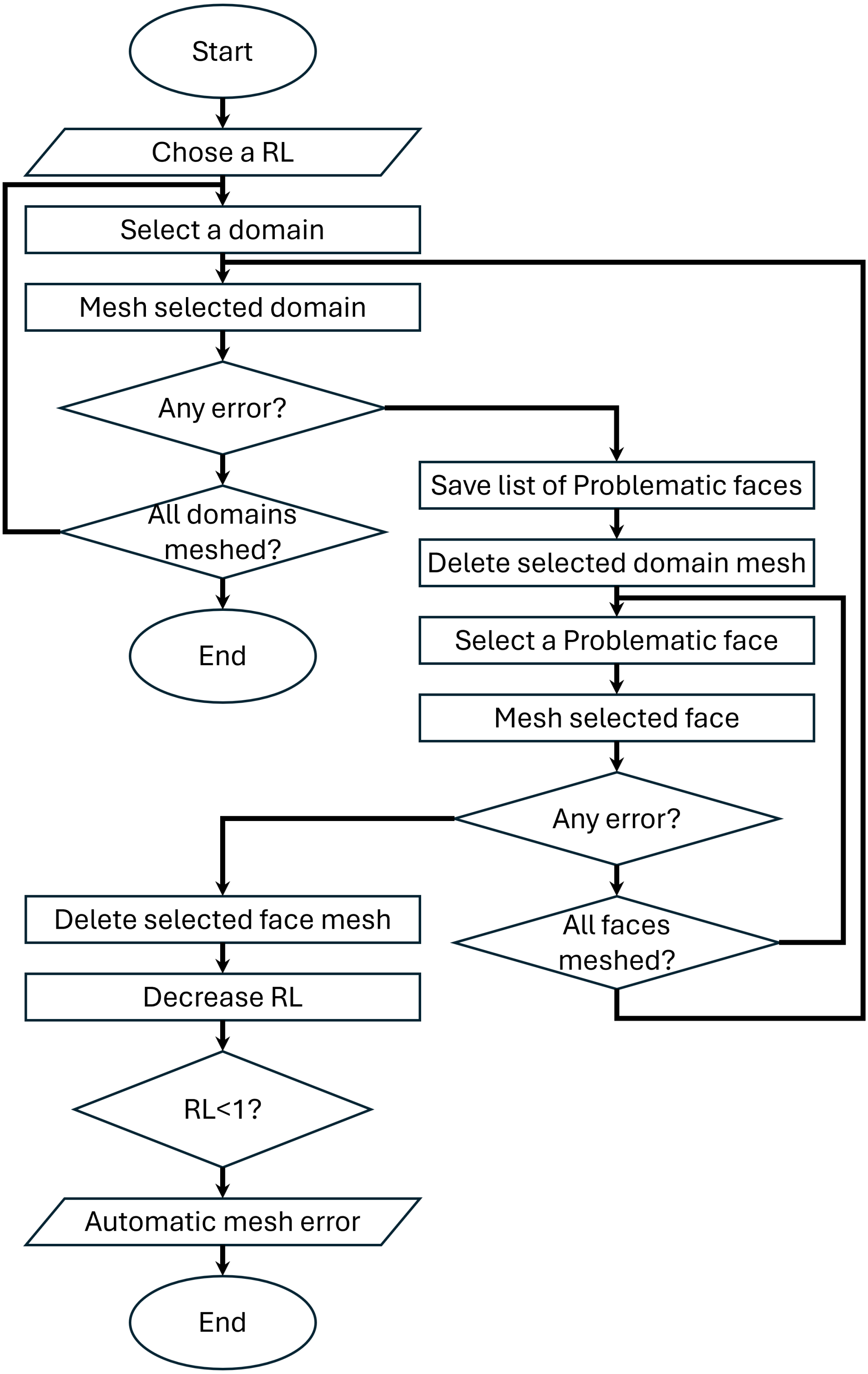

Fig. 3.4 Flowchart of the mesh generation.

For the present work, we chose a starting RL=4 with element size dimension between 0.85×10^{-6} [m] and 1.8×10^{-6} [m], resulting in a total number of elements ranging from 180,000 to 300,000 depending on the complexity of the system. This choice is the result of a good compromise between low computational cost and high accuracy of the simulation results. In this study we wanted to focus our attention on three systems with different morphology moving towards increasing complexities. The simplest electrode has spherical mono-disperse particles, the second one has spherical poly-disperse particles, and the most complex has flattened ellipsoids to reproduce in a better way the realistic shape of graphite particles, as discussed earlier. The system with polydisperse spheres was built considering particles with a volume equal to the one in the model with ellipsoidal particles. The most simple model, a package of monodisperse spheres, was instead built considering an average radius calculated from the system of polydisperse spheres. From each half cell, the discharge curve and the concentration of intercalated lithium in the active material have been analyzed and compared. It is important to specify that, since we have simulated a half cell, the graphite is treated as a cathode, and therefore during discharge, lithium diffuses from the electrolyte to the active material particle and so the concentration of lithium increases during the discharge. The half cells are produced with a thickness of 60 [µm] for the electrode plus 20 [µm] for the separator. To obtain a good characterization of the system, the electrodes have a width of 20 [µm] along the X and Y axes, and the discharges were performed at different current values. The electrode and separator thicknesses are taken from FESEM images, and the width value has been obtained from a REV (Representative Elementary Volume) analysis performed both physically (discharge curves) and geometrically (porosity and specific surface), as it is shown in Fig. 3.5. Among the two geometrical features, porosity is the easiest to compare with experimental evaluation. Nonetheless, the most meaningful insights come from the active material-electrolyte interface within the electrode, as this directly affects lithium-ion transport and intercalation kinetics. At the end of the analysis, we chose to perform our simulations on a domain with a width of 25 [µm].

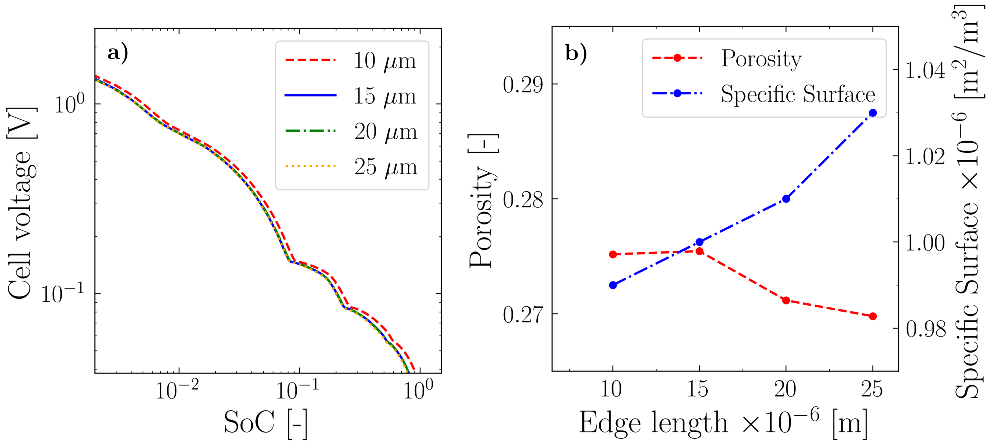

Fig. 3.5 a) physical REV analysis, discharge curve comparison; b) geometrical REV analysis, evaluation of porosity and specific surface.

Each simulation have been performed with a fully coupled solver, using GMRES iterative algorithm with a relative tolerance of 0.0001. An adaptive time step has been employed, with 1001 equally spaced output times, determined by the C_{rate} (Output times = range(0, $0.001/C_{rate}$, $1/C_{rate}$)). Simulations have been performed on 8 cores and required between 10 and 20 hours of simulation, with a consumption of memory of approx 40 Gb.

3.3 Homogenization

In the second part of the present work, we formalized and derived the upscaled equations of the charge and mass transport starting from the microscale ones. Then we validated the new model by comparing it with several pore-scale simulations under different operating conditions. As postulated by the homogenization theory, the geometry must be periodic [40, 46]. Therefore, we built a unit cell with a solid electrode submerged in the liquid electrolyte. For the purpose of this work, we chose a Body Centered Cubic (BCC) unit cell with an edge dimension of $l = 5$ [µm] [89, 17]. The representation of the unit cell is shown in Fig. 3.6. This unit cell is the same for both the anode and cathode side, and each electrode is composed of 20 unit cells in the separator-current collector direction. In this way, we have an electrode length of $L = 20 \cdot l = 100$ [µm] [90] and then the scale parameter is $\varepsilon = l/L = 0.05$. Therefore, in the comparison between the reduced order model and the pore-scale one, we are expecting an error of $err = |\psi_{up} - \psi_{ps}| = \mathcal{O}(\varepsilon)$, where $\psi = \{c^\ell, c^s, \phi^\ell, \phi^s\}$. The two electrodes are divided by the separator, which is considered as a pure liquid domain and not a porous zone. Therefore, the homogenized model will be a 1D model divided into three domains: two porous electrodes with a length of $L = 100$ [µm], divided by the liquid separator. We adopted these approximations because we are mainly interested in demonstrating the validity of homogenization theory applied in lithium-ion batteries. As such, to obtain this previously untested validation and in order to minimize spurious computational errors not related to the theoretical upscaling, we started from the simple (hence, most robust) system, and the BCC repeating unit was built by uniformly shaped spheres. The implementation of a more accurate model, e.g., considering different morphologies for the active material particles, will be one of our future works.

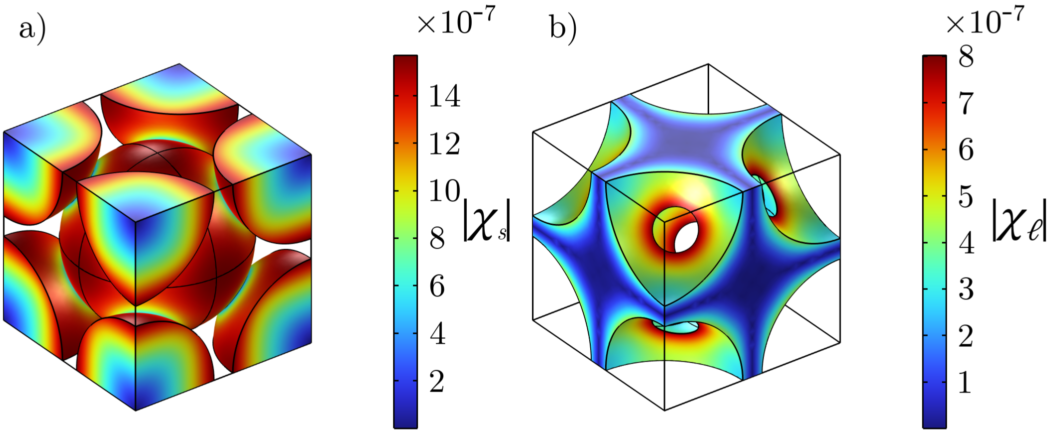

Fig. 3.6 Unit cell with the closure problem solution. a) Magnitude of the vector field χ_s in the solid phase. b) Magnitude of the vector field χ_ℓ in the liquid phase.

After the determination of the macroscopic equations, the first step is to find the solution of the closure problems (Eqn. 2.61a) to determine the effective diffusion coefficient and electrical conductivity in both liquid and solid phases. Since the geometry is symmetric along three orthogonal planes, we are expecting to have a symmetric distribution of the closure variables, as shown in Fig. 3.6. Furthermore, since the transport coefficients are considered constants and independent of the concentration, we have that the effective coefficients reduce to scalar tensors:

$$\langle \mathbf{I} + \nabla_{\mathbf{y}} \chi^{\ell} \rangle_{\ell} = \begin{bmatrix} 1.617 \cdot 10^{-1} & -3.051 \cdot 10^{-7} & -5.203 \cdot 10^{-8} \\ -3.051 \cdot 10^{-7} & 1.617 \cdot 10^{-1} & 1.003 \cdot 10^{-7} \\ -5.203 \cdot 10^{-8} & 1.003 \cdot 10^{-7} & 1.617 \cdot 10^{-1} \end{bmatrix} \approx 0.1617 \cdot \mathbf{I}$$

$$\langle \mathbf{I} + \nabla_{\mathbf{y}} \chi^{s} \rangle_{s} = \begin{bmatrix} 3.763 \cdot 10^{-1} & 1.439 \cdot 10^{-4} & -3.390 \cdot 10^{-5} \\ 1.439 \cdot 10^{-4} & 3.763 \cdot 10^{-1} & -1.445 \cdot 10^{-5} \\ -3.390 \cdot 10^{-5} & -1.445 \cdot 10^{-5} & 3.763 \cdot 10^{-1} \end{bmatrix} \approx 0.3763 \cdot \mathbf{I}$$

If a non-cubic or non-symmetric unit cell were considered, the homogenised response would generally become anisotropic. In that case, the correction tensor would remain diagonal (for a unit cell aligned with the coordinate axes), but its diagonal entries would no longer be equal, i.e., $T_{11} \neq T_{22} \neq T_{33}$. For our analysis, we explored different ranges of the variables influencing and defining the dimensionless numbers in Eqn. 2.42 and observed their impact on both the dimensionless numbers and the resulting upscaled model error.

Parameter	**Value**			**Description**
	Anode	Electrolyte	Cathode	
c_0^s [mol/m^3]	0	0	0	Initial Li concentration in solid
c_0^ℓ [mol/m^3]	1000	1000	1000	Initial Li$^+$ concentration in liquid
$c_{\max}^s$ [mol/m^3]	31507	31507	31507	Maximum Li concentration in solid
$\mathrm{SoC}_{\max}$	0.95	0.95	0.95	Final particle lithiation level
$\mathrm{SoC}_{\min}$	0	0	0	Initial particle lithiation level
$\mathbf{K}^s$ [S/m]	100	100	100	Electrode electrical conductivity
$\mathbf{K}^\ell$ [S/m]	0.743	0.743	0.743	Electrolyte electrical conductivity
$\mathbf{D}^s$ [m^2/s]	1.317E-14	1.317E-14	1.317E-14	Electrode diffusion coefficient
$\mathbf{D}^\ell$ [m^2/s]	3.613E-10	3.613E-10	3.613E-10	Electrolyte diffusion coefficient
α_a	0.5	0.5	0.5	Anodic symmetry factor
α_c	0.5	0.5	0.5	Cathodic symmetry factor
t_+	0.363	0.363	0.363	Lithium-ions transference number
L [µm]	100	100	100	Electrode length
sep [µm]	25	25	25	Separator thickness

Table 3.2 Operating conditions explored for testing the upscaled model.

$Da_{s,neg}$	$Da_{\ell,neg}$	$Pe_{s,neg}$	$Pe_{\ell,neg}$	$N_{ohm,s,neg}$
2.69E+00	8.78E-04	6.46E+03	2.00E-02	3.09E-04
$Da_{s,pos}$	$Da_{\ell,pos}$	$Pe_{s,pos}$	$Pe_{\ell,pos}$	$N_{ohm,s,pos}$
5.09E+00	1.26E-03	5.47E+03	1.29E-02	3.09E-04

Table 3.3 Dimensionless numbers values explored for testing the upscaled model.

We started from the coefficient values detailed in Tab. 3.2, obtained from common literature values [17, 45, 91–93]. In the present work, we decided to look at the impact of two parameters, the Damköhler number in the solid phase and the dimensionless IR-drop, over the error. Particularly, we varied the charging C-rate from $C/5$ up to $1C$, and we increased the solid diffusion coefficient by one and two orders of magnitude.

Chapter 4

Results

4.1 Morphology comparison

The focus of the first part of the present work is the development of a computational workflow aimed at the study of the operational behavior of a lithium ion battery. We focus in particular on the effect of different geometrical shapes on the particles constituting the anode, to observe the impact of the electrode morphology in the discharge process. The three systems analyzed are: A) mono-disperse spheres, B) poly-disperse spheres, and C) poly-disperse ellipsoids. For each system, the discharge curve and the concentration of intercalated lithium were analyzed, considering also the effect of different initial conditions. In particular, we considered four different discharge rates: C/10, C/5, C/3, and 1C. This step, the generation of the model of the electrode geometry, is the point in this workflow where experimental data can most effectively inform the computational model. In this case, the PSD was obtained from image analysis of FESEM scans: an alternative could be to obtain the whole PSD directly via static light scattering. Moreover, with a scanning electron microscope, it is possible to obtain more information about particle morphology, giving the opportunity to create electrodes composed by particles with different shapes. In order to have a good validation of the model analyzed, the discharge curves have been compared with an experimental one. All the information needed to reproduce the experiments (materials adopted for the battery assembly, experimental equipment for the analysis, and other technical details) are available in the Appendix B. The experimental discharges were made with a current value such as to complete the process in 10 hours. Therefore, the comparison is performed only with the model discharged at C/10. This hypothesis is necessary for one important reason: discharge cycles at a higher C-rate would show a marked effect of the polarization phenomena, due to an higher internal resistance, that are not taken into account in the present work. The main operating conditions and geometrical features are summarized in Tab. 3.1. The physical coefficients reported for the liquid phase are averaged values, since they are function of the lithium-ion concentration and the complete curve is available in the script itself. Tab. 4.1 compares the average porosity of the anode measured experimentally from three independent experiments (affected by an experimental error of approximately 10 %) with the values obtained from the three digital replicas. We would like to underline again that the porosity values were evaluated from 2D FESEM images, as previously reported in Sec. 3.2. As it can be seen, both the polydisperse ellipsoids and the polydisperse spheres fall within the experimental range, with the porosity of the monodisperse spheres replica, falling outside of this range. Nonetheless, given the numerical dispersion of the experimental data, from this porosity evaluation both polydisperse spheres and ellipsoids would result in geometrically fitting models. Significantly different are instead the resulting computational specific surface, calculated as the ratio between the solid-liquid interface area and the electrode volume, and the tortuosity, evaluated by the TauFactor algorithm on Matlab [94], in the separator-current collector direction. We did not report any experimental value for a comparison since the common specific surface data available for commercial graphite particles, and already reported in Section 3.1, considers the internal channel connection which are not directly accessible or represented in the computational model developed in COMSOL. As a result, the computational values in Tab 4.1 are significantly lower than the experimental values. As it will be shown later, the latter choice will prove more accurate from a physical evaluation standpoint. What can be already be inferred from these preliminary results, is that by using

Geometry	**Exp. porosity**	**Comp. porosity**	**Comp. specific area [m^2/m^3]**	**Tortuosity**
Monodisperse spheres	0.300	0.376	9.29×10^5	2.05
Polydisperse ellipsoids		0.271	9.90×10^5	7.8
Polydisperse spheres		0.301	5.93×10^5	2.33

Table 4.1 Geometrical descriptors of the three types of reconstructed electrodes, compared with the experimental value.

a simplified model considering spherical shapes of uniform size for the particles results in an electrode that has very different characteristics from the real one. After these considerations regarding the pure geometrical aspect of the electrodes we can look at the physical behaviors. In the following figures, the continuous red line will represent the system with ellipsoidal particles, the blue dashed dot line will refer to the electrode with polydisperse spheres, the green dashed line to the system formed by monodisperse particles, and the black dotted line will refer to the experimental discharge curve. For a better visualization, we chose a double-logarithm plot to show the results. Indeed, this representation highlights the different stages of graphite lithiation. First of all, the discharge curves at C-rate $= C/10$ have been compared with an experimental curve obtained in our laboratory. The experimental curve has been obtained from the first discharge cycle of a coin cell. In this way, and thanks also to the low current value, we can neglect degradation effects. Fig. 5 shows that the three systems analyzed reproduce the experimental discharge curve reasonably well. This result has two important implications: first, it serves as a second confirmation, after the geometrical analysis in Tab. 2, that the three generated electrodes are similar and comparable in structure. Second, it suggests that the morphology has a limited impact on the discharge behavior when the current is low. To further quantify the deviation between the experimental discharge curve and the computational predictions, we calculated the root mean square error (RMSE) using Eqn. 4.1:

$$\mathrm{RMSE} = \sqrt{\sum_{i=1}^{N} (y_{model,i} - y_{experiment,i})^2} \tag{4.1}$$

where $y_{model,i}$ and $y_{experiment,i}$ represent the simulated and experimental data points, respectively. Table 4.2 reports the RMSE values for the three systems. Although the system with ellipsoidal particles shows a slightly higher RMSE (0.3861) compared to the monodisperse (0.3638) and polydisperse (0.3046) spherical systems, the differences are moderate and do not compromise the main conclusions of this work. The use of a double logarithmic scale in Fig. 5 was intentionally chosen to emphasize these differences, highlighting the superior representativeness of the ellipsoidal geometry in replicating the actual discharge behavior of the system.

System	**RMSE**
Ellipsoidal	0.3861
Monodisperse	0.3638
Polydisperse	0.3046

Table 4.2 Root mean square error for the three simulated discharge curves with respect to the experimental one.

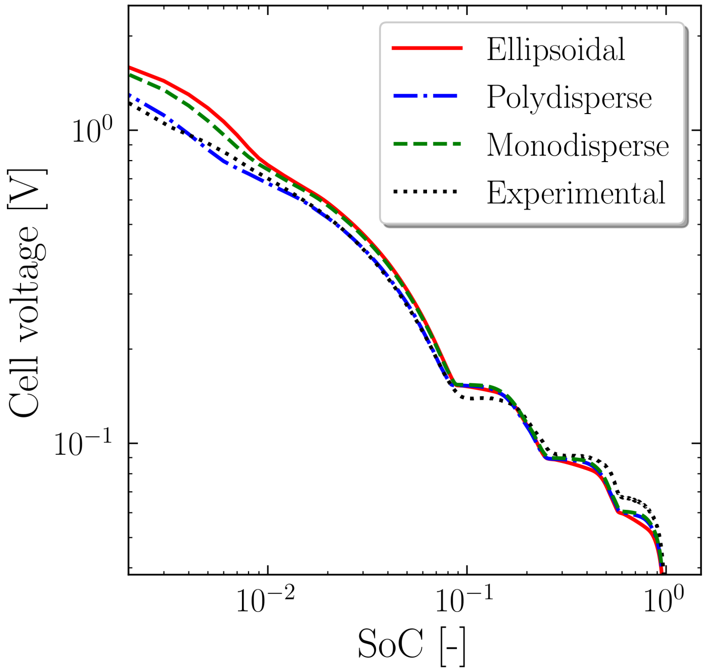

Fig. 4.1 Discharge curves as a function of the SoC, comparison between modeling and experimental results. The continuous red line represents the system with ellipsoidal particles, the blue dashed dot line refers to the electrode with polydisperse spheres, the green dashed line alludes to the system formed by monodisperse particles, and the black dotted line refers to the experimental discharge curve.

If we apply an higher value of the electric current, moving to higher C-rates, we start see some differences. In particular, from Fig. 4.2, we can immediately notice that an increase in the C-rate value leads to an increment in the difference between the curves. If we want to go more into detail, when C-rate $= C/10$ the three curves are almost overlapping, even if there is a small difference between the polydisperse system and the other two. If we look at the cases b) and c), where C-rate $= C/5$ and

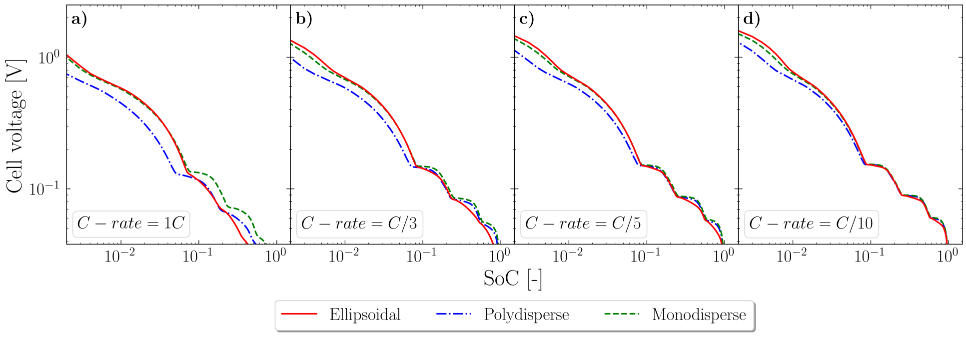

Fig. 4.2 Discharge curves as a function of the SoC. The continuous red line represents the system with ellipsoidal particles, the blue dashed dot line refers to the electrode with polydisperse spheres, and the green dashed line to the system formed by monodisperse particles. a) C-rate $= C/10$; b) C-rate $= C/5$; c) C-rate $= C/3$.

C-rate $= C/3$ respectively, also the curve of monodisperse spheres begins to diverge from the electrode with ellipsoidal particles and this difference is more appreciable close to the graphite lithiation state changes, occurring at the points with a visually evident change in slope of the curves. The biggest differences appear when we have a current value such as C-rate$= 1C$. Now, also the system with monodisperse particles start to diverge from the system with ellipsoids, in particular at the end of the discharge process. The contour plots are taken at half of the discharge time, so when SoC=0.5, and in each row, the half cells are discharged at the same C-rate value.

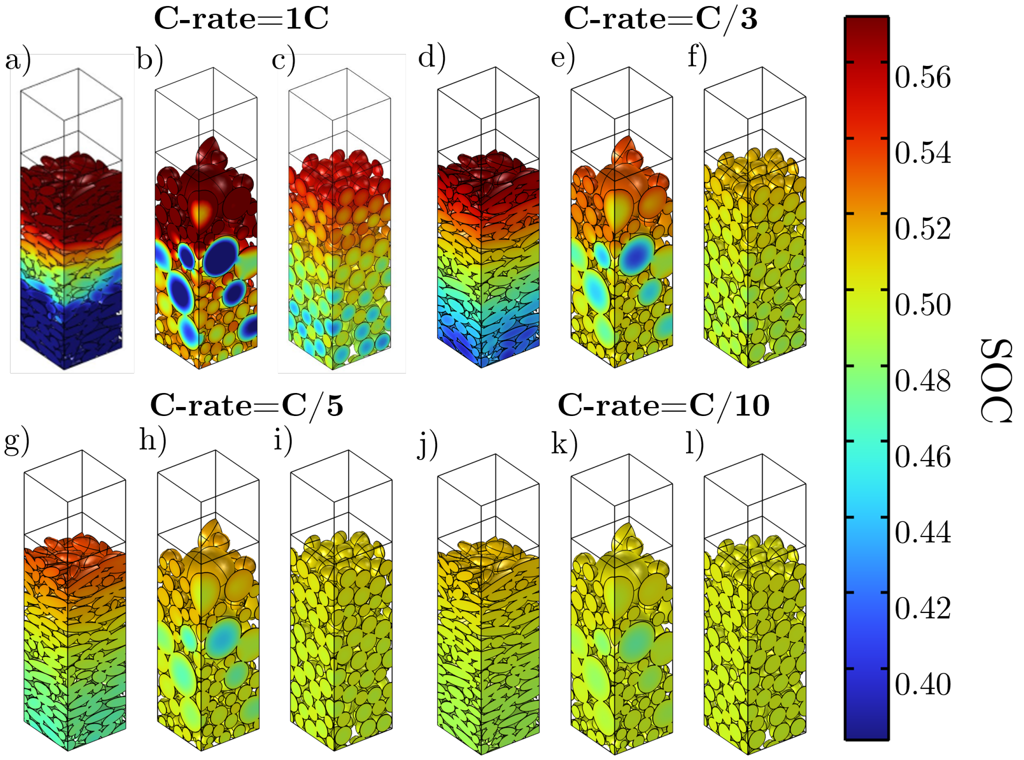

Fig. 4.3 Local intercalated lithium concentration within the electrode. Images taken at half discharge, SoC=50%. (a, b, c): C-rate=1C; (d, e, f): C-rate=C/3; (g, h, i): C-rate=C/5; (j, k, l): C-rate=C/10.

As it is shown by the figure, even if the three systems are at the same total lithiation level, the local concentration of lithium is very different. When the discharge current is low (first row), the vertical gradient of concentration in the electrode is almost null in all the systems. It is easy to notice that the half cell with ellipsoids reaches concentration values quite higher close to the separator, and the concentration field is more or less constant. On the other hand, the spherical polydisperse system has a negligible concentration gradient along the Z direction, but there is a small radial gradient within the biggest particles. If we look at the second row, in which the current value is such that discharge occurs in 5 hours, the differences explained above are more evident. The first half cell shows a marked vertical gradient. Instead, the second system start to show a vertical gradient of concentration but also the radial one is increased. The electrode with monodisperse particles does not show almost any difference from the previous case: even if the discharge current value is double, the concentration gradient value is close to zero as in the previous case.

When we move to the third row, with a C-rate $= C/3$ the anode made of ellipsoidal particles exhibits a strong gradient from top to bottom, but one important consideration is related to the radial gradient that is practically null. By contrast, the second electrode shows a very evident radial gradient as well as a vertical gradient. Finally, the electrode with monodisperse particles continue showing a null gradient, both radial and vertical. The last row, with C-rate$= 1C$ underlines better the consideration carried out for the previous case. Now, the applied current value is so high that also the system with monodisperse spheres shows a vertical gradient of concentration. Furthermore, the radial gradient in the biggest spherical particle in case k) is more evident. Looking at the system j) with ellipsoidal particles, it is clear that the vertical gradient is extremely evident and with the concentration behavior that varies a lot along the separator-current collector direction.

The presence of the vertical gradient, widely observed with X-ray analysis [95], is caused by the increased tortuosity within the electrodes, which is effectively higher for configurations with ellipsoidal particles, as shown in Tab. 4.1. The ellipsoidal particles, due to their elongated shape, create a more complex network of pathways through the electrolyte, forcing lithium ions to take longer paths compared to systems with spherical particles. This geometric constraint leads to a reduction in the effective diffusivity in the electrolyte phase and contributes to the observed vertical gradient in concentration.

The anode made of spheres, both monodisperse and polydisperse, offers a lower hindrance and for this, the local lithiation is almost homogeneous. This clearly demonstrates that only considering polydisperse ellipsoidal particles can result in a realistic representation of electrodes. We can therefore infer that the local and instant concentration profiles of intercalated lithium in the electrode, of lithium in the electrolyte and, therefore, of lithium at the electrode-electrolyte interface, are more accurately predicted only with a realistic anode (or electrode in general) geometrical representation. Since all irreversible degradation phenomena occur locally and depend on local concentrations, only such computational models can accurately describe them. These phenomena, and the SEI formation in particular, will be the focus of our future work.

4.2 Reduced order model validation

In the previous section, we demonstrated the importance of the realistic representation of the electrode morphology. However, full pore-scale models are often slow and require long simulation times, on the order of hours or days. The approach proposed in this work is the application of the homogenization via multiple scale expansion on the microscale governing equation to effectively derive macroscopic fast equations. For the validation, we calculated the volume average of the variables of interest in each unit cell that forms the 3D electrode. Then, we obtained the same variable from the 1D model at the corresponding position of the 3D model, and we evaluated the normalized error. As representative cases, we chose simulations with $C_{rate} = 1C$, that corresponds to $N_{ohm} = 0.0030$. We remember that if the constraints mentioned in Sec. 2.3.2 are satisfied, the error calculated between the 1D upscaled model and the 3D pore-scale model is on the same order of magnitude as the geometrical parameter ε. According to literature, two numbers A and B have the same order of magnitude if $0.1 < A/B < 10$ [96, 97]. We also remember that the homogenized model have been tested against a pore scale model with a solid electrode composed only by spherical particles disposed with a BCC conformation. Indeed, the purpose of this part is to demonstate the validity of the mathematical technique introduced. Testing with ellipsoidal particles, roughness surfaces or complex geometries, will be part of future studies.

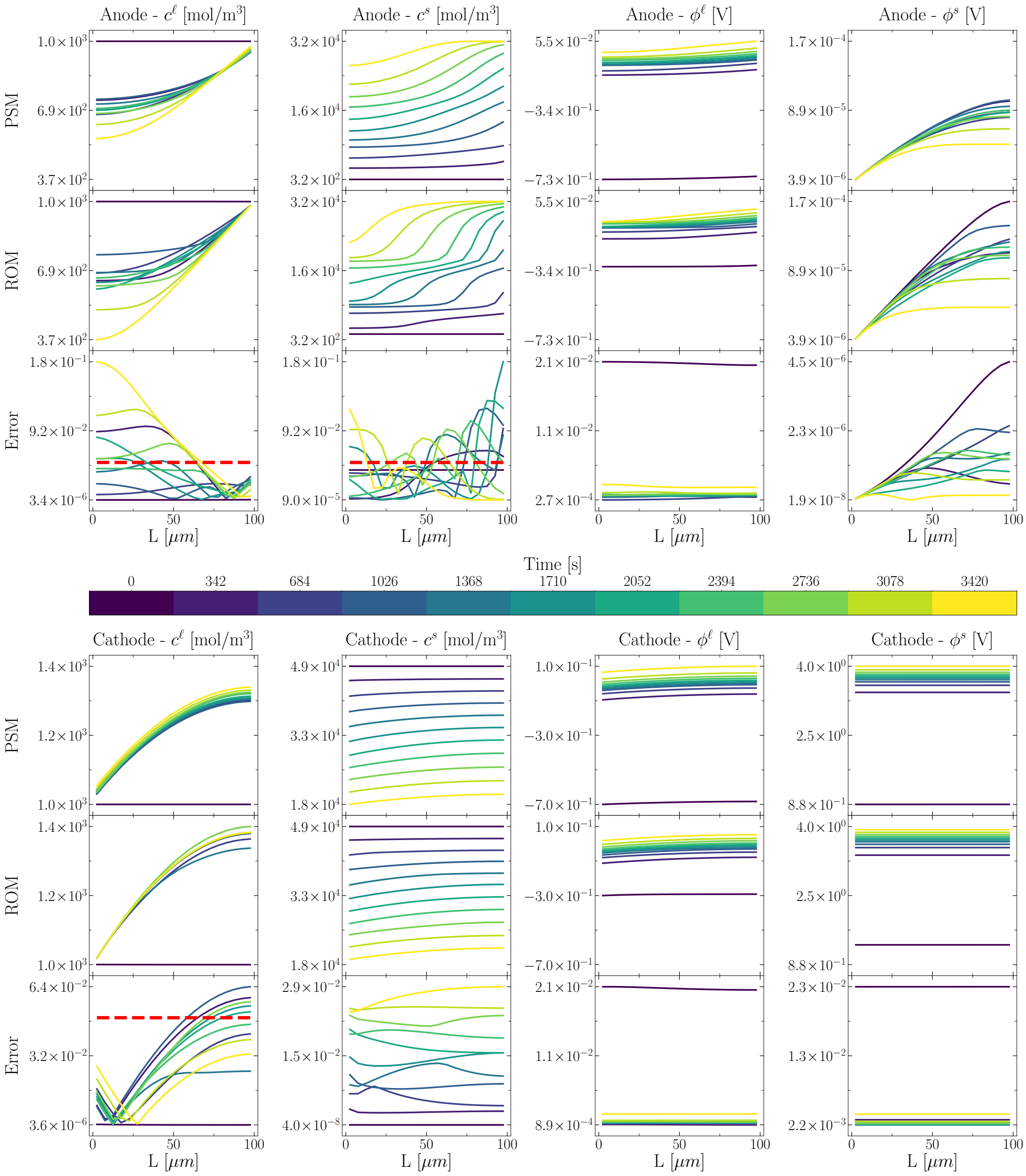

Fig. 4.4 Charge at $C_{rate} = 1C$ and $Da_s = \mathcal{O}(1)$. In the first row of each group of plots, the Pore Scale Model (PSM) is presented, then, in the second one, there is the Reduced Order Model (ROM), and finally the Error between the two methods.

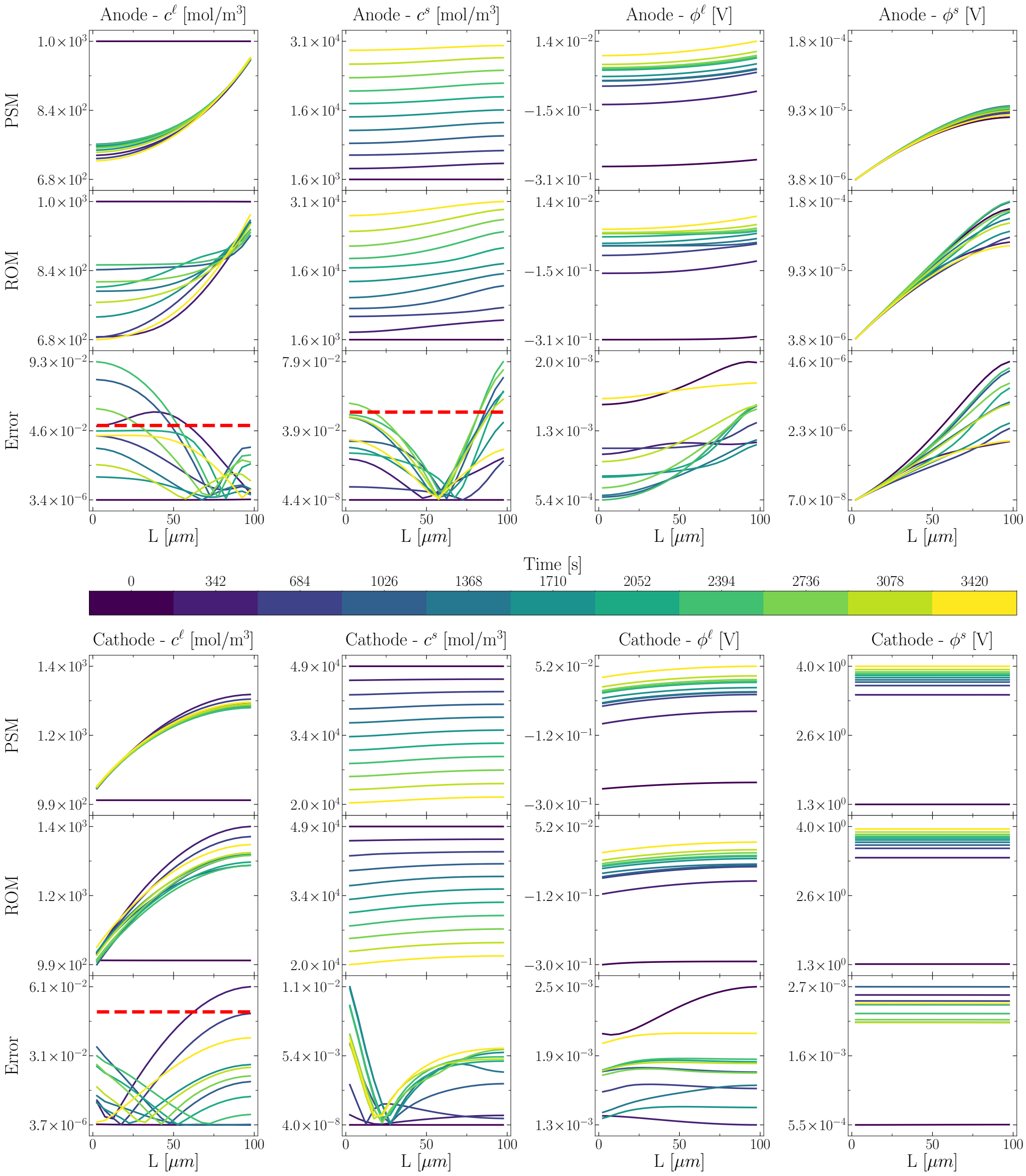

Fig. 4.5 Charge at $C_{rate} = 1C$ and $Da_s = \mathcal{O}(\varepsilon)$. In the first row of each group of plots, the Pore Scale Model (PSM) is presented, then, in the second one, there is the Reduced Order Model (ROM), and finally the Error between the two methods.

As shown by Fig. 4.5, the maximum value of the error, equal to $err = 0.072$, was obtained in the evaluation of the concentration of the intercalated lithium in the anode side. This value is on the same order of magnitude as the geometrical parameter $\varepsilon = 0.05$, as shown by the red dashed line. This significant result proves that the derived mathematical model is predictive and capable of reproducing the pore-scale results with a strong control over the error. On the other hand, if we increase the Damköler number up to $Da = \mathcal{O}(1)$, breaking the constraints, we notice an increase in the maximum error for the intercalated lithium concentration in the anode side up to $err = 0.18$, which is quite higher but still on the same order of magnitude as ε. This result is in line with the theory since homogenization via multiple-scale expansion gives a predictive model, with an error of the same order of magnitude as the geometrical parameter, only if all the constraints are satisfied. If the dimensionless numbers exceeded the applicability regimes' boundaries, it is not possible to predict the error. Indeed, if we look at the case from Fig. 4.6, we notice an error ($err = 0.083$) of the same order as ε even if the operating conditions are outside of the applicability regimes boundaries.

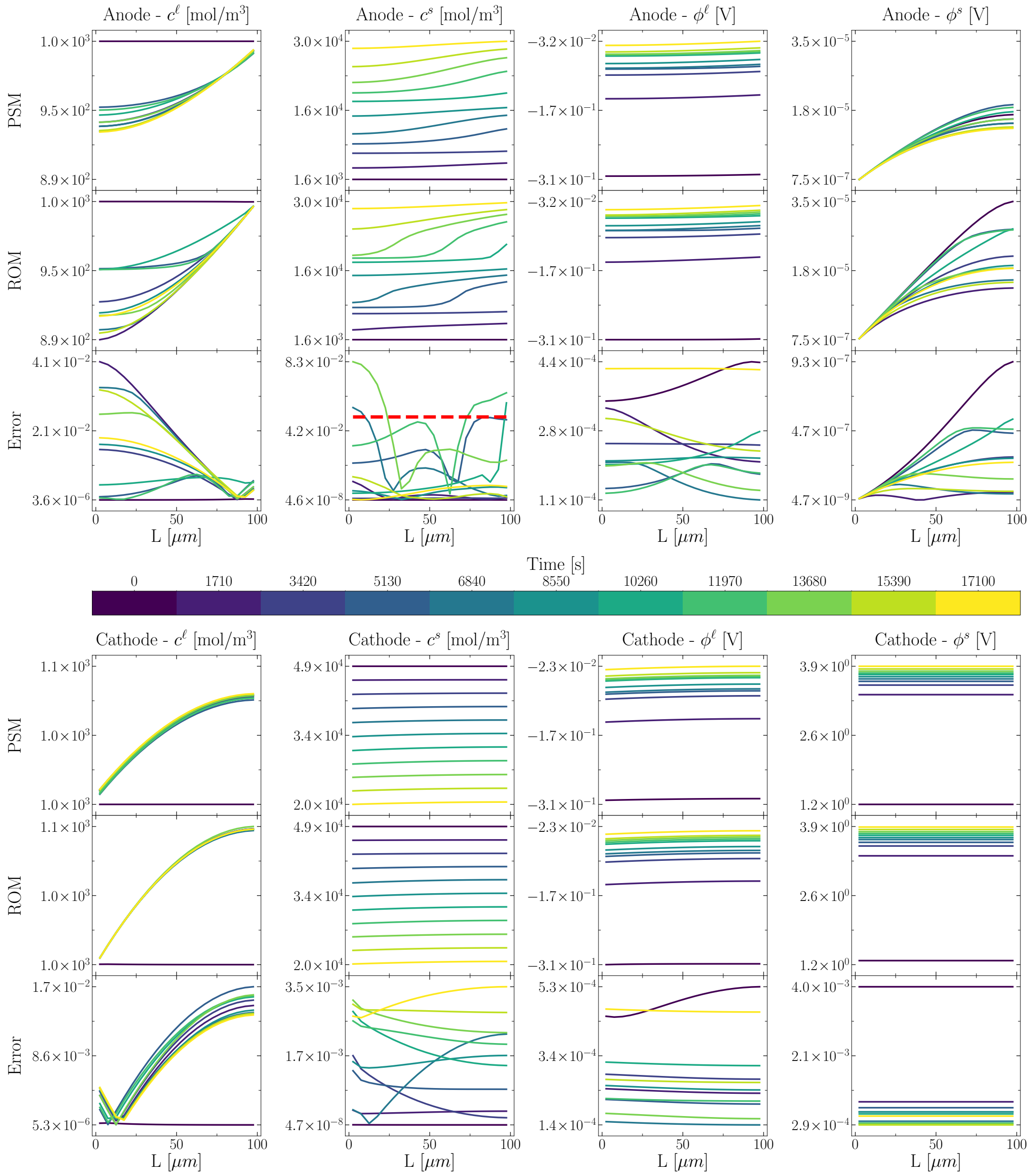

Fig. 4.6 Charge at $C_{rate} = 5C$ and $Da_s = \mathcal{O}(\varepsilon)$. In the first row of each group of plots, the Pore Scale Model (PSM) is presented, then, in the second one, there is the Reduced Order Model (ROM), and finally the Error between the two methods.

However, from Fig. 4.4 we can obtain other important conclusions. First, we notice a high error in lithium-ion concentration in the liquid phase of the anode side, even if we did not modify the dimensionless numbers that characterize this phase. The reason is that lithium-ion batteries are a multiphysics problem, and the variable behavior within the two phases is strictly connected. Therefore, in order to have a predictive model, all the constraints must be respected. Second, we notice that the error is maximum in the middle of the simulation, and then it decreases. This happens because two variables, intercalated lithium concentrations in the two electrodes, are limited: $0 < c_i^s < c_{max,i}^s$, where $i = \{a, c\}$, and therefore the error is limited as well. Thanks to the multiphysics nature of these equations, the error is also limited. This aspect, combined with the fact that constraints 2.3.2 are sufficient but not necessary conditions, allows the model to work very well also out of the applicability regimes, as shown by the case from Fig.4.6. Fig. 4.7 summarizes the errors for all the cases analyzed.

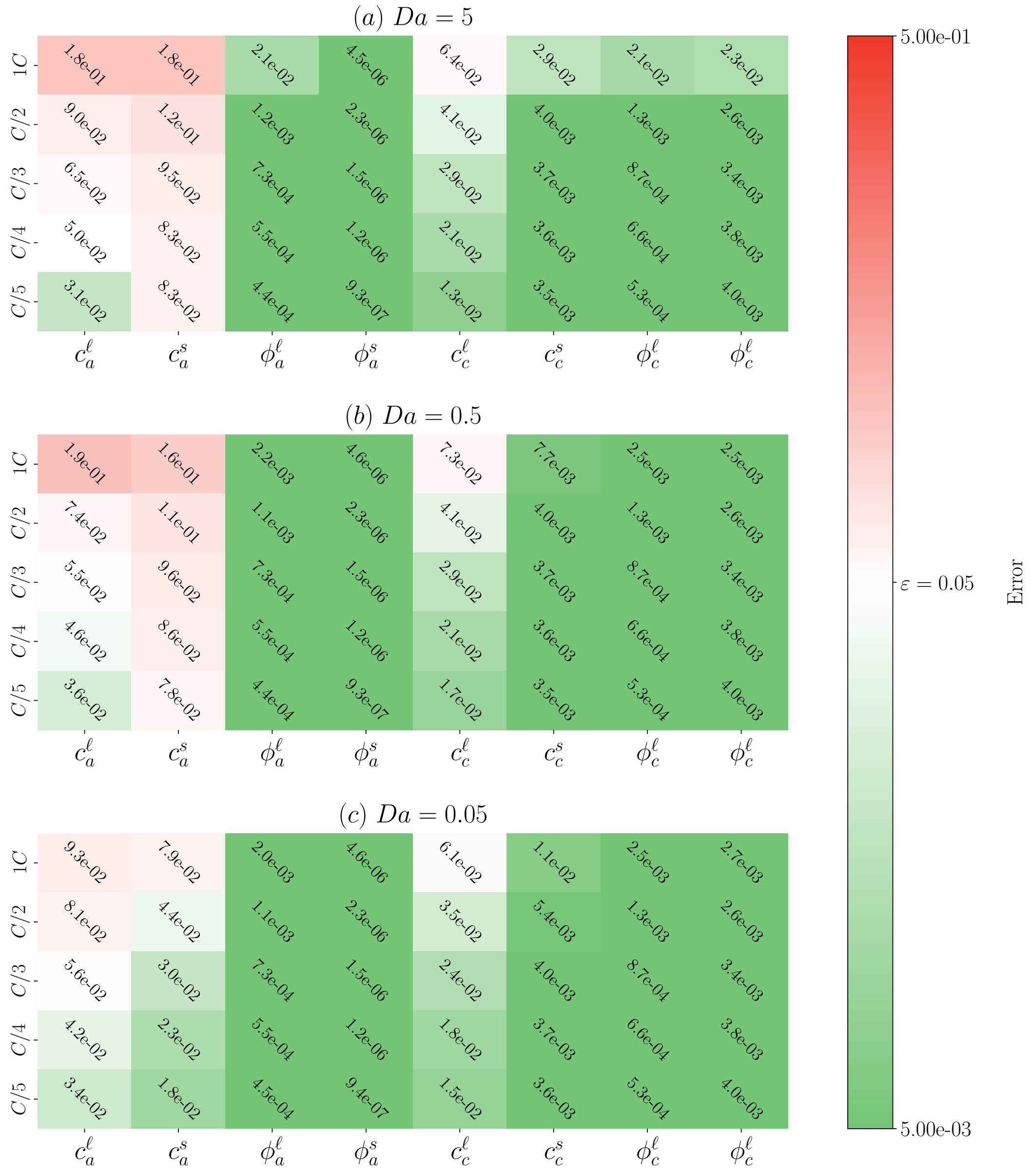

$(a)\ Da = 5$

	c_a^ℓ	c_a^s	ϕ_a^ℓ	ϕ_a^s	c_c^ℓ	c_c^s	ϕ_c^ℓ	ϕ_c^ℓ
1C	1.8e-01	1.8e-01	2.1e-02	4.5e-06	6.4e-02	2.9e-02	2.1e-02	2.3e-02
$C/2$	9.0e-02	1.2e-01	1.2e-03	2.3e-06	4.1e-02	4.0e-03	1.3e-03	2.6e-03
$C/3$	6.5e-02	9.5e-02	7.3e-04	1.5e-06	2.9e-02	3.7e-03	8.7e-04	3.4e-03
$C/4$	5.0e-02	8.3e-02	5.5e-04	1.2e-06	2.1e-02	3.6e-03	6.6e-04	3.8e-03
$C/5$	3.1e-02	8.3e-02	4.4e-04	9.3e-07	1.3e-02	3.5e-03	5.3e-04	4.0e-03

$(b)\ Da = 0.5$

	c_a^ℓ	c_a^s	ϕ_a^ℓ	ϕ_a^s	c_c^ℓ	c_c^s	ϕ_c^ℓ	ϕ_c^ℓ
1C	1.9e-01	1.6e-01	2.2e-03	4.6e-06	7.3e-02	7.7e-03	2.5e-03	2.5e-03
$C/2$	7.4e-02	1.1e-01	1.1e-03	2.3e-06	4.1e-02	4.0e-03	1.3e-03	2.6e-03
$C/3$	5.5e-02	9.6e-02	7.3e-04	1.5e-06	2.9e-02	3.7e-03	8.7e-04	3.4e-03
$C/4$	4.6e-02	8.6e-02	5.5e-04	1.2e-06	2.1e-02	3.6e-03	6.6e-04	3.8e-03
$C/5$	3.6e-02	7.8e-02	4.4e-04	9.3e-07	1.7e-02	3.5e-03	5.3e-04	4.0e-03

$(c)\ Da = 0.05$

	c_a^ℓ	c_a^s	ϕ_a^ℓ	ϕ_a^s	c_c^ℓ	c_c^s	ϕ_c^ℓ	ϕ_c^ℓ
1C	9.3e-02	7.9e-02	2.0e-03	4.6e-06	6.1e-02	1.1e-02	2.5e-03	2.7e-03
$C/2$	8.1e-02	4.4e-02	1.1e-03	2.3e-06	3.5e-02	5.4e-03	1.3e-03	2.6e-03
$C/3$	5.6e-02	3.0e-02	7.3e-04	1.5e-06	2.4e-02	4.0e-03	8.7e-04	3.4e-03
$C/4$	4.2e-02	2.3e-02	5.5e-04	1.2e-06	1.8e-02	3.7e-03	6.6e-04	3.8e-03
$C/5$	3.4e-02	1.8e-02	4.5e-04	9.4e-07	1.5e-02	3.6e-03	5.3e-04	4.0e-03

Fig. 4.7 Cases analyzed: the color bar represents the error value.

From the heatmap, we can conclude that the 1D upscaled model well reproduces the variables' behaviors. Indeed, cases that are out of the applicability regimes' boundaries have a low value for the error, compared to the scaling parameter. Furthermore, we noticed that the variables that most affect the error are the concentration in liquid and solid phases in the anode side. We explain this because of the equilibrium potential curve. The one referred to as the graphite anode has several inflection points, and we notice that the error rises when one of these points is reached by the simulation. This indicated the direction for further studies, by testing several materials and looking for a relation between the inflection points and the error.

Chapter 5

Conclusions

This PhD thesis focused on the computational simulation of the electrochemical processes involved during the charge-discharge of a lithium ion battery. Nowadays, this topic has a huge interest in the research world but, or precisely because of that, still show many aspects where efforts in their improvement would lead to great practical gains. In particular, there are two aspects that we considered to be of primary interest and on which we focused our study. The first point is the electrode morphology reproduction and the second is the computation time, especially as their requirements grow to satisfy the detailed description as introduced in the first part. Therefore, in the first part we addressed the limitations of traditional lithium-ion battery modeling, particularly highlighting the importance of accurate electrode geometrical representation. We examined the differences between conventional spherical approximations and the actual shapes of graphite particles, demonstrating that the anisotropic geometry of graphite significantly affects the electrochemical behavior of batteries. By using FESEM images and electrochemical half-cell battery models, we were able to show how a precise representation of graphite particles improves the understanding of intra-particle lithiation processes. Additionally, we developed an automatic script to replicate electrodes with various physical and geometric properties, allowing detailed comparisons between different types of graphite and different geometric configurations. The results highlight that adopting geometrically accurate models can not only improve battery performance predictions but also optimize the study for their design for greater efficiency and longevity. Geometry directly influence the particle arrangements, the porosity, and the specific surface, which has a fundamental importance in an electrochemical model governed by a superficial reaction. The altered ion distribution causes local variations in reaction rates across the electrode, even under uniform current conditions. In contrast, the spherical-particle model promotes more isotropic transport properties and more uniform electrochemical reactions, leading to a flatter lithium concentration profile. This work paves the way for further research on the influence of electrode morphology and supports the idea that increased attention to particle geometry can lead to significant advancements in LiB technology. Ultimately, improved models that consider the true geometries of electrodes could play a crucial role in the evolution of LiBs, significantly contributing to the achievement of global energy sustainability goals. This work aimed to accurately represent the physical and morphological characteristics of LiB electrodes. During the first part of this work, we noticed another weak point of electrochemical models, closely related to the first one. Improving the accuracy of the electrode morphology inevitably rise the computational cost of the whole simulation. To address this limitation we searched for a way to reduce the computational time without compromising the geometry realism. Our choice fell on the homogenization via multiple scale expansion. This mathematical technique allows the evaluation of effective transport and reaction coefficients, informed by the morphology under consideration, that appear in fast macroscopic equations rigorously derived from microscopical ones. Therefore, the second objective of this thesis work was the methodical derivation of the macroscopic governing equations for mass and charge transport in a lithium-ion battery, both in liquid and solid phases, followed by their validation. In fact, even though the derivation had already been carried out in literature, it was considered incomplete or incorrect. To do so, we started from the pore-scale microscopic equations and applied the homogenization via multiple-scale expansion to the transport equations and their boundary conditions. Then, the macroscopic electrical conductivity and diffusivity coefficients were evaluated by solving the unit cell problem to take into account the morphology effect, and we formalized the applicability regime conditions with appropriate dimensionless numbers. Finally, we validated the one-dimensional continuum model by computing the error with respect to a corresponding three-dimensional pore-scale simulation. According to the mathematical derivation, the resulting error should be of the same order of magnitude as the geometrical parameter $\varepsilon = \ell/L$. This parameter is the ratio between the characteristic length of a periodic unit cell and the electrode length. Indeed, two mainly hypothesis of the homogenization are the periodicity of the domain of interest and the separation of scale between the domain of interest and the characteristic pore-scale length. These hypotheses are both formalized with $\varepsilon \to 0$. For the validation, we built a 3D model with two solid electrodes divided by the separator and submerged in the liquid electrolyte. Each electrode is composed of twenty unit cells and therefore we expected an error of the order of $\varepsilon = \ell/L = 0.05$. We solved the mass and charge transport equations in the 3D pore-scale model and the corresponding macroscale version in a 1D continuous model. Then, we evaluated the error as $err = |\langle\psi\rangle_{rod} - \langle\psi\rangle_{ps}|$ where $\psi = \{c^s; c^\ell; \phi^s; \phi^\ell\}$ in both in the anode and in the cathode sides. We demonstrated that, if the analyzed system falls into the applicability regimes, the 1D continuous model well reproduces the results of the 3D pore-scale model with an error of the same order of magnitude as ε. Moreover, we proved that the constraints imposed by the applicability regimes are a sufficient but not necessary condition. Indeed, in some of the cases analyzed we noticed an error of order ε even if the system was outside of the applicability regimes limits. Out of these boundaries is impossible to predict the error, but this could even be of the same order of magnitude as ε or lower. The derived model is accurate enough to be incorporated in a Battery Mangement System software to predict the SoC, the time of charge. There are numerous and diverse possibilities for future development in this field, starting from the simplifying assumptions that we have adopted for the present study. Specifically, the use of idealized particle geometries, with a smooth shape or a fixed maximum thickness, simplifies the highly irregular and rough morphology of real graphite particles. Furthermore, our simulations do not incorporate electrochemical degradation mechanisms such as SEI formation or lithium plating, which can play a significant role during long-term cycling. We also neglect thermal effects and mechanical rearrangement that may arise in fast charge and very high inner current values. Future work should aim to address these limitations by incorporating realistic particle shapes, electrochemical aging phenomena, like SEI formation and growth, and thermal effects into the simulation framework. Exploring these phenomena with a too approximate geometry would lead to a useless simulation that could not help in the design of new batteries. This would provide a deeper understanding of the wear and tear processes that affect battery performance over time. Additionally, incorporating thermal effects into the models could offer insights into how temperature variations impact the efficiency and longevity of the batteries. We demonstrated how the computational model well reproduces the realistic electrochemical process and the potential of mathematical techniques to speed up the simulation process. Such fast and accurate models has the potential to become, in the near future, a powerful weapon to precisely plan an experimental campaign, minimizing both time and resources. Moreover, having a computational script that can automatize the whole process, starting from the electrode generation, going through the effective coefficient evaluation, to ends with the concentration and electric potential fields within the battery, would be a huge support in the performance evaluation. By pursuing these lines of research, we can further highlight the necessity of precise *in-silico* representations. Such detailed models are crucial for comprehensively understanding the complex interactions between the various physical phenomena occurring within LiBs. These advancements could lead to significant improvements in battery design, performance, and safety, ultimately contributing to the development of more reliable and efficient energy storage systems.

References

[1] M. S. Whittingham. Electrical energy storage and intercalation chemistry. *Science*, 192(4244):1126–1127, 1976.

[2] K. Mizushima, P.C. Jones, P.J. Wiseman, and J.B. Goodenough. Lixcoo2 (0<x<-1): A new cathode material for batteries of high energy density. *Materials Research Bulletin*, 15(6):783–789, 1980.

[3] Akira Yoshino, Kenichi Sanechika, and Takayuki Nakajima. Secondary battery. US Patent 4668595, may 1987. Assignee: Asahi Kasei Kogyo Kabushiki Kaisha. Filed 1986-05-09; priority JP 60-97695 (1985-05-10) and JP 60-100101 (1985-05-11).

[4] J.M. Tarascon and Michel Armand. Issues and challenges facing rechargeable lithium batteries. *Nature*, 414:359–67, 12 2001.

[5] Saskia Ziemann, Daniel B. Müller, Liselotte Schebek, and Marcel Weil. Modeling the potential impact of lithium recycling from ev batteries on lithium demand: A dynamic mfa approach. *Resources, Conservation and Recycling*, 133:76–85, 2018.

[6] Yanyan Zhao, Oliver Pohl, Anand Bhatt, Gavin Collis, Peter Mahon, Thomas Rüther, and Anthony Hollenkamp. A review on battery market trends, second-life reuse, and recycling. *Sustainable Chemistry*, 2:167–205, 03 2021.

[7] Chengjian Xu, Qiang Dai, Linda Gaines, Mingming Hu, Arnold Tukker, and Bernhard Steubing. Future material demand for automotive lithium-based batteries. *Communications Materials*, 1(1):99, Dec 2020.

[8] Hong Li. Practical evaluation of li-ion batteries. *Joule*, 3(4):911–914, 2019.

[9] Xuekun Lu, Antonio Bertei, Donal P. Finegan, Chun Tan, Sohrab R. Daemi, Julia S. Weaving, Kieran B. O'Regan, Thomas M. M. Heenan, Gareth Hinds, Emma Kendrick, Dan J. L. Brett, and Paul R. Shearing. 3d microstructure design of lithium-ion battery electrodes assisted by x-ray nano-computed tomography and modelling. *Nature Communications*, 11(1):2079, Apr 2020.

[10] Abhay Gupta and Arumugam Manthiram. Designing advanced lithium-based batteries for low-temperature conditions. *Advanced Energy Materials*, 10(38):2001972, 2020.

[11] Dana Thompson, Jennifer Hartley, Simon Lambert, Muez Shiref, Gavin Harper, Emma Kendrick, Paul Anderson, Karl Ryder, Linda Gaines, and Andrew Abbott. The importance of design in lithium ion battery recycling -a critical review. *RSC Green Chemistry*, 22:7585–7603, 10 2020.

[12] Paul A. Nelson, Danilo J. Santini, and James Barnes. Factors determining the manufacturing costs of lithium-ion batteries for phevs. *World Electric Vehicle Journal*, 3(3):457–468, 2009.

[13] Alessio Lombardo Pontillo, Marco Ferrari, Marcello Rospiccio, and Antonio Buffo. Molecular modeling of the adsorption of an egg yolk protein on a water–oil interface. *Langmuir*, 40(7):3596–3605, 2024.

[14] Xiangchun Zhang, Wei Shyy, and Ann Marie Sastry. Numerical simulation of intercalation-induced stress in li-ion battery electrode particles. *Journal of The Electrochemical Society*, 154(10):A910, jul 2007.

[15] Alejandro A. Franco. Multiscale modelling and numerical simulation of rechargeable lithium ion batteries: concepts, methods and challenges. *RSC Adv.*, 3:13027–13058, 2013.

[16] Alessio Lombardo Pontillo, Agnese Marcato, Daniele Versaci, Daniele Marchisio, and Gianluca Boccardo. Comparative analysis via cfd simulation on the impact of graphite anode morphologies on the discharge of a lithium-ion battery. *Batteries*, 11(7), 2025.

[17] Graham M. Goldin, Andrew M. Colclasure, Andreas H. Wiedemann, and Robert J. Kee. Three-dimensional particle-resolved models of li-ion batteries to assist the evaluation of empirical parameters in one-dimensional models. *Electrochimica Acta*, 64:118–129, 2012.

[18] Marc Doyle, Thomas F. Fuller, and John Newman. The importance of the lithium ion transference number in lithium/polymer cells. *Electrochimica Acta*, 39(13):2073–2081, 1994.

[19] Marc Doyle, Thomas F. Fuller, and John Newman. Modeling of galvanostatic charge and discharge of the lithium/polymer/insertion cell. *Journal of The Electrochemical Society*, 140(6):1526, jun 1993.

[20] Ali Jokar, Barzin Rajabloo, Martin Désilets, and Marcel Lacroix. Review of simplified pseudo-two-dimensional models of lithium-ion batteries. *Journal of Power Sources*, 327:44–55, 2016.

[21] Gang Qiu, C.R. Dennison, K.W. Knehr, E.C. Kumbur, and Ying Sun. Pore-scale analysis of effects of electrode morphology and electrolyte flow conditions on performance of vanadium redox flow batteries. *Journal of Power Sources*, 219:223–234, 2012.

[22] D. D. L. Chung. Review graphite. *Journal of Materials Science*, 37(8):1475–1489, Apr 2002.

[23] N Deprez and D S McLachlan. The analysis of the electrical conductivity of graphite conductivity of graphite powders during compaction. *Journal of Physics D: Applied Physics*, 21(1):101, jan 1988.

[24] Laura Gottschalk, Jannes Müller, Alexander Schoo, Ernesto Baasch, and Arno Kwade. Spherical graphite anodes: Influence of particle size distribution and multilayer structuring in lithium-ion battery cells. *Batteries*, 10(2), 2024.

[25] Lars Bläubaum, Fridolin Röder, Christine Nowak, Hoon Seng Chan, Arno Kwade, and Ulrike Krewer. Impact of particle size distribution on performance of lithium-ion batteries. *ChemElectroChem*, 7(23):4755–4766, 2020.

[26] Hanqing Yu, Lisheng Zhang, Wentao Wang, Kaiyi Yang, Zhengjie Zhang, Xiang Liang, Siyan Chen, Shichun Yang, Junfu Li, and Xinhua Liu. Lithium-ion battery multi-scale modeling coupled with simplified electrochemical model and kinetic monte carlo model. *iScience*, 26(9):107661, 2023.

[27] Xuekun Lu, Marco Lagnoni, Antonio Bertei, Supratim Das, Rhodri E. Owen, Qi Li, Kieran O'Regan, Aaron Wade, Donal P. Finegan, Emma Kendrick, Martin Z. Bazant, Dan J. L. Brett, and Paul R. Shearing. Multiscale dynamics of charging and plating in graphite electrodes coupling operando microscopy and phase-field modelling. *Nature Communications*, 14(1):5127, Aug 2023.

[28] Lars Bläubaum, Fridolin Röder, Christine Nowak, Hoon Seng Chan, Arno Kwade, and Ulrike Krewer. Impact of particle size distribution on performance of lithium-ion batteries. *ChemElectroChem*, 7(23):4755–4766, 2020.

[29] Timo Danner, Madhav Singh, Simon Hein, Jörg Kaiser, Horst Hahn, and Arnulf Latz. Thick electrodes for li-ion batteries: A model based analysis. *Journal of Power Sources*, 334:191–201, 2016.

[30] Daniel Westhoff, Ingo Manke, and Volker Schmidt. Generation of virtual lithium-ion battery electrode microstructures based on spatial stochastic modeling. *Computational Materials Science*, 151:53–64, 2018.

[31] Lea Sophie Kremer, Alice Hoffmann, Timo Danner, Simon Hein, Benedikt Prifling, Daniel Westhoff, Christian Dreer, Arnulf Latz, Volker Schmidt, and Margret Wohlfahrt-Mehrens. Manufacturing process for improved ultra-thick cathodes in high-energy lithium-ion batteries. *Energy Technology*, 8(2):1900167, 2020.

[32] Simon Hein, Timo Danner, Daniel Westhoff, Benedikt Prifling, Rares Scurtu, Lea Kremer, Alice Hoffmann, André Hilger, Markus Osenberg, Ingo Manke, Margret Wohlfahrt-Mehrens, Volker Schmidt, and Arnulf Latz. Influence of conductive additives and binder on the impedance of lithium-ion battery electrodes: Effect of morphology. *Journal of The Electrochemical Society*, 167(1):013546, jan 2020.

[33] Zhe Deng, Xing Lin, Zhenyu Huang, Jintao Meng, Yun Zhong, Guangting Ma, Yu Zhou, Yue Shen, Han Ding, and Yunhui Huang. Recent progress on advanced imaging techniques for lithium-ion batteries. *Advanced Energy Materials*, 11(2):2000806, 2021.

[34] Xiaosong Huang. Separator technologies for lithium-ion batteries. *Journal of Solid State Electrochemistry*, 15(4):649–662, 2011.

[35] Marie Francine Lagadec, Raphael Zahn, and Vanessa Wood. Characterization and performance evaluation of lithium-ion battery separators. *Nature Energy*, 4(1):16–25, 2019.

[36] Stephen Whitaker. *The Method of Volume Averaging*, volume 13 of *Theory and Applications of Transport in Porous Media*. Springer, 1999.

[37] Ulrich Hornung, editor. *Homogenization and Porous Media*, volume 6 of *Interdisciplinary Applied Mathematics*. Springer, 1997.

[38] Malte A. Peter. Coupled reaction–diffusion processes inducing an evolution of the microstructure: Analysis and homogenization. *Nonlinear Analysis: Theory, Methods & Applications*, 70(2):806–821, 2009.

[39] William G. Gray and Cass T. Miller. Thermodynamically constrained averaging theory approach for modeling flow and transport phenomena in porous medium systems: 7. single-phase megascale flow models. *Advances in Water Resources*, 32(8):1121–1142, 2009.

[40] J.L. Auriault and P.M. Adler. Taylor dispersion in porous media: Analysis by multiple scale expansions. *Advances in Water Resources*, 18(4):217–226, 1995.

[41] Mat Hunt, Ferran Brosa Planella, F. Theil, and W. Widanage. Derivation of an effective thermal electrochemical model for porous electrode batteries using asymptotic homogenisation. *Journal of Engineering Mathematics*, 122:1–27, 06 2020.

[42] F. Ciucci and W. Lai. Derivation of micro/macro lithium battery models from homogenization theory. *Transport in Porous Media*, 87(2):249–282, 2011.

[43] S. Korneev and I. Battiato. A data-driven multiscale framework to estimate effective properties of lithium-ion batteries from microstructure images. *Transport in Porous Media*, 134:173–194, 2020.

[44] I. R. Moyles and A. Madzvamuse. Asymptotic homogenization of a nonlinear reaction–diffusion model for ion transport in porous lithium-ion batteries. *Journal of Mathematical Chemistry*, 57:601–624, 2019.

[45] Harikesh Arunachalam, Simona Onori, and Ilenia Battiato. On veracity of macroscopic lithium-ion battery models. *Journal of The Electrochemical Society*, 162(10):A1940, jul 2015.

[46] I. Battiato and D.M. Tartakovsky. Applicability regimes for macroscopic models of reactive transport in porous media. *Journal of Contaminant Hydrology*, 120-121:18–26, 2011. Reactive Transport in the Subsurface: Mixing, Spreading and Reaction in Heterogeneous Media.

[47] E. Sanchez-Palencia. *Non-Homogeneous Media and Vibration Theory*, volume 127 of *Lecture Notes in Physics*. Springer, 1980.

[48] Andro Mikelic. Homogenization theory and applications to filtration through porous media. In *Homogenization and Applications to Material Sciences*, volume 1534 of *Lecture Notes in Mathematics*, pages 18–68. Springer, 1991.

[49] Alain Bensoussan, Jacques-Louis Lions, and George Papanicolaou. *Asymptotic Analysis for Periodic Structures*. North-Holland, 1978.

[50] Adam M. Boyce, Xuekun Lu, Dan J.L. Brett, and Paul R. Shearing. Exploring the influence of porosity and thickness on lithium-ion battery electrodes using an image-based model. *Journal of Power Sources*, 542:231779, 2022.

[51] L. Bläubaum, F. Röder, C. Nowak, H. S. Chan, A. Kwade, and U. Krewer. Impact of particle size distribution on performance of lithium-ion batteries. *ChemElectroChem*, 7(23):5655–5667, 2020.

[52] Graham M. Goldin, Andrew M. Colclasure, Andreas H. Wiedemann, and Robert J. Kee. Three-dimensional particle-resolved models of li-ion batteries to assist the evaluation of empirical parameters in one-dimensional models. *Electrochimica Acta*, 64:118–129, 2012.

[53] John Newman and Nitash P Balsara. *Electrochemical systems*. John Wiley & Sons, 2021.

[54] Allen J Bard, Larry R Faulkner, and Henry S White. *Electrochemical methods: fundamentals and applications*. John Wiley & Sons, 2022.

[55] A. Latz and J. Zausch. Thermodynamic consistent transport theory of li-ion batteries. *Journal of Power Sources*, 196(6):3296–3302, 2011.

[56] Andrew M. Colclasure and Robert J. Kee. Thermodynamically consistent modeling of elementary electrochemistry in lithium-ion batteries. *Electrochimica Acta*, 55(28):8960–8973, 2010.

[57] Deepak K. Karthikeyan, Godfrey Sikha, and Ralph E. White. Thermodynamic model development for lithium intercalation electrodes. *Journal of Power Sources*, 185(2):1398–1407, 2008.

[58] Peter A Cundall and Otto DL Strack. A discrete numerical model for granular assemblies. *geotechnique*, 29(1):47–65, 1979.

[59] Erwin Coumans. Bullet physics simulation. In *ACM SIGGRAPH 2015 Courses*. Association for Computing Machinery, 2015.

[60] Gianluca Boccardo, Frédéric Augier, Yacine Haroun, Daniel Ferré, and Daniele L. Marchisio. Validation of a novel open-source work-flow for the simulation of packed-bed reactors. *Chemical Engineering Journal*, 279:809–820, 2015.

[61] Stephen Whitaker. Mass transport and reaction in catalyst pellets. *Transport in porous media*, 2(3):269–299, 1987.

[62] J Alberto Ochoa, Pieter Stroeve, and Stephen Whitaker. Diffusion and reaction in cellular media. *Chemical Engineering Science*, 41(12):2999–3013, 1986.

[63] D Ryan, RG Carbonell, and S Whitaker. Effective diffusivities for catalyst pellets under reactive conditions. *Chemical Engineering Science*, 35(1-2):10–16, 1980.

[64] WJ Duncan and AR Collar. Lxxiv. a method for the solution of oscillation problems by matrices. *The London, Edinburgh, and Dublin Philosophical Magazine and Journal of Science*, 17(115):865–909, 1934.

[65] C. A. Felippa. A historical outline of matrix structural analysis: a play in three acts. *Computers & Structures*, 79(14):1313–1324, 2001.

[66] M. J. Turner, R. W. Clough, H. C. Martin, and L. J. Topp. Stiffness and deflection analysis of complex structures. *Journal of the Aeronautical Sciences*, 23(9):805–823, 1956.

[67] R. Courant. Variational methods for the solution of problems of equilibrium and vibrations. *Bulletin of the American Mathematical Society*, 49(1):1–23, 1943.

[68] Mats G Larson and Fredrik Bengzon. *The finite element method: theory, implementation, and applications*, volume 10. Springer Science & Business Media, 2013.

[69] Wolfgang Arendt and Mahamadi Warma. Dirichlet and neumann boundary conditions: What is in between? *Journal of Evolution Equations*, 3(1):119–135, 2003.

[70] Martin J Gander and Gerhard Wanner. From euler, ritz, and galerkin to modern computing. *Siam Review*, 54(4):627–666, 2012.

[71] John Dolbow and Ted Belytschko. Numerical integration of the galerkin weak form in meshfree methods. *Computational mechanics*, 23(3):219–230, 1999.

[72] K Ho-Le. Finite element mesh generation methods: a review and classification. *Computer-aided design*, 20(1):27–38, 1988.

[73] Steffen Petersen, Daniel Dreyer, and Otto von Estorff. Assessment of finite and spectral element shape functions for efficient iterative simulations of interior acoustics. *Computer methods in applied mechanics and engineering*, 195(44-47):6463–6478, 2006.

[74] Talal Rahman and Jan Valdman. Fast matlab assembly of fem matrices in 2d and 3d: Nodal elements. *Applied mathematics and computation*, 219(13):7151–7158, 2013.

[75] Jong Hyun Park, Hana Yoon, Younghyun Cho, and Chung-Yul Yoo. Investigation of lithium ion diffusion of graphite anode by the galvanostatic intermittent titration technique. *Materials*, 14(16), 2021.

[76] E. Markevich, M.D. Levi, and D. Aurbach. Comparison between potentiostatic and galvanostatic intermittent titration techniques for determination of chemical diffusion coefficients in ion-insertion electrodes. *Journal of Electroanalytical Chemistry*, 580(2):231–237, 2005.

[77] Hui Yang, Hyun Joo Bang, and Jai Prakash. Evaluation of electrochemical interface area and lithium diffusion coefficient for a composite graphite anode. *Journal of The Electrochemical Society*, 151(8):A1247, jul 2004.

[78] Jeffrey S. Horner, Grace Whang, David S. Ashby, Igor V. Kolesnichenko, Timothy N. Lambert, Bruce S. Dunn, A. Alec Talin, and Scott A. Roberts. Electrochemical modeling of gitt measurements for improved solid-state diffusion coefficient evaluation. *ACS Applied Energy Materials*, 4(10):11460–11469, 2021.

[79] Arash Rabbani and Saeed Salehi. Dynamic modeling of the formation damage and mud cake deposition using filtration theories coupled with sem image processing. *Journal of Natural Gas Science and Engineering*, 42:157–168, 2017.

[80] C. P. Ezeakacha, A. Rabbani, S. Salehi, and A. Ghalambor. Integrated image processing and computational techniques to characterize formation damage. In *SPE International Conference and Exhibition on Formation Damage Control*, volume SPE International Conference and Exhibition on Formation Damage Control, page D012S007R004, 02 2018.

[81] Victoria Julia Ovejas and Angel Cuadras. Impedance characterization of an lco-nmc/graphite cell: Ohmic conduction, sei transport and charge-transfer phenomenon. *Batteries*, 4(3):43, 2018.

[82] Daniel Müller, Imanol Landa-Medrano, Aitor Eguia-Barrio, Iker Boyano, Idoia Urdampilleta, Iratxe de Meatza, Alexander Fill, and Peter Birke. Electrochemical characterization of bi-layered graphite anodes combining high and low porosity in lithium-ion cells to improve cell performance. *Electrochimica Acta*, 391:138966, 2021.

[83] Ben Rowden and Nuria Garcia-Araez. Estimating lithium-ion battery behavior from half-cell data. *Energy Reports*, 7:97–103, 2021.

[84] Yu-Kai Huang, Jean Pettersson, and Leif Nyholm. Diffusion-controlled lithium trapping in graphite composite electrodes for lithium-ion batteries. *Advanced Energy and Sustainability Research*, 3(8):2200042, 2022.

[85] Vaclav Smilauer. *Yade documentation*. The Yade Project, nov 2021.

[86] S.V. Filippov. Blender software platform as an environment for modeling objects and processes of science disciplines. *Keldysh Institute preprints*, (230):1–42, 2018.

[87] Julen Castillo, Asier Soria-Fernández, Sergio Rodriguez-Peña, Jokin Rikarte, Adrián Robles-Fernández, Itziar Aldalur, Rosalía Cid, Jose Antonio González-Marcos, Javier Carrasco, Michel Armand, Alexander Santiago, and Daniel Carriazo. Graphene-based sulfur cathodes and dual salt-based sparingly solvating electrolytes: A perfect marriage for high performing, safe, and long cycle life lithium-sulfur prototype batteries. *Advanced Energy Materials*, 14(1):2302378, 2024.

[88] Aslihan Örüm Aydin, Franziska Zajonz, Till Günther, Kamil Burak Dermenci, Maitane Berecibar, and Lisset Urrutia. Lithium-ion battery manufacturing: Industrial view on processing challenges, possible solutions and recent advances. *Batteries*, 9(11):555, 2023.

[89] Tobias Hofmann, Daniel Westhoff, Julian Feinauer, Heiko Andrä, Jochen Zausch, Volker Schmidt, and Ralf Müller. Electro-chemo-mechanical simulation for lithium ion batteries across the scales. *International Journal of Solids and Structures*, 184:24–39, 2020. Physics and Mechanics of Random Structures: From Morphology to Material Properties.

[90] Tiejun Liu, Tianyu Zhang, Feng Shen, Zhiwei Wu, Zhengyang Kang, Jun Zheng, Xianglin Li, Jing Zhao, Yan Zhang, Ying Cheng, Kejie Zhao, Yan Wang, and Huolin L. Xin. 3d microstructure design of lithium-ion battery electrodes assisted by x-ray nano-computed tomography. *Nature Communications*, 11(1):2079, 2020.

[91] Suman Basu, Rajkumar S. Patil, Sanoop Ramachandran, Krishnan S. Hariharan, Subramanya Mayya Kolake, Taewon Song, Dukjin Oh, Taejung Yeo, and Seokgwang Doo. Non-isothermal electrochemical model for lithium-ion cells with composite cathodes. *Journal of Power Sources*, 283:132–150, 2015.

[92] Karthik Somasundaram, Erik Birgersson, and Arun Sadashiv Mujumdar. Model for a bipolar li-ion battery module: Automated model generation, validation and verification. *Applied Mathematics and Computation*, 219(4):2231–2245, 2012.

[93] Meng Xu, Zhuqian Zhang, Xia Wang, Li Jia, and Lixin Yang. A pseudo three-dimensional electrochemical–thermal model of a prismatic lifepo4 battery during discharge process. *Energy*, 80:303–317, 2015.

[94] S.J. Cooper, A. Bertei, P.R. Shearing, J.A. Kilner, and N.P. Brandon. Taufactor: An open-source application for calculating tortuosity factors from tomographic data. *SoftwareX*, 5:203–210, 2016.

[95] Koffi P. C. Yao, John S. Okasinski, Kaushik Kalaga, Ilya A. Shkrob, and Daniel P. Abraham. Quantifying lithium concentration gradients in the graphite electrode of li-ion cells using operando energy dispersive x-ray diffraction. *Energy Environ. Sci.*, 12:656–665, 2019.

[96] David Halliday, Robert Resnick, and Jearl Walker. *Fundamentals of Physics*. John Wiley & Sons, Hoboken, NJ, 10th edition, 2013.

[97] Paul A. Tipler and Gene Mosca. *Physics for Scientists and Engineers*. W. H. Freeman and Company, New York, 6th edition, 2008.

Appendix A

Mathematical derivation of the homogenized model

A.1 Homogenization in the Electrolyte

We set $\psi_\varepsilon(\mathbf{x},t) = \psi(\mathbf{x},\mathbf{y},t,\tau_{\mathrm{r}},\tau_{\mathrm{m}e},\tau_{\mathrm{m}s},\tau_{\mathrm{c}})$ with $\psi = \{c^\ell,\psi^\ell,c^s,\psi^s\}$. Then, combining Eqn. 2.43, 2.44, 2.45, and 2.46 with 2.26 we obtain:

$$
\begin{aligned}
&\frac{\partial c^\ell}{\partial t} + Da_\ell \frac{\partial c^\ell}{\partial \tau_{\mathrm{r}}} + Pe_\ell \Big(\frac{\partial c^\ell}{\partial \tau_{\mathrm{m}e}} + \frac{Da_\ell}{Da_s} \Big(\frac{\partial c^\ell}{\partial \tau_{\mathrm{m}s}} + N_{ohm} \frac{\partial c^\ell}{\partial \tau_c} \Big) \Big) = \\
&\nabla_{\mathbf{x}} \cdot \Big[\Big(\mathbf{D}^\ell - 2t_+(1-t_+) Pe_\ell \mathbf{K}^\ell \frac{1}{c^\ell} \Big) (\nabla_{\mathbf{x}} c^\ell + \varepsilon^{-1} \nabla_{\mathbf{y}} c^\ell) \\
&+ 2t_+ Pe_\ell \mathbf{K}^\ell (\nabla_{\mathbf{x}} \phi^\ell + \varepsilon^{-1} \nabla_{\mathbf{y}} \phi^\ell) \Big] \\
&+ \varepsilon^{-1} \nabla_{\mathbf{y}} \Big[\Big(\mathbf{D}^\ell - 2t_+(1-t_+) Pe_\ell \frac{1}{c^\ell} \Big) \Big(\nabla_{\mathbf{x}} c^\ell + \varepsilon^{-1} \nabla_{\mathbf{y}} c^\ell \Big) \\
&+ 2t_+ Pe_\ell \mathbf{K}^\ell \Big(\nabla_{\mathbf{x}} \phi^\ell + \varepsilon^{-1} \nabla_{\mathbf{y}} \phi^\ell \Big) \Big] = 0
\end{aligned}
\tag{A1a}
$$

subject to:

$$
\begin{aligned}
&\mathbf{n}_\ell \cdot \Big[\Big(\mathbf{D}^\ell - 2t_+(1-t_+) Pe_\ell \mathbf{K}^\ell \frac{1}{c^\ell} \Big) \Big(\nabla_{\mathbf{x}} c^\ell + \varepsilon^{-1} \nabla_{\mathbf{y}} c^\ell \Big) \\
&+ 2t_+ Pe_\ell \mathbf{K}^\ell \Big(\nabla_{\mathbf{x}} \phi^\ell + \varepsilon^{-1} \nabla_{\mathbf{y}} \phi^\ell \Big) \Big] = Da_\ell \sqrt{\frac{c^s_{max}}{c^\ell_{max}}} f(c^\ell_\varepsilon, c^s_\varepsilon, \phi^\ell_\varepsilon, \phi^s_\varepsilon)
\end{aligned}
\tag{A1b}
$$

$$
\begin{aligned}
&\nabla_{\mathbf{x}}\Big[\Big(-2(1-t_+)Pe_\ell\mathbf{K}^\ell\frac{1}{c^\ell}\Big)\Big(\nabla_{\mathbf{x}}c^\ell+\varepsilon^{-1}\nabla_{\mathbf{y}}c^\ell\Big)\\
&+2Pe_\ell\mathbf{K}^\ell\Big(\nabla_{\mathbf{x}}\phi^\ell+\varepsilon^{-1}\nabla_{\mathbf{y}}\phi^\ell\Big)\Big]\\
&+\varepsilon^{-1}\nabla_{\mathbf{y}}\Big[-2(1-t_+)Pe_\ell\mathbf{K}^\ell\frac{1}{c^\ell}\Big(\nabla_{\mathbf{x}}c^\ell+\varepsilon^{-1}\nabla_{\mathbf{y}}c^\ell\Big)\\
&+2Pe_\ell\mathbf{K}^\ell\Big(\nabla_{\mathbf{x}}\phi^\ell+\varepsilon^{-1}\nabla_{\mathbf{y}}\phi^\ell\Big)\Big]=0
\end{aligned}
\tag{A2a}
$$

subject to

$$
\begin{aligned}
&\mathbf{n}_\ell\cdot\Big[-2(1-t_+)Pe_\ell\mathbf{K}^\ell\frac{1}{c^\ell}\Big(\nabla_{\mathbf{x}}c^\ell+\varepsilon^{-1}\nabla_{\mathbf{y}}c^\ell\Big)\\
&+2Pe_\ell\mathbf{K}^\ell\Big(\nabla_{\mathbf{x}}\phi^\ell+\varepsilon^{-1}\nabla_{\mathbf{y}}\phi^\ell\Big)\Big]=Da_\ell\sqrt{\frac{c^s_{max}}{c^\ell_{max}}}f(c^\ell_\varepsilon,c^s_\varepsilon,\phi^\ell_\varepsilon,\phi^s_\varepsilon)
\end{aligned}
\tag{A2b}
$$

respectively, where $f(c^\ell_\varepsilon,c^s_\varepsilon,\phi^\ell_\varepsilon,\phi^s_\varepsilon)$ is defined in Eqn. 2.47.

Asymptotic expansion

Substituting Eqn. 2.27 and Eqn. 2.42 in the previous equations (Eqns. A1 and A2) leads to:

$$
\begin{aligned}
&\varepsilon^{-2}\Big\{\nabla_{\mathbf{y}}\cdot\Big[\Big(-\mathbf{D}^{\ell}+2t_{+}(1-t_{+})\varepsilon^{-\alpha}\mathbf{K}^{\ell}(1/c_0^{\ell})\Big)\nabla_{\mathbf{y}}c_0^{\ell}\\
&\quad-2t_{+}\varepsilon^{-\alpha}\mathbf{K}^{\ell}\nabla_{\mathbf{y}}\phi_0^{\ell}\Big]\Big\}\\
&+\varepsilon^{-1}\Big\{\varepsilon^{1+\beta}\partial_{\tau_{\mathrm{r}}}c_0^{\ell}\\
&\quad+\nabla_{\mathbf{x}}\cdot\Big[\Big(-\mathbf{D}^{\ell}+2t_{+}(1-t_{+})\varepsilon^{-\alpha}\mathbf{K}^{\ell}(1/c_0^{\ell})\Big)\nabla_{\mathbf{y}}c_0^{\ell}\\
&\quad-2t_{+}\varepsilon^{-\alpha}\mathbf{K}^{\ell}\nabla_{\mathbf{y}}\phi_0^{\ell}\Big]\\
&\quad+\nabla_{\mathbf{y}}\cdot\Big[\Big(-\mathbf{D}^{\ell}+2t_{+}(1-t_{+})\varepsilon^{-\alpha}\mathbf{K}^{\ell}(1/c_0^{\ell})\Big)\Big(\nabla_{\mathbf{x}}c_0^{\ell}+\nabla_{\mathbf{y}}c_1^{\ell}\Big)\\
&\quad-2t_{+}(1-t_{+})\varepsilon^{-\alpha}\mathbf{K}^{\ell}(1/c_0^{\ell})(c_1^{\ell}/c_0^{\ell})\nabla_{\mathbf{y}}c_0^{\ell}\\
&\quad-2t_{+}\varepsilon^{-\alpha}\mathbf{K}^{\ell}\Big(\nabla_{\mathbf{x}}\phi_0^{\ell}+\nabla_{\mathbf{y}}\phi_1^{\ell}\Big)\Big]\Big\}\\
&+\varepsilon^{0}\Big\{\partial_t c_0^{\ell}+\varepsilon^{1+\beta}\partial_{\tau_{\mathrm{r}}}c_1^{\ell}+\varepsilon^{-\alpha}\big(\partial_{\tau_{\mathrm{m}e}}c_0^{\ell}+\varepsilon^{\beta-\gamma}(\partial_{\tau_{\mathrm{m}s}}c_0^{\ell}+\varepsilon^{\zeta}\partial_{\tau_{\mathrm{c}}}c_0^{\ell})\big)\\
&\quad+\nabla_{\mathbf{x}}\cdot\Big[\Big(-\mathbf{D}^{\ell}+2t_{+}(1-t_{+})\varepsilon^{-\alpha}\mathbf{K}^{\ell}(1/c_0^{\ell})\Big)\Big(\nabla_{\mathbf{x}}c_0^{\ell}+\nabla_{\mathbf{y}}c_1^{\ell}\Big)\\
&\quad-2t_{+}(1-t_{+})\varepsilon^{-\alpha}\mathbf{K}^{\ell}(1/c_0^{\ell})(c_1^{\ell}/c_0^{\ell})\nabla_{\mathbf{y}}c_0^{\ell}\\
&\quad-2t_{+}\varepsilon^{-\alpha}\mathbf{K}^{\ell}\Big(\nabla_{\mathbf{x}}\phi_0^{\ell}+\nabla_{\mathbf{y}}\phi_1^{\ell}\Big)\Big]\\
&\quad+\nabla_{\mathbf{y}}\cdot\Big[\Big(-\mathbf{D}^{\ell}+2t_{+}(1-t_{+})\varepsilon^{-\alpha}\mathbf{K}^{\ell}(1/c_0^{\ell})\Big)\Big(\nabla_{\mathbf{x}}c_1^{\ell}+\nabla_{\mathbf{y}}c_2^{\ell}\Big)\\
&\quad-2t_{+}(1-t_{+})\varepsilon^{-\alpha}\mathbf{K}^{\ell}(1/c_0^{\ell})(c_1^{\ell}/c_0^{\ell})\Big(\nabla_{\mathbf{x}}c_0^{\ell}+\nabla_{\mathbf{y}}c_1^{\ell}\Big)\\
&\quad+2t_{+}(1-t_{+})\varepsilon^{-\alpha}\mathbf{K}^{\ell}(1/c_0^{\ell})((c_1^{\ell}/c_0^{\ell})^2-(c_2^{\ell}/c_0^{\ell}))\nabla_{\mathbf{y}}c_0^{\ell}\\
&\quad-2t_{+}\varepsilon^{-\alpha}\mathbf{K}^{\ell}\Big(\nabla_{\mathbf{x}}\phi_1^{\ell}+\nabla_{\mathbf{y}}\phi_2^{\ell}\Big)\Big]\Big\}=\mathcal{O}(\varepsilon^{1})
\end{aligned}
\tag{A3a}
$$

subject to:

$$\begin{aligned}
&\varepsilon^{-1}\Big\{\mathbf{n}_\ell\cdot\Big[\Big(\mathbf{D}^\ell-2t_+(1-t_+)\varepsilon^{-\alpha}\mathbf{K}^\ell(1/c_0^\ell)\Big)\nabla_{\mathbf{y}}c_0^\ell\\
&\quad+2t_+\varepsilon^{-\alpha}\mathbf{K}^\ell\nabla_{\mathbf{y}}\phi_0^\ell\Big]\Big\}\\
&+\varepsilon^{0}\Big\{\mathbf{n}_\ell\cdot\Big[\Big(\mathbf{D}^\ell-2t_+(1-t_+)\varepsilon^{-\alpha}\mathbf{K}^\ell(1/c_0^\ell)\Big)\Big(\nabla_{\mathbf{x}}c_0^\ell+\nabla_{\mathbf{y}}c_1^\ell\Big)\\
&\quad+2t_+(1-t_+)\varepsilon^{-\alpha}\mathbf{K}^\ell(1/c_0^\ell)(c_1^\ell/c_0^\ell)\nabla_{\mathbf{y}}c_0^\ell\\
&\quad+2t_+\varepsilon^{-\alpha}\mathbf{K}^\ell\Big(\nabla_{\mathbf{x}}\phi_0^\ell+\nabla_{\mathbf{y}}\phi_1^\ell\Big)\Big]-2\varepsilon^\beta\sqrt{\frac{c_{max}^s}{c_{max}^\ell}}A_0B_0\Big\}\\
&+\varepsilon^{1}\Big\{\mathbf{n}_\ell\cdot\Big[\Big(\mathbf{D}^\ell-2t_+(1-t_+)\varepsilon^{-\alpha}\mathbf{K}^\ell(1/c_0^\ell)\Big)\Big(\nabla_{\mathbf{x}}c_1^\ell+\nabla_{\mathbf{y}}c_2^\ell\Big)\\
&\quad+2t_+(1-t_+)\varepsilon^{-\alpha}\mathbf{K}^\ell(1/c_0^\ell)(c_1^\ell/c_0^\ell)\Big(\nabla_{\mathbf{x}}c_0^\ell+\nabla_{\mathbf{y}}c_1^\ell\Big)\\
&\quad-2t_+(1-t_+)\varepsilon^{-\alpha}\mathbf{K}^\ell(1/c_0^\ell)((c_1^\ell/c_0^\ell)^2-(c_2^\ell/c_0^\ell))\nabla_{\mathbf{y}}c_0^\ell\\
&\quad+2t_+\varepsilon^{-\alpha}\mathbf{K}^\ell\Big(\nabla_{\mathbf{x}}\phi_1^\ell+\nabla_{\mathbf{y}}\phi_2^\ell\Big)\Big]-2\varepsilon^\beta\sqrt{\frac{c_{max}^s}{c_{max}^\ell}}(A_0B_1+A_1B_0)\Big\}=\mathcal{O}(\varepsilon^2)
\end{aligned}\tag{A3b}$$

and

$$
\begin{aligned}
&\varepsilon^{-2}\Big\{\nabla_{\mathbf{y}}\cdot\Big[-2(1-t_+)\varepsilon^{-\alpha}\mathbf{K}^\ell(1/c_0^\ell)\nabla_{\mathbf{y}}c_0^\ell \\
&\qquad +2t_+\varepsilon^{-\alpha}\mathbf{K}^\ell\nabla_{\mathbf{y}}\phi_0^\ell\Big]\Big\} \\
&+\varepsilon^{-1}\Big\{\nabla_{\mathbf{x}}\cdot\Big[-2(1-t_+)\varepsilon^{-\alpha}\mathbf{K}^\ell(1/c_0^\ell)\nabla_{\mathbf{y}}c_0^\ell \\
&\qquad +2\varepsilon^{-\alpha}\mathbf{K}^\ell\nabla_{\mathbf{y}}\phi_0^\ell\Big] \\
&\qquad +\nabla_{\mathbf{y}}\cdot\Big[-2(1-t_+)\varepsilon^{-\alpha}\mathbf{K}^\ell(1/c_0^\ell)\Big(\nabla_{\mathbf{x}}c_0^\ell+\nabla_{\mathbf{y}}c_1^\ell\Big) \\
&\qquad +2(1-t_+)\varepsilon^{-\alpha}\mathbf{K}^\ell(1/c_0^\ell)(c_1^\ell/c_0^\ell)\nabla_{\mathbf{y}}c_0^\ell \\
&\qquad +2\varepsilon^{-\alpha}\mathbf{K}^\ell\Big(\nabla_{\mathbf{x}}\phi_0^\ell+\nabla_{\mathbf{y}}\phi_1^\ell\Big)\Big]\Big\} \\
&+\varepsilon^{0}\Big\{\nabla_{\mathbf{x}}\cdot\Big[-2(1-t_+)\varepsilon^{-\alpha}\mathbf{K}^\ell(1/c_0^\ell)\Big(\nabla_{\mathbf{x}}c_0^\ell+\nabla_{\mathbf{y}}c_1^\ell\Big) \\
&\qquad +2(1-t_+)\varepsilon^{-\alpha}\mathbf{K}^\ell(1/c_0^\ell)(c_1^\ell/c_0^\ell)\nabla_{\mathbf{y}}c_0^\ell \\
&\qquad +2\varepsilon^{-\alpha}\mathbf{K}^\ell\Big(\nabla_{\mathbf{x}}\phi_0^\ell+\nabla_{\mathbf{y}}\phi_1^\ell\Big)\Big] \\
&\qquad +\nabla_{\mathbf{y}}\cdot\Big[-2(1-t_+)\varepsilon^{-\alpha}\mathbf{K}^\ell(1/c_0^\ell)\Big(\nabla_{\mathbf{x}}c_1^\ell+\nabla_{\mathbf{y}}c_2^\ell\Big) \\
&\qquad +2(1-t_+)\varepsilon^{-\alpha}\mathbf{K}^\ell(1/c_0^\ell)(c_1^\ell/c_0^\ell)\Big(\nabla_{\mathbf{x}}c_0^\ell+\nabla_{\mathbf{y}}c_1^\ell\Big) \\
&\qquad -2t_+(1-t_+)\varepsilon^{-\alpha}\mathbf{K}^\ell(1/c_0^\ell)((c_1^\ell/c_0^\ell)^2-(c_2^\ell/c_0^\ell))\nabla_{\mathbf{y}}c_0^\ell \\
&\qquad +2t_+\varepsilon^{-\alpha}\mathbf{K}^\ell\Big(\nabla_{\mathbf{x}}\phi_1^\ell+\nabla_{\mathbf{y}}\phi_2^\ell\Big)\Big]\Big\}=\mathcal{O}(\varepsilon^1)
\end{aligned}
\tag{A4a}
$$

subject to:

$$\begin{aligned}
&\varepsilon^{-1}\Big\{\mathbf{n}_\ell\cdot\Big[-2(1-t_+)\varepsilon^{-\alpha}\mathbf{K}^\ell(1/c_0^\ell)\nabla_{\mathbf{y}}c_0^\ell\\
&\qquad+2\varepsilon^{-\alpha}\mathbf{K}^\ell\nabla_{\mathbf{y}}\phi_0^\ell\Big]\Big\}\\
&+\varepsilon^0\Big\{\mathbf{n}_\ell\cdot\Big[-2(1-t_+)\varepsilon^{-\alpha}\mathbf{K}^\ell(1/c_0^\ell)\Big(\nabla_{\mathbf{x}}c_0^\ell+\nabla_{\mathbf{y}}c_1^\ell\Big)\\
&\qquad+2(1-t_+)\varepsilon^{-\alpha}\mathbf{K}^\ell(1/c_0^\ell)(c_1^\ell/c_0^\ell)\nabla_{\mathbf{y}}c_0^\ell\\
&\qquad+2\varepsilon^{-\alpha}\mathbf{K}^\ell\Big(\nabla_{\mathbf{x}}\phi_0^\ell+\nabla_{\mathbf{y}}\phi_1^\ell\Big)\Big]-2\varepsilon^\beta\sqrt{\frac{c^s_{max}}{c^\ell_{max}}}A_0B_0\Big\}\\
&+\varepsilon^1\Big\{\mathbf{n}_\ell\cdot\Big[-2(1-t_+)\varepsilon^{-\alpha}\mathbf{K}^\ell(1/c_0^\ell)\Big(\nabla_{\mathbf{x}}c_1^\ell+\nabla_{\mathbf{y}}c_2^\ell\Big)\\
&\qquad+2(1-t_+)\varepsilon^{-\alpha}\mathbf{K}^\ell(1/c_0^\ell)(c_1^\ell/c_0^\ell)\Big(\nabla_{\mathbf{x}}c_0^\ell+\nabla_{\mathbf{y}}c_1^\ell\Big)\\
&\qquad-2(1-t_+)\varepsilon^{-\alpha}\mathbf{K}^\ell(1/c_0^\ell)((c_1^\ell/c_0^\ell)^2-(c_2^\ell/c_0^\ell))\nabla_{\mathbf{y}}c_0^\ell\\
&\qquad+2\varepsilon^{-\alpha}\mathbf{K}^\ell\Big(\nabla_{\mathbf{x}}\phi_1^\ell+\nabla_{\mathbf{y}}\phi_2^\ell\Big)\Big]-2\varepsilon^\beta\sqrt{\frac{c^s_{max}}{c^\ell_{max}}}(A_0B_1+A_1B_0)\Big\}=\mathcal{O}(\varepsilon^2)
\end{aligned}\tag{A4b}$$

Where the non-linear terms present in the electronic migration and in the Butler-Volmer are expanded in a McLaurin series as follows:

$$1/c^{\ell} = 1/c_0^{\ell}(1-\varepsilon^1(c_1^{\ell}/c_0^{\ell})+\varepsilon^2((c_1^{\ell}/c_0^{\ell})^2-(c_2^{\ell}/c_0^{\ell}))) + \mathcal{O}(\varepsilon^2)$$

$$\sinh(\phi^s-\phi^{\ell}-U) = \sinh(\phi_0^s-\phi_0^{\ell}-U)+\varepsilon^1(\phi_1^s-\phi_1^{\ell})\cosh(\phi_0^s-\phi_0^{\ell}-U)+\mathcal{O}(\varepsilon^2)$$

$$\sqrt{c_s c^{\ell}(1-c_s)} = \sqrt{c_0^s c_0^{\ell}(1-c_0^s)}(1+\varepsilon^1\frac{c_1^s}{c_0^s})(1+\varepsilon^1\frac{c_1^{\ell}}{c_0^{\ell}})(1-\varepsilon^1\frac{c_1^s}{1-c_0^s})+\mathcal{O}(\varepsilon^1)$$

$$f(c^{\ell},c^s,\phi^{\ell},\phi^s) = \sqrt{c^{\ell}c^s(1-c^s)}\sinh(\phi_s-\phi_l-U) = A_0B_0+\varepsilon^1(A_1B_0+A_0B_1)+\mathcal{O}(\varepsilon^1)$$

$$\begin{aligned}
A_0 &= \sinh(\phi_0^s-\phi_0^{\ell}-U)\\
B_0 &= \sqrt{c_0^s c_0^{\ell}(1-c_0^s)}\\
A_1 &= (\phi_1^s-\phi_1^{\ell})\cosh(\phi_0^s-\phi_0^{\ell}-U)\\
B_1 &= \sqrt{c_0^s c_0^{\ell}(1-c_0^s)}\left(\frac{c_1^s}{2c_0^s}+\frac{c_1^{\ell}}{2c_0^{\ell}}-\frac{c_1^s}{2(1-c_0^s)}\right)
\end{aligned} \tag{A5}$$

Terms of order $\mathcal{O}(\varepsilon^{-2})$

Collecting the leading-order terms in the mass transport equations (Eqn. A3), we obtain:

$$\nabla_{\mathbf{y}}\cdot\left[\left(-\mathbf{D}^{\ell}+2t_+(1-t_+)\varepsilon^{-\alpha}\mathbf{K}^{\ell}(1/c_0^{\ell})\right)\nabla_{\mathbf{y}}c_0^{\ell}-2t_+\varepsilon^{-\alpha}\mathbf{K}^{\ell}\nabla_{\mathbf{y}}\phi_0^{\ell}\right]=0 \tag{A6a}$$

subject to:

$$\mathbf{n}_{\ell}\cdot\left[\left(-\mathbf{D}^{\ell}+2t_+(1-t_+)\varepsilon^{-\alpha}\mathbf{K}^{\ell}(1/c_0^{\ell})\right)\nabla_{\mathbf{y}}c_0^{\ell}-2t_+\varepsilon^{-\alpha}\mathbf{K}^{\ell}\varepsilon^{-1}\nabla_{\mathbf{y}}\phi_0^{\ell}\right]=0 \tag{A6b}$$

Similarly, at the leading order, the charge transport equations (Eqn. A4) are:

$$\nabla_{\mathbf{y}}\cdot\left[-2(1-t_+)\varepsilon^{-\alpha}\mathbf{K}^{\ell}(1/c_0^{\ell})\nabla_{\mathbf{y}}c_0^{\ell}+2\varepsilon^{-\alpha}\mathbf{K}^{\ell}\nabla_{\mathbf{y}}\phi_0^{\ell}\right]=0 \tag{A7a}$$

subject to:

$$\mathbf{n}_\ell \cdot \left[-2(1-t_+)\varepsilon^{-\alpha}\mathbf{K}^\ell(1/c_0^\ell)\nabla_\mathbf{y} c_0^\ell + 2\varepsilon^{-\alpha}\mathbf{K}^\ell\varepsilon^{-1}\nabla_\mathbf{y}\phi_0^\ell\right] = 0 \tag{A7b}$$

Homogeneity of Eqns. A6 and A7 guarantees that c_0^ℓ and ϕ_0^ℓ are independent of y:

$$\begin{aligned} c_0^\ell &= c_0^\ell(\mathbf{x}, t, \tau_\mathrm{r}, \tau_{\mathrm{m}e}, \tau_{\mathrm{m}s}, \tau_\mathrm{c}) \\ \phi_0^\ell &= \phi_0^\ell(\mathbf{x}, t, \tau_\mathrm{r}, \tau_{\mathrm{m}e}, \tau_{\mathrm{m}s}, \tau_\mathrm{c}) \end{aligned} \tag{A8}$$

Terms of order $\mathcal{O}(\varepsilon^{-1})$

Since $\nabla_\mathbf{y} c_0^\ell = \mathbf{0}$ and $\nabla_\mathbf{y}\phi_0^\ell = \mathbf{0}$, the mass balance equations (Eqns. A1) at order $\mathcal{O}(\varepsilon^{-1})$ simplifies to:

$$\nabla_\mathbf{y} \cdot \left[\left(-\mathbf{D}^\ell + 2t_+(1-t_+)\varepsilon^{-\alpha}\mathbf{K}^\ell(1/c_0^\ell)\right)\left(\nabla_\mathbf{x} c_0^\ell + \nabla_\mathbf{y} c_1^\ell\right) - 2t_+\varepsilon^{-\alpha}\mathbf{K}^\ell\left(\nabla_\mathbf{x}\phi_0^\ell + \nabla_\mathbf{y}\phi_1^\ell\right)\right] = -\varepsilon^{1+\beta}\partial_r c_0^\ell \tag{A9a}$$

subject to:

$$\mathbf{n}_\ell \cdot \left[\left(-\mathbf{D}^\ell + 2t_+(1-t_+)\varepsilon^{-\alpha}\mathbf{K}^\ell(1/c_0^\ell)\right)\left(\nabla_\mathbf{x} c_0^\ell + \nabla_\mathbf{y} c_1^\ell\right) - 2t_+\varepsilon^{-\alpha}\mathbf{K}^\ell\left(\nabla_\mathbf{x}\phi_0^\ell + \nabla_\mathbf{y}\phi_1^\ell\right)\right] = -2\varepsilon^\beta\sqrt{\frac{c_{max}^s}{c_{max}^\ell}}A_0 B_0 \tag{A9b}$$

By integrating Eqn. A9a over $\mathcal{L}$ with respect to $\mathbf{y}$ and Eqn. A9b over Γ with respect to $\mathbf{y}$, following the definition in 2.28 and while accounting for the periodicity of the coefficients on the external boundary of the unit cell $\partial\mathrm{Y}$, we obtain:

$$\varepsilon^{1+\beta}\partial_r c_0^\ell = 2\mathcal{K}^\star\varepsilon^\beta\sqrt{\frac{c_{max}^s}{c_{max}^\ell}}A_0 B_0 \tag{A10}$$

where $\mathcal{K}^{\star}$ is defined in Eqn. 2.65. Combining A9a with A10 to eliminate the temporal derivative, we obtain:

$$\nabla_{\mathbf{y}} \cdot \left[\left(-\mathbf{D}^{\ell} + 2t_{+}(1-t_{+})\varepsilon^{-\alpha}\mathbf{K}^{\ell}(1/c_0^{\ell}) \right) \left(\nabla_{\mathbf{x}} c_0^{\ell} + \nabla_{\mathbf{y}} c_1^{\ell} \right) - 2t_{+}\varepsilon^{-\alpha}\mathbf{K}^{\ell} \left(\nabla_{\mathbf{x}} \phi_0^{\ell} + \nabla_{\mathbf{y}} \phi_1^{\ell} \right) \right]$$
$$+ 2\mathcal{K}^{\star}\varepsilon^{\beta} \sqrt{\frac{c_{max}^{s}}{c_{max}^{\ell}}} A_0 B_0 = 0 \tag{A11a}$$

subject to:

$$\mathbf{n}_{\ell} \cdot \left[\left(-\mathbf{D}^{\ell} + 2t_{+}(1-t_{+})\varepsilon^{-\alpha}\mathbf{K}^{\ell}(1/c_0^{\ell}) \right) \left(\nabla_{\mathbf{x}} c_0^{\ell} + \nabla_{\mathbf{y}} c_1^{\ell} \right) - 2t_{+}\varepsilon^{-\alpha}\mathbf{K}^{\ell} \left(\nabla_{\mathbf{x}} \phi_0^{\ell} + \nabla_{\mathbf{y}} \phi_1^{\ell} \right) \right]$$
$$+ 2\varepsilon^{\beta} \sqrt{\frac{c_{max}^{s}}{c_{max}^{\ell}}} A_0 B_0 = 0 \tag{A11b}$$

Similarly, at the leading order, the charge transport equations (Eqns. A2) are:

$$\nabla_{\mathbf{y}} \cdot \left[-2(1-t_{+})\varepsilon^{-\alpha}\mathbf{K}^{\ell}(1/c_0^{\ell}) \left(\nabla_{\mathbf{x}} c_0^{\ell} + \nabla_{\mathbf{y}} c_1^{\ell} \right) + 2\varepsilon^{-\alpha}\mathbf{K}^{\ell} \left(\nabla_{\mathbf{x}} \phi_0^{\ell} + \nabla_{\mathbf{y}} \phi_1^{\ell} \right) \right] = 0 \tag{A12a}$$

subject to:

$$\mathbf{n}_{\ell} \cdot \left[-2(1-t_{+})\varepsilon^{-\alpha}\mathbf{K}^{\ell}(1/c_0^{\ell}) \left(\nabla_{\mathbf{x}} c_0^{\ell} + \nabla_{\mathbf{y}} c_1^{\ell} \right) + 2\varepsilon^{-\alpha}\mathbf{K}^{\ell} \left(\nabla_{\mathbf{x}} \phi_0^{\ell} + \nabla_{\mathbf{y}} \phi_1^{\ell} \right) \right] = 2\varepsilon^{\beta} \sqrt{\frac{c_{max}^{s}}{c_{max}^{\ell}}} A_0 B_0 \tag{A12b}$$

Eqns. A11 and A12 form boundary value problems for both c_1^{ℓ} and ϕ_1^{ℓ}. Following Ref. [45], we look for solutions in the form:

$$\begin{aligned} c_1^{\ell}(x,y,t,\tau_{\mathrm{r}},\tau_{\mathrm{me}},\tau_{\mathrm{m}s},\tau_{\mathrm{c}}) &= \chi_1(y)\nabla_{\mathbf{x}} c_0^{\ell}(x,t,\tau_{\mathrm{r}},\tau_{\mathrm{m}e},\tau_{\mathrm{m}s},\tau_{\mathrm{c}}) + \bar{c}_1^{\ell}(x,t,\tau_{\mathrm{r}},\tau_{\mathrm{m}e},\tau_{\mathrm{m}s},\tau_{\mathrm{c}}) \\ \phi_1^{\ell}(x,y,t,\tau_{\mathrm{r}},\tau_{\mathrm{me}},\tau_{\mathrm{m}s},\tau_{\mathrm{c}}) &= \chi_2(y)\nabla_{\mathbf{x}} \phi_0^{\ell}(x,t,\tau_{\mathrm{r}},\tau_{\mathrm{m}e},\tau_{\mathrm{m}s},\tau_{\mathrm{c}}) + \bar{\phi}_1^{\ell}(x,t,\tau_{\mathrm{r}},\tau_{\mathrm{m}e},\tau_{\mathrm{m}s},\tau_{\mathrm{c}}) \end{aligned} \tag{A13}$$

Substituting A13 into A11 and A12 we obtain:

$$\nabla_{\mathbf{y}} \cdot \left[\left(-\mathbf{D}^\ell + 2t_+(1-t_+)\varepsilon^{-\alpha}\mathbf{K}^\ell(1/c_0^\ell)\right)\left(I+\nabla_{\mathbf{y}}\chi_1\right)\nabla_{\mathbf{x}} c_0^\ell - 2t_+\varepsilon^{-\alpha}\mathbf{K}^\ell\left(I+\nabla_{\mathbf{y}}\chi_2\right)\nabla_{\mathbf{x}}\phi_0^\ell\right]$$
$$+ 2\mathcal{K}^\star \varepsilon^\beta \sqrt{\frac{c^s_{max}}{c^\ell_{max}}} A_0 B_0 = 0 \tag{A14a}$$

subject to:

$$\mathbf{n}_\ell \cdot \left[\left(-\mathbf{D}^\ell + 2t_+(1-t_+)\varepsilon^{-\alpha}\mathbf{K}^\ell(1/c_0^\ell)\right)\left(I+\nabla_{\mathbf{y}}\chi_1\right)\nabla_{\mathbf{x}} c_0^\ell - 2t_+\varepsilon^{-\alpha}\mathbf{K}^\ell\left(I+\nabla_{\mathbf{y}}\chi_2\right)\nabla_{\mathbf{x}}\phi_0^\ell\right]$$
$$+ 2\varepsilon^\beta \sqrt{\frac{c^s_{max}}{c^\ell_{max}}} A_0 B_0 = 0 \tag{A14b}$$

and

$$\nabla_{\mathbf{y}} \cdot \left[-2(1-t_+)\varepsilon^{-\alpha}\mathbf{K}^\ell(1/c_0^\ell)\left(I+\nabla_{\mathbf{y}}\chi_1\right)\nabla_{\mathbf{x}} c_0^\ell + 2\varepsilon^{-\alpha}\mathbf{K}^\ell\left(I+\nabla_{\mathbf{y}}\chi_2\right)\nabla_{\mathbf{x}}\phi_0^\ell\right] = 0 \tag{A15a}$$

subject to:

$$\mathbf{n}_\ell \cdot \left[-2(1-t_+)\varepsilon^{-\alpha}\mathbf{K}^\ell(1/c_0^\ell)\left(I+\nabla_{\mathbf{y}}\chi_1\right)\nabla_{\mathbf{x}} c_0^\ell + 2\varepsilon^{-\alpha}\mathbf{K}^\ell\left(I+\nabla_{\mathbf{y}}\chi_2\right)\nabla_{\mathbf{x}}\phi_0^\ell\right]$$
$$- 2\varepsilon^\beta \sqrt{\frac{c^s_{max}}{c^\ell_{max}}} A_0 B_0 = 0 \tag{A15b}$$

Eqns. A14 and A15 define the closure variables $\chi_1(y)$ and $\chi_2(y)$. The coupling of $\chi_1(y)$ and $\chi_2(y)$ with $c_0^\ell(x)$, $\phi_0^\ell(x)$, $A_0(x)$ and $B_0(x)$ through the boundary value problems A11 and A12 is incompatible with the closure variables' general representation postulated in A13. This inconsistency is resolved by imposing the following constraints on the exponents α and β. If we choose $\beta > \max 0, -\alpha$ and $\alpha < 0$, then the terms that contains $\varepsilon^{-\alpha}$ or ε^{β} are negligible. Considering also that the conductivity tensor $\mathbf{K}^\ell$ and the diffusion tensor $\mathbf{D}^\ell$ are function of concentration c^ℓ and potential ϕ^ℓ, with an order ε^1 approximation we have that $\mathbf{K}^\ell \approx \mathbf{K}^\ell(c_0^\ell, \phi_0^\ell)$ and $\mathbf{D}^\ell \approx \mathbf{K}^\ell(c_0^\ell, \phi_0^\ell)$. As a result, $\chi_1(y) = \chi_2(y) = \chi_\ell(y)$. The closure variable $\chi_\ell(y)$

defines the cell problem and describes the behavior of the effective diffusion and conductivity tensors due to the morphology of the system. Under these hypothesis, Eqns. A14 and A15 simplifies to:

$$\nabla_{\mathbf{y}} \cdot \left[\left(I + \nabla_{\mathbf{y}} \chi_1 \right) \right] = 0 \tag{A16a}$$

subject to:

$$\mathbf{n}_\ell \cdot \left[\left(I + \nabla_{\mathbf{y}} \chi_1 \right) \right] = 0 \tag{A16b}$$

Terms of order $\mathcal{O}(\varepsilon^0)$

Collecting the zeroth-order term in the mass balance equation (Eqns A1a) and first-order term in the corresponding boundary condition (Eqns A1b), and recalling the results obtained in the previous steps, we have:

$$\begin{aligned}
&\partial_t c_0^\ell + \varepsilon^{1+\beta} \partial_{\tau_\mathrm{r}} c_1^\ell + \varepsilon^{-\alpha} \left(\partial_{\tau_{\mathrm{m}e}} c_0^\ell + \varepsilon^{\beta-\gamma} (\partial_{\tau_{\mathrm{m}s}} c_0^\ell + \varepsilon^\zeta \partial_{\tau_\mathrm{c}} c_0^\ell) \right) \\
&+ \nabla_{\mathbf{x}} \cdot \Big[\left(-\mathbf{D}^\ell + 2t_+ (1 - t_+) \varepsilon^{-\alpha} \mathbf{K}^\ell (1/c_0^\ell) \right) \left(\nabla_{\mathbf{x}} c_0^\ell + \nabla_{\mathbf{y}} c_1^\ell \right) \\
&- 2t_+ \varepsilon^{-\alpha} \mathbf{K}^\ell \left(\nabla_{\mathbf{x}} \phi_0^\ell + \nabla_{\mathbf{y}} \phi_1^\ell \right) \Big] \\
&+ \nabla_{\mathbf{y}} \cdot \Big[\left(-\mathbf{D}^\ell + 2t_+ (1 - t_+) \varepsilon^{-\alpha} \mathbf{K}^\ell (1/c_0^\ell) \right) \left(\nabla_{\mathbf{x}} c_1^\ell + \nabla_{\mathbf{y}} c_2^\ell \right) \\
&- 2t_+ (1 - t_+) \varepsilon^{-\alpha} \mathbf{K}^\ell (1/c_0^\ell)(c_1^\ell / c_0^\ell) \left(\nabla_{\mathbf{x}} c_0^\ell + \nabla_{\mathbf{y}} c_1^\ell \right) \\
&- 2t_+ \varepsilon^{-\alpha} \mathbf{K}^\ell \left(\nabla_{\mathbf{x}} \phi_1^\ell + \nabla_{\mathbf{y}} \phi_2^\ell \right) \Big] = 0
\end{aligned} \tag{A17a}$$

subject to:

$$\begin{aligned}
&\mathbf{n}_\ell \cdot \Big[\left(-\mathbf{D}^\ell + 2t_+ (1 - t_+) \varepsilon^{-\alpha} \mathbf{K}^\ell (1/c_0^\ell) \right) \left(\nabla_{\mathbf{x}} c_1^\ell + \nabla_{\mathbf{y}} c_2^\ell \right) \\
&- 2t_+ (1 - t_+) \varepsilon^{-\alpha} \mathbf{K}^\ell (1/c_0^\ell)(c_1^\ell / c_0^\ell) \left(\nabla_{\mathbf{x}} c_0^\ell + \nabla_{\mathbf{y}} c_1^\ell \right) \\
&- 2t_+ \varepsilon^{-\alpha} \mathbf{K}^\ell \left(\nabla_{\mathbf{x}} \phi_1^\ell + \nabla_{\mathbf{y}} \phi_2^\ell \right) \Big] + 2\varepsilon^\beta \sqrt{\frac{c_{max}^s}{c_{max}^\ell}} (A_0 B_1 + A_1 B_0) = 0
\end{aligned} \tag{A17b}$$

integrating Eqn. A17a over $\mathcal{L}$ with respect to $\mathbf{y}$ and Eqn.A17b over Γ with respect to $\mathbf{y}$, following the definition in 2.28 and, taking into account the periodic boundary condition:

$$\begin{aligned}
&\partial_t \langle c_0^\ell \rangle_\mathcal{L} + \varepsilon^{1+\beta} \partial_r \langle c_1^\ell \rangle_\mathcal{L} + \varepsilon^{-\alpha} \big(\partial_{m,l} \langle c_0^\ell \rangle_\mathcal{L} + \varepsilon^{\beta-\gamma} (\partial_{m,s} \langle c_0^\ell \rangle_\mathcal{L} + \varepsilon^{\zeta} \partial_c \langle c_0^\ell \rangle_\mathcal{L}) \big) \\
&+ \eta^{-1} \nabla_\mathbf{x} \cdot \Big[\Big(-\mathbf{D}^{\ell\star\star} + 2t_+ (1 - t_+) \varepsilon^{-\alpha} \mathbf{K}^{\ell\star\star} (1/\langle c_0^\ell \rangle_\mathcal{L}) \Big) \nabla_\mathbf{x} \langle c_0^\ell \rangle_\mathcal{L} \\
&- 2t_+ \varepsilon^{-\alpha} \mathbf{K}^{\ell\star\star} \nabla_\mathbf{x} \langle \phi_0^\ell \rangle_\mathcal{L} \Big] \\
&- 2\varepsilon^\beta \sqrt{\frac{c^s_{max}}{c^\ell_{max}}} \mathcal{K}^\star \big(\langle A_0 \rangle_\mathcal{L} \langle B_1 \rangle_\Gamma + \langle A_1 \rangle_\Gamma \langle B_0 \rangle_\mathcal{L} \big) = 0
\end{aligned} \tag{A18}$$

Now we recall that:

$$\langle c^\ell \rangle_\mathcal{L} = \langle c_0^\ell \rangle_\mathcal{L} + \varepsilon \langle c_1^\ell \rangle_\mathcal{L} + \mathcal{O}(\varepsilon^2) \tag{A19a}$$

$$\langle \phi^\ell \rangle_\mathcal{L} = \langle \phi_0^\ell \rangle_\mathcal{L} + \varepsilon \langle \phi_1^\ell \rangle_\mathcal{L} + \mathcal{O}(\varepsilon^2) \tag{A19b}$$

$$\varepsilon^{1+\beta} \partial_r c_0^\ell = 2\mathcal{K}^\star \varepsilon^\beta \sqrt{\frac{c^s_{max}}{c^\ell_{max}}} A_0 B_0 \tag{A19c}$$

Multiplying the temporal derivative of Eqn. A19a by ε, we obtain:

$$\begin{aligned}
&\varepsilon \partial_t \langle c^\ell \rangle_\mathcal{L} = \\
&\varepsilon \partial_t \langle c_0^\ell \rangle_\mathcal{L} + \varepsilon^{1+\beta} \partial_r \langle c_0^\ell \rangle_\mathcal{L} + \varepsilon^{1-\alpha} \big(\partial_{m,l} \langle c_0^\ell \rangle_\mathcal{L} + \varepsilon^{\beta-\gamma} (\partial_{m,s} \langle c_0^\ell \rangle_\mathcal{L} + \varepsilon^{\zeta} \partial_c \langle c_0^\ell \rangle_\mathcal{L}) \big) + \mathcal{O}(\varepsilon^2)
\end{aligned} \tag{A20}$$

Then, integrating Eqn. A19c over $\mathcal{L}$ with respect to $\mathbf{y}$ and adding to Eqn. A20 we obtain:

$$\begin{aligned}
&\varepsilon \partial_t \langle c^\ell \rangle_\mathcal{L} - 2\mathcal{K}^\star \varepsilon^\beta \sqrt{\frac{c^s_{max}}{c^\ell_{max}}} \langle A_0 \rangle_\mathcal{L} \langle B_0 \rangle_\mathcal{L} = \\
&\varepsilon \partial_t \langle c_0^\ell \rangle_\mathcal{L} + \varepsilon^{1-\alpha} \big(\partial_{m,l} \langle c_0^\ell \rangle_\mathcal{L} + \varepsilon^{\beta-\gamma} (\partial_{m,s} \langle c_0^\ell \rangle_\mathcal{L} + \varepsilon^{\zeta} \partial_c \langle c_0^\ell \rangle_\mathcal{L}) \big) + \mathcal{O}(\varepsilon^2)
\end{aligned} \tag{A21}$$

Multiplying A18 by ε:

$$
\begin{aligned}
&\varepsilon\partial_t\langle c_0^\ell\rangle_{\mathcal{L}} + \varepsilon^{1-\alpha}\big(\partial_{m,l}\langle c_0^\ell\rangle_{\mathcal{L}} + \varepsilon^{\beta-\gamma}(\partial_{m,s}\langle c_0^\ell\rangle_{\mathcal{L}} + \varepsilon^{\zeta}\partial_c\langle c_0^\ell\rangle_{\mathcal{L}})\big)\\
&= -\eta^{-1}\nabla_{\mathbf{x}}\cdot\Big[\Big(-\mathbf{D}^{\ell\star\star} + 2t_+(1-t_+)\varepsilon^{-\alpha}\mathbf{K}^{\ell\star\star}(1/\langle c_0^\ell\rangle_{\mathcal{L}})\Big)\nabla_{\mathbf{x}}\langle c_0^\ell\rangle_{\mathcal{L}} - 2t_+\varepsilon^{-\alpha}\mathbf{K}^{\ell\star\star}\nabla_{\mathbf{x}}\langle\phi_0^\ell\rangle_{\mathcal{L}}\Big]\\
&+ 2\varepsilon^{1+\beta}\sqrt{\frac{c^s_{max}}{c^\ell_{max}}}\mathcal{K}^\star\big(\langle A_0\rangle_{\mathcal{L}}\langle B_1\rangle_\Gamma + \langle A_1\rangle_\Gamma\langle B_0\rangle_{\mathcal{L}}\big) + \mathcal{O}(\varepsilon^2)
\end{aligned}
\tag{A22}
$$

Combining Eqn. A21 and A22, we obtain:

$$
\begin{aligned}
&\varepsilon\partial_t\langle c^\ell\rangle_{\mathcal{L}} =\\
&-\varepsilon\eta^{-1}\nabla_{\mathbf{x}}\cdot\Big[\Big(-\mathbf{D}^{\ell\star\star} + 2t_+(1-t_+)\varepsilon^{-\alpha}\mathbf{K}^{\ell\star\star}(1/\langle c_0^\ell\rangle_{\mathcal{L}})\Big)\nabla_{\mathbf{x}}\langle c_0^\ell\rangle_{\mathcal{L}} - 2t_+\varepsilon^{-\alpha}\mathbf{K}^{\ell\star\star}\nabla_{\mathbf{x}}\langle\phi_0^\ell\rangle_{\mathcal{L}}\Big]\\
&+ 2\varepsilon^{\beta}\sqrt{\frac{c^s_{max}}{c^\ell_{max}}}\mathcal{K}^\star\Big[\langle A_0\rangle_{\mathcal{L}}\langle B_0\rangle_{\mathcal{L}} + \varepsilon\big(\langle A_0\rangle_{\mathcal{L}}\langle B_1\rangle_\Gamma + \langle A_1\rangle_\Gamma\langle B_0\rangle_{\mathcal{L}}\big)\Big] + \mathcal{O}(\varepsilon^2)
\end{aligned}
\tag{A23}
$$

Combining the result of Eqn. A23 with the expansions:

$$
\begin{aligned}
\varepsilon\langle c^\ell\rangle_{\mathcal{L}} &= \varepsilon\langle c_0^\ell\rangle_{\mathcal{L}} + \mathcal{O}(\varepsilon^2) = \varepsilon c_0^\ell + \mathcal{O}(\varepsilon^2)\\
\varepsilon\langle \phi^\ell\rangle_{\mathcal{L}} &= \varepsilon\langle \phi_0^\ell\rangle_{\mathcal{L}} + \mathcal{O}(\varepsilon^2) = \varepsilon \phi_0^\ell + \mathcal{O}(\varepsilon^2)
\end{aligned}
\tag{A24}
$$

and recalling the definitions of $Da_\ell = \varepsilon^\beta$ and $Pe_\ell = \varepsilon^{-\alpha}$ and assuming $\langle\psi_\ell\rangle_\Gamma = \langle\psi_\ell\rangle_{\mathcal{L}}$ and $\langle\psi_s\rangle_\Gamma = \langle\psi_s\rangle_s$, where $\psi = \{c,\phi\}$, leads to the homogenized equation of the mass transport within the liquid phase:

$$
\begin{aligned}
&\eta\partial_t\langle c^\ell\rangle_{\mathcal{L}} = \nabla_{\mathbf{x}}\cdot\Big[\big(\mathbf{D}^{\ell\star\star} - 2t_+(1-t_+)Pe_\ell\mathbf{K}^{\ell\star\star}(1/\langle c^\ell\rangle_{\mathcal{L}})\big)\nabla_{\mathbf{x}}\langle c^\ell\rangle_{\mathcal{L}} + 2t_+Pe_\ell\mathbf{K}^{\ell\star\star}\nabla_{\mathbf{x}}\langle\phi^\ell\rangle_{\mathcal{L}}\Big]\\
&+ 2\eta\varepsilon^{-1}\mathcal{K}^\star Da_\ell\sqrt{\frac{c^s_{max}}{c^\ell_{max}}}f(\langle c^\ell\rangle_{\mathcal{L}}, \langle c^s\rangle_{\mathcal{S}}, \langle\phi^\ell\rangle_{\mathcal{L}}, \langle\phi^s\rangle_{\mathcal{S}})
\end{aligned}
\tag{A25}
$$

where:

$$
f(\langle c^\ell\rangle_{\mathcal{L}}, \langle c^s\rangle_{\mathcal{S}}, \langle\phi^\ell\rangle_{\mathcal{L}}, \langle\phi^s\rangle_{\mathcal{S}}) \approx \langle A_0\rangle_{\mathcal{L}}\langle B_0\rangle_{\mathcal{L}} + \varepsilon(\langle A_0\rangle_{\mathcal{L}}\langle B_1\rangle_\Gamma + \langle A_1\rangle_\Gamma\langle B_0\rangle_{\mathcal{L}}) + \mathcal{O}(\varepsilon^2)
\tag{A26}
$$

Similarly, collecting the zeroth-order term in the charge balance equation (Eqns A2a) and first-order term in the corresponding boundary condition (Eqns A2b):

$$\begin{aligned}
&\nabla_{\mathbf{x}} \cdot \Big[-2(1-t_+)\varepsilon^{-\alpha}\mathbf{K}^\ell(1/c_0^\ell)\Big(\nabla_{\mathbf{x}} c_0^\ell + \nabla_{\mathbf{y}} c_1^\ell\Big) \\
&+ 2\varepsilon^{-\alpha}\mathbf{K}^\ell\Big(\nabla_{\mathbf{x}}\phi_0^\ell + \nabla_{\mathbf{y}}\phi_1^\ell\Big)\Big] \\
&+ \nabla_{\mathbf{y}} \cdot \Big[-2(1-t_+)\varepsilon^{-\alpha}\mathbf{K}^\ell(1/c_0^\ell)\Big(\nabla_{\mathbf{x}} c_1^\ell + \nabla_{\mathbf{y}} c_2^\ell\Big) \\
&+ 2(1-t_+)\varepsilon^{-\alpha}\mathbf{K}^\ell(1/c_0^\ell)(c_1^\ell/c_0^\ell)\Big(\nabla_{\mathbf{x}} c_0^\ell + \nabla_{\mathbf{y}} c_1^\ell\Big) \\
&+ 2t_+\varepsilon^{-\alpha}\mathbf{K}^\ell\Big(\nabla_{\mathbf{x}}\phi_1^\ell + \nabla_{\mathbf{y}}\phi_2^\ell\Big)\Big] = 0
\end{aligned} \tag{A27a}$$

subject to:

$$\begin{aligned}
&\mathbf{n}_\ell \cdot \Big[-2(1-t_+)\varepsilon^{-\alpha}\mathbf{K}^\ell(1/c_0^\ell)\Big(\nabla_{\mathbf{x}} c_1^\ell + \nabla_{\mathbf{y}} c_2^\ell\Big) \\
&+ 2(1-t_+)\varepsilon^{-\alpha}\mathbf{K}^\ell(1/c_0^\ell)(c_1^\ell/c_0^\ell)\Big(\nabla_{\mathbf{x}} c_0^\ell + \nabla_{\mathbf{y}} c_1^\ell\Big) \\
&+ 2\varepsilon^{-\alpha}\mathbf{K}^\ell\Big(\nabla_{\mathbf{x}}\phi_1^\ell + \nabla_{\mathbf{y}}\phi_2^\ell\Big)\Big] - 2\varepsilon^{\beta}\sqrt{\frac{c_{max}^s}{c_{max}^\ell}}(A_0B_1 + A_1B_0) = 0
\end{aligned} \tag{A27b}$$

By multiplying Eqns. A27 by ε and adding them to Eqns. A15:

$$\begin{aligned}
&\varepsilon\nabla_{\mathbf{x}} \cdot \Big[-2(1-t_+)\varepsilon^{-\alpha}\mathbf{K}^\ell(1/c_0^\ell)\Big(\nabla_{\mathbf{x}} c_0^\ell + \nabla_{\mathbf{y}} c_1^\ell\Big) \\
&+ 2\varepsilon^{-\alpha}\mathbf{K}^\ell\Big(\nabla_{\mathbf{x}}\phi_0^\ell + \nabla_{\mathbf{y}}\phi_1^\ell\Big)\Big] \\
&+ \varepsilon\nabla_{\mathbf{y}} \cdot \Big[-2(1-t_+)\varepsilon^{-\alpha}\mathbf{K}^\ell(1/c_0^\ell)\Big(\nabla_{\mathbf{x}} c_1^\ell + \nabla_{\mathbf{y}} c_2^\ell\Big) \\
&+ 2(1-t_+)\varepsilon^{-\alpha}\mathbf{K}^\ell(1/c_0^\ell)(c_1^\ell/c_0^\ell)\Big(\nabla_{\mathbf{x}} c_0^\ell + \nabla_{\mathbf{y}} c_1^\ell\Big) \\
&+ 2t_+\varepsilon^{-\alpha}\mathbf{K}^\ell\Big(\nabla_{\mathbf{x}}\phi_1^\ell + \nabla_{\mathbf{y}}\phi_2^\ell\Big)\Big] \\
&+ \nabla_{\mathbf{y}} \cdot \Big[-2(1-t_+)\varepsilon^{-\alpha}\mathbf{K}^\ell(1/c_0^\ell)\Big(I + \nabla_{\mathbf{y}}\chi_1\Big)\nabla_{\mathbf{x}} c_0^\ell \\
&+ 2\varepsilon^{-\alpha}\mathbf{K}^\ell\Big(I + \nabla_{\mathbf{y}}\chi_2\Big)\nabla_{\mathbf{x}}\phi_0^\ell\Big] = 0
\end{aligned} \tag{A28a}$$

subject to:

$$\begin{aligned}
&\varepsilon \mathbf{n}_\ell \cdot \Big[-2(1-t_+)\varepsilon^{-\alpha}\mathbf{K}^\ell(1/c_0^\ell)\Big(\nabla_\mathbf{x} c_1^\ell + \nabla_\mathbf{y} c_2^\ell\Big)\\
&+2(1-t_+)\varepsilon^{-\alpha}\mathbf{K}^\ell(1/c_0^\ell)(c_1^\ell/c_0^\ell)\Big(\nabla_\mathbf{x} c_0^\ell+\nabla_\mathbf{y} c_1^\ell\Big)\\
&+2\varepsilon^{-\alpha}\mathbf{K}^\ell\Big(\nabla_\mathbf{x}\phi_1^\ell+\nabla_\mathbf{y}\phi_2^\ell\Big)\Big]\\
&+\mathbf{n}_\ell\cdot\Big[-2(1-t_+)\varepsilon^{-\alpha}\mathbf{K}^\ell(1/c_0^\ell)\Big(I+\nabla_\mathbf{y}\chi_1\Big)\nabla_\mathbf{x}c_0^\ell\\
&+2\varepsilon^{-\alpha}\mathbf{K}^\ell\Big(I+\nabla_\mathbf{y}\chi_2\Big)\nabla_\mathbf{x}\phi_0^\ell\Big]\\
&=2\varepsilon^\beta\sqrt{\frac{c^s_{max}}{c^\ell_{max}}}\big(A_0B_0+\varepsilon\big(A_0B_1+A_1B_0\big)\big)
\end{aligned}\tag{A28b}$$

By integrating Eqn. A28a over $\mathcal{L}$ with respect to $\mathbf{y}$ and Eqn. A28b over Γ with respect to $\mathbf{y}$, following the definition in 2.28 and, taking into account the periodic boundary condition:

$$\begin{aligned}
&\varepsilon\eta^{-1}\nabla_\mathbf{x}\cdot\Big[\big(-2(1-t_+)\varepsilon^{-\alpha}\mathbf{K}^{\ell\star\star}(1/\langle c_0^\ell\rangle_\mathcal{L})\big)\nabla_\mathbf{x}\langle c_0^\ell\rangle_\mathcal{L}+2\varepsilon^{-\alpha}\mathbf{K}^{\ell\star\star}\nabla_\mathbf{x}\langle\phi_0^\ell\rangle_\mathcal{L}\Big]\\
&=-2\varepsilon^\beta\sqrt{\frac{c^s_{max}}{c^\ell_{max}}}\mathcal{K}^\star[\langle A_0\rangle_\mathcal{L}\langle B_0\rangle_\mathcal{L}+\varepsilon(\langle A_0\rangle_\mathcal{L}\langle B_1\rangle_\Gamma+\langle A_1\rangle_\Gamma\langle B_0\rangle_\mathcal{L})]
\end{aligned}\tag{A29}$$

Combining the result of Eqn. A29 with the expansions:

$$\begin{aligned}
\varepsilon\langle c^\ell\rangle_\mathcal{L}&=\varepsilon\langle c_0^\ell\rangle_\mathcal{L}+\mathcal{O}(\varepsilon^2)=\varepsilon c_0^\ell+\mathcal{O}(\varepsilon^2)\\
\varepsilon\langle \phi^\ell\rangle_\mathcal{L}&=\varepsilon\langle \phi_0^\ell\rangle_\mathcal{L}+\mathcal{O}(\varepsilon^2)=\varepsilon \phi_0^\ell+\mathcal{O}(\varepsilon^2)
\end{aligned}\tag{A30}$$

and recalling the definitions of $Da_\ell=\varepsilon^\beta$ and $Pe_\ell=\varepsilon^{-\alpha}$ and assuming $\langle\psi_s\rangle_\Gamma=\langle\psi_s\rangle_s$ and $\langle\psi_\ell\rangle_\Gamma=\langle\psi_\ell\rangle_\mathcal{L}$, where $\psi=\{c,\phi\}$, leads to the homogenized equation of the charge transport within the liquid phase::

$$\begin{aligned}
&\nabla_\mathbf{x}\cdot\Big[\big(-2(1-t_+)Pe_\ell\mathbf{K}^{\ell\star\star}(1/\langle c^\ell\rangle_\mathcal{L})\big)\nabla_\mathbf{x}\langle c^\ell\rangle_\mathcal{L}+2Pe_\ell\mathbf{K}^{\ell\star\star}\nabla_\mathbf{x}\langle\phi^\ell\rangle_\mathcal{L}\Big]\\
&=-2\eta\varepsilon^{-1}\mathcal{K}^\star Da_\ell\sqrt{\frac{c^s_{max}}{c^\ell_{max}}}f(\langle c^\ell\rangle_\mathcal{L},\langle c^s\rangle_\mathcal{S},\langle\phi^\ell\rangle_\mathcal{L},\langle\phi^s\rangle_\mathcal{S})
\end{aligned}\tag{A31}$$

where:

$$f(\langle c^\ell\rangle_{\mathcal{L}}, \langle c^s\rangle_{\mathcal{S}}, \langle\phi^\ell\rangle_{\mathcal{L}}, \langle\phi^s\rangle_{\mathcal{S}}) \approx \langle A_0\rangle_{\mathcal{L}}\langle B_0\rangle_{\mathcal{L}} + \varepsilon(\langle A_0\rangle_{\mathcal{L}}\langle B_1\rangle_\Gamma + \langle A_1\rangle_\Gamma\langle B_0\rangle_{\mathcal{L}}) + \mathcal{O}(\varepsilon^2) \tag{A32}$$

A.2 Homogenization in the Electrode

We set $\psi_\varepsilon(\mathbf{x},t) = \psi(\mathbf{x},\mathbf{y},t,\tau_\mathrm{r},\tau_{\mathrm{m}e},\tau_{\mathrm{m}s},\tau_\mathrm{c})$ with $\psi = \{c^s,\psi^s\}$. Then, combining Eqns. 2.50, 2.51, 2.52, 2.53 and 2.55 with 2.26 we obtain:

$$\begin{aligned}
&\frac{\partial c^s}{\partial t} + Da_\ell\frac{\partial c^s}{\partial \tau_\mathrm{r}} + Pe_\ell\Big(\frac{\partial c^s}{\partial \tau_{\mathrm{m}e}} + \frac{Da_\ell}{Da_s}\Big(\frac{\partial c^s}{\partial \tau_{\mathrm{m}s}} + N_{ohm}\frac{\partial c^s}{\partial \tau_c}\Big)\Big) = \\
&Da_\ell Da_s^{-1}\nabla_\mathbf{x}\cdot\Big[\mathbf{D}^s(\nabla_\mathbf{x}c^s + \varepsilon^{-1}\nabla_\mathbf{y}c^s)\Big] \\
&+\varepsilon^{-1}Da_\ell Da_s^{-1}\nabla_\mathbf{y}\cdot\Big[\mathbf{D}^s(\nabla_\mathbf{x}c^s + \varepsilon^{-1}\nabla_\mathbf{y}c^s)\Big]
\end{aligned} \tag{B1a}$$

subject to:

$$-n_s\cdot\Big[\mathbf{D}^s(\nabla_\mathbf{x}c^s + \varepsilon^{-1}\nabla_\mathbf{y}c^s)\Big] = Da_s\sqrt{\frac{c^\ell_{max}}{c^s_{max}}}f(c^\ell_\varepsilon, c^s_\varepsilon, \phi^\ell_\varepsilon, \phi^s_\varepsilon) \tag{B1b}$$

and

$$\begin{aligned}
&\nabla_\mathbf{x}\cdot\Big[\mathbf{K}^s(\nabla_\mathbf{x}c^s + \varepsilon^{-1}\nabla_\mathbf{y}c^s)\Big] \\
&+\varepsilon^{-1}\nabla_\mathbf{y}\cdot\Big[\mathbf{K}^s(\nabla_\mathbf{x}c^s + \varepsilon^{-1}\nabla_\mathbf{y}c^s)\Big] = 0
\end{aligned} \tag{B2a}$$

subject to

$$-n_s\cdot\Big[2Pe_s\mathbf{K}^s(\nabla_\mathbf{x}c^s + \varepsilon^{-1}\nabla_\mathbf{y}c^s)\Big] = Da_s\sqrt{\frac{c^\ell_{max}}{c^s_{max}}}f(c^\ell_\varepsilon, c^s_\varepsilon, \phi^\ell_\varepsilon, \phi^s_\varepsilon) \tag{B2b}$$

and

$$-n_s\cdot\Big[2\mathbf{K}^s(\nabla_\mathbf{x}c^s + \varepsilon^{-1}\nabla_\mathbf{y}c^s)\Big] = N_{ohm} \tag{B2c}$$

respectively, where $f(c^\ell_\varepsilon, c^s_\varepsilon, \phi^\ell_\varepsilon, \phi^s_\varepsilon)$ is defined in Eqn. 2.47.

Asymptotic expansion

Substituting Eqn. 2.27 and Eqn. 2.42 in the previous equations (Eqns. B1 and B2) leads to:

$$
\begin{aligned}
&\varepsilon^{-2}\Big\{-\varepsilon^{\beta-\gamma}\nabla_{\mathbf{y}}\cdot\Big[\mathbf{D}^s\nabla_{\mathbf{y}}c_0^s\Big]\Big\}\\
&+\varepsilon^{-1}\Big\{\varepsilon^{1+\beta}\partial_{\tau_\mathrm{r}}c_0^s\\
&\qquad-\varepsilon^{\beta-\gamma}\nabla_{\mathbf{x}}\cdot\Big[\mathbf{D}^s\nabla_{\mathbf{y}}c_0^s\Big]\\
&\qquad-\varepsilon^{\beta-\gamma}\nabla_{\mathbf{y}}\cdot\Big[\mathbf{D}^s\Big(\nabla_{\mathbf{x}}c_0^s+\nabla_{\mathbf{y}}c_1^s\Big)\Big]\Big\}\\
&+\varepsilon^{0}\Big\{\partial_t c_0^s+\varepsilon^{1+\beta}\partial_{\tau_\mathrm{r}}c_1^s+\varepsilon^{-\alpha}\big(\partial_{\tau_\mathrm{me}}c_0^s+\varepsilon^{\beta-\gamma}(\partial_{\tau_{\mathrm{m}s}}c_0^s+\varepsilon^{\zeta}\partial_{\tau_\mathrm{c}}c_0^s)\big)\\
&\qquad-\varepsilon^{\beta-\gamma}\nabla_{\mathbf{x}}\cdot\Big[\mathbf{D}^s\Big(\nabla_{\mathbf{x}}c_0^s+\nabla_{\mathbf{y}}c_1^s\Big)\Big]\\
&\qquad-\varepsilon^{\beta-\gamma}\nabla_{\mathbf{y}}\cdot\Big[\mathbf{D}^s\Big(\nabla_{\mathbf{x}}c_1^s+\nabla_{\mathbf{y}}c_2^s\Big)\Big]\Big\}=\mathcal{O}(\varepsilon^1)
\end{aligned}
\tag{B3a}
$$

subject to:

$$
\begin{aligned}
&\varepsilon^{-1}\Big\{n_s\cdot\Big[\mathbf{D}^s\nabla_{\mathbf{y}}c_0^s\Big]\Big\}\\
&+\varepsilon^{0}\Big\{n_s\cdot\Big[\mathbf{D}^s\Big(\nabla_{\mathbf{x}}c_0^s+\nabla_{\mathbf{y}}c_1^s\Big)\Big]+2\varepsilon^{\gamma}\sqrt{\frac{c_{max}^{\ell}}{c_{max}^{s}}}A_0B_0\Big\}\\
&+\varepsilon^{1}\Big\{n_s\cdot\Big[\mathbf{D}^s\Big(\nabla_{\mathbf{x}}c_1^s+\nabla_{\mathbf{y}}c_2^s\Big)\Big]+2\varepsilon^{\gamma}\sqrt{\frac{c_{max}^{\ell}}{c_{max}^{s}}}(A_0B_1+A_1B_0)\Big\}=\mathcal{O}(\varepsilon^2)
\end{aligned}
\tag{B3b}
$$

and

$$
\begin{aligned}
&\varepsilon^{-2}\Big\{\nabla_{\mathbf{y}}\cdot\Big[\mathbf{K}^s\nabla_{\mathbf{y}}\phi_0^s\Big]\Big\}\\
&+\varepsilon^{-1}\Big\{\nabla_{\mathbf{x}}\cdot\Big[\mathbf{K}^s\nabla_{\mathbf{y}}\phi_0^s\Big]\\
&\qquad+\nabla_{\mathbf{y}}\cdot\Big[\mathbf{K}^s\Big(\nabla_{\mathbf{x}}\phi_0^s+\nabla_{\mathbf{y}}\phi_1^s\Big)\Big]\Big\}\\
&+\varepsilon^{0}\Big\{\nabla_{\mathbf{x}}\cdot\Big[\mathbf{K}^s\Big(\nabla_{\mathbf{x}}\phi_0^s+\nabla_{\mathbf{y}}\phi_1^s\Big)\Big]\\
&\qquad+\nabla_{\mathbf{y}}\Big[\mathbf{K}^s\Big(\nabla_{\mathbf{x}}\phi_1^s+\nabla_{\mathbf{y}}\phi_2^s\Big)\Big]\Big\}=\mathcal{O}(\varepsilon^1)
\end{aligned}
\tag{B4a}
$$

subject to:

$$\begin{aligned}
&\varepsilon^{-1}\Big\{n_s\cdot\Big[2\varepsilon^{-\delta}\mathbf{K}^s\nabla_{\mathbf{y}}\phi_0^s\Big]\Big\}\\
&+\varepsilon^{0}\Big\{n_s\cdot\Big[2\varepsilon^{-\delta}\mathbf{K}^s\Big(\nabla_{\mathbf{x}}\phi_0^s+\nabla_{\mathbf{y}}\phi_1^s\Big)\Big]+2\varepsilon^{\gamma}\sqrt{\frac{c^{\ell}_{max}}{c^{s}_{max}}}A_0B_0\Big\}\\
&+\varepsilon^{1}\Big\{n_s\cdot\Big[2\varepsilon^{-\delta}\mathbf{K}^s\Big(\nabla_{\mathbf{x}}\phi_1^s+\nabla_{\mathbf{y}}\phi_2^s\Big)\Big]+2\varepsilon^{\gamma}\sqrt{\frac{c^{\ell}_{max}}{c^{s}_{max}}}(A_0B_1+A_1B_0)\Big\}=\mathcal{O}(\varepsilon^1)
\end{aligned} \tag{B4b}$$

and

$$\begin{aligned}
&\varepsilon^{-1}\Big\{n_s\cdot\Big[2\mathbf{K}^s\nabla_{\mathbf{y}}\phi_0^s\Big]\Big\}\\
&+\varepsilon^{0}\Big\{n_s\cdot\Big[2\mathbf{K}^s\Big(\nabla_{\mathbf{x}}\phi_0^s+\nabla_{\mathbf{y}}\phi_1^s\Big)\Big]-\varepsilon^{\zeta}\Big\}\\
&+\varepsilon^{1}\Big\{n_s\cdot\Big[2\mathbf{K}^s\Big(\nabla_{\mathbf{x}}\phi_1^s+\nabla_{\mathbf{y}}\phi_2^s\Big)\Big]\Big\}=\mathcal{O}(\varepsilon^1)
\end{aligned} \tag{B4c}$$

Where the non-linear term present in the Butler-Volmer is expanded in a McLaurin series as in Eqn. A5.

Terms of order $\mathcal{O}(\varepsilon^{-2})$

Collecting the leading-order terms in the mass transport equations (Eqn. B3), we obtain:

$$-\varepsilon^{\beta-\gamma}\nabla_{\mathbf{y}}\cdot\Big[\mathbf{D}^s\nabla_{\mathbf{y}}c_0^s\Big]=0 \tag{B5a}$$

subject to:

$$n_s\cdot\Big[\mathbf{D}^s\nabla_{\mathbf{y}}c_0^s\Big]=0 \tag{B5b}$$

Similarly, at the leading order, the charge transport equations (Eqn. B4) are:

$$\nabla_{\mathbf{y}}\cdot\Big[\mathbf{K}^s\nabla_{\mathbf{y}}\phi_0^s\Big]=0 \tag{B6a}$$

subject to:

$$n_s \cdot \left[2\varepsilon^{-\delta} \mathbf{K}^s \nabla_{\mathbf{y}} \phi_0^s \right] = 0 \tag{B6b}$$

and

$$n_s \cdot \left[2\mathbf{K}^s \nabla_{\mathbf{y}} \phi_0^s \right] = 0 \tag{B6c}$$

Homogeneity of Eqns. B5 and B6 guarantees that c_0^s and ϕ_0^s are independent of y:

$$\begin{aligned} c_0^s &= c_0^s(\mathbf{x}, t, \tau_{\mathrm{r}}, \tau_{\mathrm{m}e}, \tau_{\mathrm{m}s}, \tau_{\mathrm{c}}) \\ \phi_0^s &= \phi_0^s(\mathbf{x}, t, \tau_{\mathrm{r}}, \tau_{\mathrm{m}e}, \tau_{\mathrm{m}s}, \tau_{\mathrm{c}}) \end{aligned} \tag{B7}$$

Terms of order $\mathcal{O}(\varepsilon^{-1})$

Since $\nabla_{\mathbf{y}} c_0^s = \mathbf{0}$ and $\nabla_{\mathbf{y}} \phi_0^s = \mathbf{0}$, the mass balance equations (Eqns. A1) at order $\mathcal{O}(\varepsilon^{-1})$ simplifies to:

$$\varepsilon^{\beta-\gamma} \nabla_{\mathbf{y}} \cdot \left[\mathbf{D}^s \left(\nabla_{\mathbf{x}} c_0^s + \nabla_{\mathbf{y}} c_1^s \right) \right] = \varepsilon^{1+\beta} \partial_{\tau_{\mathrm{r}}} c_0^s \tag{B8a}$$

subject to:

$$n_s \cdot \left[\mathbf{D}^s \left(\nabla_{\mathbf{x}} c_0^s + \nabla_{\mathbf{y}} c_1^s \right) \right] = -2\varepsilon^{\gamma} \sqrt{\frac{c_{max}^{\ell}}{c_{max}^s}} A_0 B_0 \tag{B8b}$$

By integrating Eqn. B8a over $\mathcal{S}$ with respect to $\mathbf{y}$ and Eqn. B8b over Γ with respect to $\mathbf{y}$, following the definition in 2.28 and while accounting for the periodicity of the coefficients on the external boundary of the unit cell $\partial \mathrm{Y}$, we obtain:

$$\varepsilon^{1+\gamma} \partial_{\tau_{\mathrm{r}}} c_0^s = -2\mathcal{K}^{\star} \eta \varepsilon^{\gamma} \sqrt{\frac{c_{max}^{\ell}}{c_{max}^s}} A_0 B_0 \tag{B9}$$

where $\mathcal{K}^{\star}$ is defined in Eqn. 2.65. Combining B8a with B9 to eliminate the temporal derivative, we obtain:

$$\nabla_{\mathbf{y}} \cdot \left[\mathbf{D}^s\left(\nabla_{\mathbf{x}} c_0^s + \nabla_{\mathbf{y}} c_1^s\right)\right] + 2\mathcal{K}^\star \eta \varepsilon^\gamma \sqrt{\frac{c^\ell_{max}}{c^s_{max}}} A_0 B_0 = 0 \tag{B10a}$$

subject to:

$$n_s \cdot \left[\mathbf{D}^s\left(\nabla_{\mathbf{x}} c_0^s + \nabla_{\mathbf{y}} c_1^s\right)\right] + 2\varepsilon^\gamma \sqrt{\frac{c^\ell_{max}}{c^s_{max}}} A_0 B_0 = 0 \tag{B10b}$$

Similarly, for the charge balance equation at the order of $\mathcal{O}(\varepsilon^{-1})$ (Eqns B2):

$$\nabla_{\mathbf{y}} \cdot \left[\mathbf{K}^s\left(\nabla_{\mathbf{x}} \phi_0^s + \nabla_{\mathbf{y}} \phi_1^s\right)\right] = 0 \tag{B11a}$$

$$n_s \cdot \left[2\varepsilon^{-\delta}\mathbf{K}^s\left(\nabla_{\mathbf{x}} \phi_0^s + \nabla_{\mathbf{y}} \phi_1^s\right)\right] + 2\varepsilon^\gamma \sqrt{\frac{c^\ell_{max}}{c^s_{max}}} A_0 B_0 = 0 \tag{B11b}$$

and

$$n_s \cdot \left[2\mathbf{K}^s\left(\nabla_{\mathbf{x}} \phi_0^s + \nabla_{\mathbf{y}} \phi_1^s\right)\right] - \varepsilon^\zeta = 0 \tag{B11c}$$

Eqns. B10 and B11 form boundary value problems for both c_1^s and ϕ_1^s. Following Ref. [45], we look for solutions in the form:

$$\begin{aligned}
c_1^s(x,y,t,\tau_{\mathrm{r}},\tau_{\mathrm{m}e},\tau_{\mathrm{m}s},\tau_{\mathrm{c}}) &= \chi_3(y)\nabla_{\mathbf{x}} c_0^s(x,t,\tau_{\mathrm{r}},\tau_{\mathrm{m}e},\tau_{\mathrm{m}s},\tau_{\mathrm{c}}) + \bar{c}_1^s(x,t,\tau_{\mathrm{r}},\tau_{\mathrm{m}e},\tau_{\mathrm{m}s},\tau_{\mathrm{c}})\\
\phi_1^s(x,y,t,\tau_{\mathrm{r}},\tau_{\mathrm{m}e},\tau_{\mathrm{m}s},\tau_{\mathrm{c}}) &= \chi_4(y)\nabla_{\mathbf{x}} \phi_0^s(x,t,\tau_{\mathrm{r}},\tau_{\mathrm{m}e},\tau_{\mathrm{m}s},\tau_{\mathrm{c}}) + \bar{\phi}_1^s(x,t,\tau_{\mathrm{r}},\tau_{\mathrm{m}e},\tau_{\mathrm{m}s},\tau_{\mathrm{c}})
\end{aligned} \tag{B12}$$

Substituting B12 into B10 and B11 we obtain:

$$\nabla_{\mathbf{y}} \cdot \left[\mathbf{D}^s\left(I + \nabla_{\mathbf{y}}\chi_3\right)\nabla_{\mathbf{x}} c_0^s\right] + 2\mathcal{K}^\star \eta \varepsilon^\gamma \sqrt{\frac{c^\ell_{max}}{c^s_{max}}} A_0 B_0 = 0 \tag{B13a}$$

subject to:

$$n_s \cdot \left[\mathbf{D}^s\left(I + \nabla_{\mathbf{y}}\chi_3\right)\nabla_{\mathbf{x}} c_0^s\right] + 2\varepsilon^\gamma \sqrt{\frac{c^\ell_{max}}{c^s_{max}}} A_0 B_0 = 0 \tag{B13b}$$

and

$$\nabla_{\mathbf{y}} \cdot \left[\mathbf{K}^s \left(I + \nabla_{\mathbf{y}} \chi_4\right) \nabla_{\mathbf{x}} \phi_0^s\right] = 0 \tag{B14a}$$

subject to:

$$n_s \cdot \left[2\varepsilon^{-\delta} \mathbf{K}^s \left(I + \nabla_{\mathbf{y}} \chi_4\right) \nabla_{\mathbf{x}} \phi_0^s\right] + 2\varepsilon^{\gamma} \sqrt{\frac{c_{max}^{\ell}}{c_{max}^{s}}} A_0 B_0 = 0 \tag{B14b}$$

and

$$n_s \cdot \left[2\mathbf{K}^s \left(I + \nabla_{\mathbf{y}} \chi_4\right) \nabla_{\mathbf{x}} c_0^s\right] - \varepsilon^{\zeta} = 0 \tag{B14c}$$

Eqns. B13 and B14 define the closure variables $\chi_3(y)$ and $\chi_4(y)$. The coupling of $\chi_3(y)$ and $\chi_4(y)$ with $c_0^s(x)$, $\phi_0^s(x)$, $A_0(x)$ and $B_0(x)$ through the boundary value problems B10 and B11 is incompatible with the closure variables' general representation postulated in B12. This inconsistency is resolved by imposing the following constraints on the exponents γ and β. If we choose $\delta > \max 0, -\gamma$ and $\gamma < 0$, then the terms that contain $\varepsilon^{-\gamma}$ or ε^{δ} are negligible. Moreover, we need the condition $\zeta > 0$ to neglect the term associated to the Charge number and consider the system periodic. Considering also that the conductivity tensor $\mathbf{K}^s$ and the diffusion tensor $\mathbf{D}^s$ are function of concentration c^s and potential ϕ^s, with an order ε^1 approximation we have that $\mathbf{K}^s \approx \mathbf{K}^s(c_0^s, \phi_0^s)$ and $\mathbf{D}^s \approx \mathbf{K}^s(c_0^s, \phi_0^s)$. As a result, $\chi_3(y) = \chi_4(y) = \chi_s(y)$. The closure variable $\chi_s(y)$ defines the cell problem and describes the behavior of the effective diffusion and conductivity tensors due to the morphology of the system. Under these hypothesis, Eqns. B13 and B14 simplifies to:

$$\nabla_{\mathbf{y}} \cdot \left[\left(I + \nabla_{\mathbf{y}} \chi_s\right)\right] = 0 \tag{B15a}$$

subject to:

$$\mathbf{n}_s \cdot \left[\left(I + \nabla_{\mathbf{y}} \chi_s\right)\right] = 0 \tag{B15b}$$

Terms of order $\mathcal{O}(\varepsilon^0)$

Collecting the zeroth-order term in the mass balance equation (Eqns B1a) and first-order term in the corresponding boundary condition (Eqns B1b), and recalling the results obtained in the previous steps, we have:

$$\begin{aligned}&\partial_t c_0^s+\varepsilon^{1+\beta}\partial_{\tau_\mathrm{r}} c_1^s+\varepsilon^{-\alpha}\left(\partial_{\tau_{\mathrm{m}e}} c_0^s+\varepsilon^{\beta-\gamma}(\partial_{\tau_{\mathrm{m}s}} c_0^s+\varepsilon^{\zeta}\partial_{\tau_\mathrm{c}} c_0^s)\right)\\&-\varepsilon^{\beta-\gamma}\nabla_{\mathbf{x}}\cdot\left[\mathbf{D}^s\left(\nabla_{\mathbf{x}} c_0^s+\nabla_{\mathbf{y}} c_1^s\right)\right]-\varepsilon^{\beta-\gamma}\nabla_{\mathbf{y}}\cdot\left[\mathbf{D}^s\left(\nabla_{\mathbf{x}} c_1^s+\nabla_{\mathbf{y}} c_2^s\right)\right]=0\end{aligned} \tag{B16a}$$

subject to:

$$n_s\cdot\left[\mathbf{D}^s\left(\nabla_{\mathbf{x}} c_1^s+\nabla_{\mathbf{y}} c_2^s\right)\right]+2\varepsilon^{\gamma}\sqrt{\frac{c_{max}^{\ell}}{c_{max}^{s}}}(A_0B_1+A_1B_0)=0 \tag{B16b}$$

integrating Eqn. B16a over $\mathcal{S}$ with respect to **y** and Eqn.B16b over Γ with respect to **y**, following the definition in 2.28 and, taking into account the periodic boundary condition:

$$\begin{aligned}&\partial_t\langle c_0^s\rangle_s+\varepsilon^{1+\beta}\partial_r\langle c_1^s\rangle_s+\varepsilon^{-\alpha}\left(\partial_{m,l}\langle c_0^s\rangle_s+\varepsilon^{\beta-\gamma}(\partial_{m,s}\langle c_0^s\rangle_s+\varepsilon^{\zeta}\partial_c\langle c_0^s\rangle_s)\right)\\&-\varepsilon^{\beta-\gamma}\nabla_{\mathbf{x}}\cdot\left[\mathbf{D}^{s\star\star}\nabla_{\mathbf{x}}\langle c_0^s\rangle_s\right]+2\mathcal{K}^{\star}\eta\varepsilon^{\beta}\left(\langle A_0\rangle_{\mathcal{L}}\langle B_1\rangle_{\Gamma}+\langle A_1\rangle_{\Gamma}\langle B_0\rangle_{\mathcal{L}}\right)=0\end{aligned} \tag{B17}$$

Now we recall that:

$$\langle c^s\rangle_s=\langle c_0^s\rangle_s+\varepsilon\langle c_1^s\rangle_s+\mathcal{O}(\varepsilon^2) \tag{B18a}$$

$$\langle \phi^s\rangle_s=\langle \phi_0^s\rangle_s+\varepsilon\langle \phi_1^s\rangle_s+\mathcal{O}(\varepsilon^2) \tag{B18b}$$

$$\varepsilon^{1+\gamma}\partial_{\tau_\mathrm{r}} c_0^s=-2\mathcal{K}^{\star}\eta\varepsilon^{\gamma}\sqrt{\frac{c_{max}^{\ell}}{c_{max}^{s}}}A_0B_0 \tag{B18c}$$

Multiplying the temporal derivative of Eqn. B18a by ε, we obtain:

$$\varepsilon\partial_t\langle c^s\rangle_s=\varepsilon\partial_t\langle c_0^s\rangle_s+\varepsilon^{1+\beta}\partial_r\langle c_0^s\rangle_s+\varepsilon^{1-\alpha}\left(\partial_{m,l}\langle c_0^s\rangle_s+\varepsilon^{\beta-\gamma}(\partial_{m,s}\langle c_0^s\rangle_s+\varepsilon^{\zeta}\partial_c\langle c_0^s\rangle_s)\right)+\mathcal{O}(\varepsilon^2) \tag{B19}$$

Then, integrating Eqn. B18c over $\mathcal{S}$ with respect to $\mathbf{y}$ and adding to Eqn. B19 we obtain:

$$\begin{aligned}&\varepsilon\partial_t\langle c^s\rangle_s + 2\mathcal{K}^\star\eta\varepsilon^\beta\sqrt{\frac{c^\ell_{max}}{c^s_{max}}}\langle A_0\rangle_\mathcal{L}\langle B_0\rangle_\mathcal{L} = \\ &\varepsilon\partial_t\langle c_0^s\rangle_s + \varepsilon^{1-\alpha}\big(\partial_{m,l}\langle c_0^s\rangle_s+\varepsilon^{\beta-\gamma}(\partial_{m,s}\langle c_0^s\rangle_s+\varepsilon^\zeta\partial_c\langle c_0^s\rangle_s)\big)+\mathcal{O}(\varepsilon^2)\end{aligned}\tag{B20}$$

Multiplying B17 by ε:

$$\begin{aligned}&\varepsilon\partial_t\langle c_0^s\rangle_s + \varepsilon^{1-\alpha}\big(\partial_{m,l}\langle c_0^s\rangle_s+\varepsilon^{\beta-\gamma}(\partial_{m,s}\langle c_0^s\rangle_s+\varepsilon^\zeta\partial_c\langle c_0^s\rangle_s)\big) \\ &-\varepsilon^{1+\beta-\gamma}\nabla_\mathbf{x}\cdot\Big[\mathbf{D}^{s\star\star}\nabla_\mathbf{x}\langle c_0^s\rangle_s\Big]+2\mathcal{K}^\star\eta\varepsilon^{1+\beta}\sqrt{\frac{c^\ell_{max}}{c^s_{max}}}\big(\langle A_0\rangle_\mathcal{L}\langle B_1\rangle_\Gamma+\langle A_1\rangle_\Gamma\langle B_0\rangle_\mathcal{L}\big)=\mathcal{O}(\varepsilon^2)\end{aligned}\tag{B21}$$

Combining Eqn. B20 and B21, we obtain:

$$\begin{aligned}&\varepsilon\partial_t\langle c^s\rangle_s + 2\mathcal{K}^\star\eta\varepsilon^\beta\langle A_0\rangle_\mathcal{L}\langle B_0\rangle_\mathcal{L} \\ &-\varepsilon^{1+\beta-\gamma}\nabla_\mathbf{x}\cdot\Big[\mathbf{D}^{s\star\star}\nabla_\mathbf{x}\langle c_0^s\rangle_s\Big]+2\mathcal{K}^\star\eta\varepsilon^{1+\beta}\sqrt{\frac{c^\ell_{max}}{c^s_{max}}}\big(\langle A_0\rangle_\mathcal{L}\langle B_1\rangle_\Gamma+\langle A_1\rangle_\Gamma\langle B_0\rangle_\mathcal{L}\big)=\mathcal{O}(\varepsilon^2)\end{aligned}\tag{B22}$$

Combining the result of Eqn. B22 with the expansions:

$$\begin{aligned}\varepsilon\langle c^s\rangle_s &= \varepsilon\langle c_0^s\rangle_s+\mathcal{O}(\varepsilon^2)=\varepsilon c_0^s+\mathcal{O}(\varepsilon^2)\\ \varepsilon\langle \phi^s\rangle_s &= \varepsilon\langle \phi_0^s\rangle_s+\mathcal{O}(\varepsilon^2)=\varepsilon \phi_0^s+\mathcal{O}(\varepsilon^2)\end{aligned}\tag{B23}$$

and recalling the definitions of $Da_s=\varepsilon^\gamma$ and $Pe_s=\varepsilon^{-\delta}$ and assuming $\langle\psi_\ell\rangle_\Gamma=\langle\psi_\ell\rangle_\mathcal{L}$ and $\langle\psi_s\rangle_\Gamma=\langle\psi_s\rangle_s$, where $\psi=\{c,\phi\}$, leads to the homogenized equation of the mass transport within the solid phase:

$$\partial_t\langle c^s\rangle_s = Da_\ell Da_s^{-1}\nabla_\mathbf{x}\cdot\Big[\mathbf{D}^{s\star\star}\nabla_\mathbf{x}\langle c^s\rangle_s\Big]-2\varepsilon^{-1}\eta Da_\ell\sqrt{\frac{c^\ell_{max}}{c^s_{max}}}\mathcal{K}^\star f(\langle c^\ell\rangle_\mathcal{L},\langle c^s\rangle_s,\langle\phi^\ell\rangle_\mathcal{L},\langle\phi^s\rangle_s)\tag{B24}$$

where:

$$f(\langle c^\ell\rangle_{\mathcal{L}}, \langle c^s\rangle_{\mathcal{S}}, \langle \phi^\ell\rangle_{\mathcal{L}}, \langle \phi^s\rangle_{\mathcal{S}}) \approx \langle A_0\rangle_{\mathcal{L}}\langle B_0\rangle_{\mathcal{L}} + \varepsilon(\langle A_0\rangle_{\mathcal{L}}\langle B_1\rangle_{\Gamma} + \langle A_1\rangle_{\Gamma}\langle B_0\rangle_{\mathcal{L}}) + \mathcal{O}(\varepsilon^2) \tag{B25}$$

Similarly, collecting the zeroth-order term in the charge balance equation (Eqns B2a) and first-order term in the corresponding boundary condition (Eqns B2b):

$$\nabla_{\mathbf{x}} \cdot \left[\mathbf{K}^s\left(\nabla_{\mathbf{x}}\phi_0^s + \nabla_{\mathbf{y}}\phi_1^s\right)\right] + \nabla_{\mathbf{y}}\left[\mathbf{K}^s\left(\nabla_{\mathbf{x}}\phi_1^s + \nabla_{\mathbf{y}}\phi_2^s\right)\right] = 0 \tag{B26a}$$

subject to:

$$n_s \cdot \left[2\varepsilon^{-\delta}\mathbf{K}^s\left(\nabla_{\mathbf{x}}\phi_1^s + \nabla_{\mathbf{y}}\phi_2^s\right)\right] + 2\varepsilon^{\gamma}\sqrt{\frac{c^\ell_{max}}{c^s_{max}}}(A_0B_1 + A_1B_0) = 0 \tag{B26b}$$

The charge external boundary condition (Eqn. B2c) is less restrictive than the Butler-Volmer equation, and so it will not be reported anymore. By multiplying Eqns. B26 by ε and adding them to Eqns. B14:

$$\begin{aligned} &\varepsilon\nabla_{\mathbf{x}} \cdot \left[2\varepsilon^{-\delta}\mathbf{K}^s\left(\nabla_{\mathbf{x}}\phi_0^s + \nabla_{\mathbf{y}}\phi_1^s\right)\right] \\ &+ \nabla_{\mathbf{y}} \cdot \left[2\varepsilon^{-\delta}\mathbf{K}^s\left(\nabla_{\mathbf{x}}\phi_0^s + \nabla_{\mathbf{y}}\phi_1^s\right) + 2\varepsilon^{1-\delta}\mathbf{K}^s\left(\nabla_{\mathbf{x}}\phi_1^s + \nabla_{\mathbf{y}}\phi_2^s\right)\right] = 0 \end{aligned} \tag{B27a}$$

subject to:

$$\begin{aligned} &n_s \cdot \left[2\varepsilon^{-\delta}\mathbf{K}^s\left(\nabla_{\mathbf{x}}\phi_0^s + \nabla_{\mathbf{y}}\phi_1^s\right) + 2\varepsilon^{1-\delta}\mathbf{K}^s\left(\nabla_{\mathbf{x}}\phi_1^s + \nabla_{\mathbf{y}}\phi_2^s\right)\right] = \\ &-2\varepsilon^{\gamma}\sqrt{\frac{c^\ell_{max}}{c^s_{max}}}(A_0B_0 + \varepsilon(A_1B_0 + A_0B_1)) \end{aligned} \tag{B27b}$$

By integrating Eqn. B27a over $\mathcal{S}$ with respect to **y** and Eqn. B27b over Γ with respect to **y**, following the definition in 2.28 and, taking into account the periodic boundary condition:

$$\varepsilon\nabla_{\mathbf{x}} \cdot \left[2\varepsilon^{-\delta}\mathbf{K}^{s\star\star}\nabla_{\mathbf{x}}\phi_0^s\right] = 2\mathcal{K}^{\star}\eta\varepsilon^{\gamma}\sqrt{\frac{c^\ell_{max}}{c^s_{max}}}\left(\langle A_0\rangle_{\mathcal{L}}\langle B_0\rangle_{\mathcal{L}} + \varepsilon(\langle A_0\rangle_{\mathcal{L}}\langle B_1\rangle_{\Gamma} + \langle A_1\rangle_{\Gamma}\langle B_0\rangle_{\mathcal{L}})\right) \tag{B28}$$

$$\begin{aligned} \varepsilon\langle c^s\rangle_s &= \varepsilon\langle c_0^s\rangle_s + \mathcal{O}(\varepsilon^2) = \varepsilon c_0^s + \mathcal{O}(\varepsilon^2) \\ \varepsilon\langle \phi^s\rangle_s &= \varepsilon\langle \phi_0^s\rangle_s + \mathcal{O}(\varepsilon^2) = \varepsilon \phi_0^s + \mathcal{O}(\varepsilon^2) \end{aligned} \tag{B29}$$

and recalling the definitions of $Da_s = \varepsilon^\gamma$ and $Pe_s = \varepsilon^{-\delta}$ and assuming $\langle\psi_\ell\rangle_\Gamma = \langle\psi_\ell\rangle_\mathcal{L}$ and $\langle\psi_s\rangle_\Gamma = \langle\psi_s\rangle_s$, where $\psi = \{c, \phi\}$, leads to the homogenized equation of the charge transport within the solid phase::

$$\nabla_\mathbf{x} \cdot \left[2Pe_s \mathbf{K}^{s\star\star} \nabla_\mathbf{x} \langle\phi^s\rangle_s\right] = 2\varepsilon^{-1}\eta Da_s \sqrt{\frac{c^\ell_{max}}{c^s_{max}}}\mathcal{K}^\star f(\langle c^\ell\rangle_\mathcal{L}, \langle c^s\rangle_s, \langle\phi^\ell\rangle_\mathcal{L}, \langle\phi^s\rangle_s) \tag{B30}$$

where:

$$f(\langle c^\ell\rangle_\mathcal{L}, \langle c^s\rangle_\mathcal{S}, \langle\phi^\ell\rangle_\mathcal{L}, \langle\phi^s\rangle_\mathcal{S}) \approx \langle A_0\rangle_\mathcal{L}\langle B_0\rangle_\mathcal{L} + \varepsilon(\langle A_0\rangle_\mathcal{L}\langle B_1\rangle_\Gamma + \langle A_1\rangle_\Gamma\langle B_0\rangle_\mathcal{L}) + \mathcal{O}(\varepsilon^2) \tag{B31}$$

Appendix B

Results of the homogenized model

In this Appendix section, all the cases analyzed for validating the reduced order model are reported. We remember that, for this work purpose, we studied the effect of the Damköhler number and the C-rate over the error evaluation. We remember that the C-rate influences the current value and the N_{ohm} number consequently. For a more clear understanding and interpretation of the data collected, we chose to show the plot at different C-rates values, since this information is more understandable. The system with $Da = 0.05$ falls into the applicability regimes and therefore we were expecting an error comparable to the geometrical parameter ε. Indeed the error exceed the dashed red line of 0.05 only at high current values. Looking more into details the maximum error reached is equal to 0.093 and is obtained evaluating the lithium ion concentration in the liquid phase in the anode side. This result totally confirms the up-scalability of the LiBs pore-scale governing equations. The obtained reduced order model well reproduces the pore-scale results except for a certain error ($\varepsilon = 0.05$) chosen a priori. The two sets of cases with $Da = 0.5$ and $Da = 5$, even if are out of the applicability regimes boundaries, presents errors in the acceptable range. This confirms that the applicability regimes are sufficient but not necessary conditions, as better explained in the main text.

Da=0.05

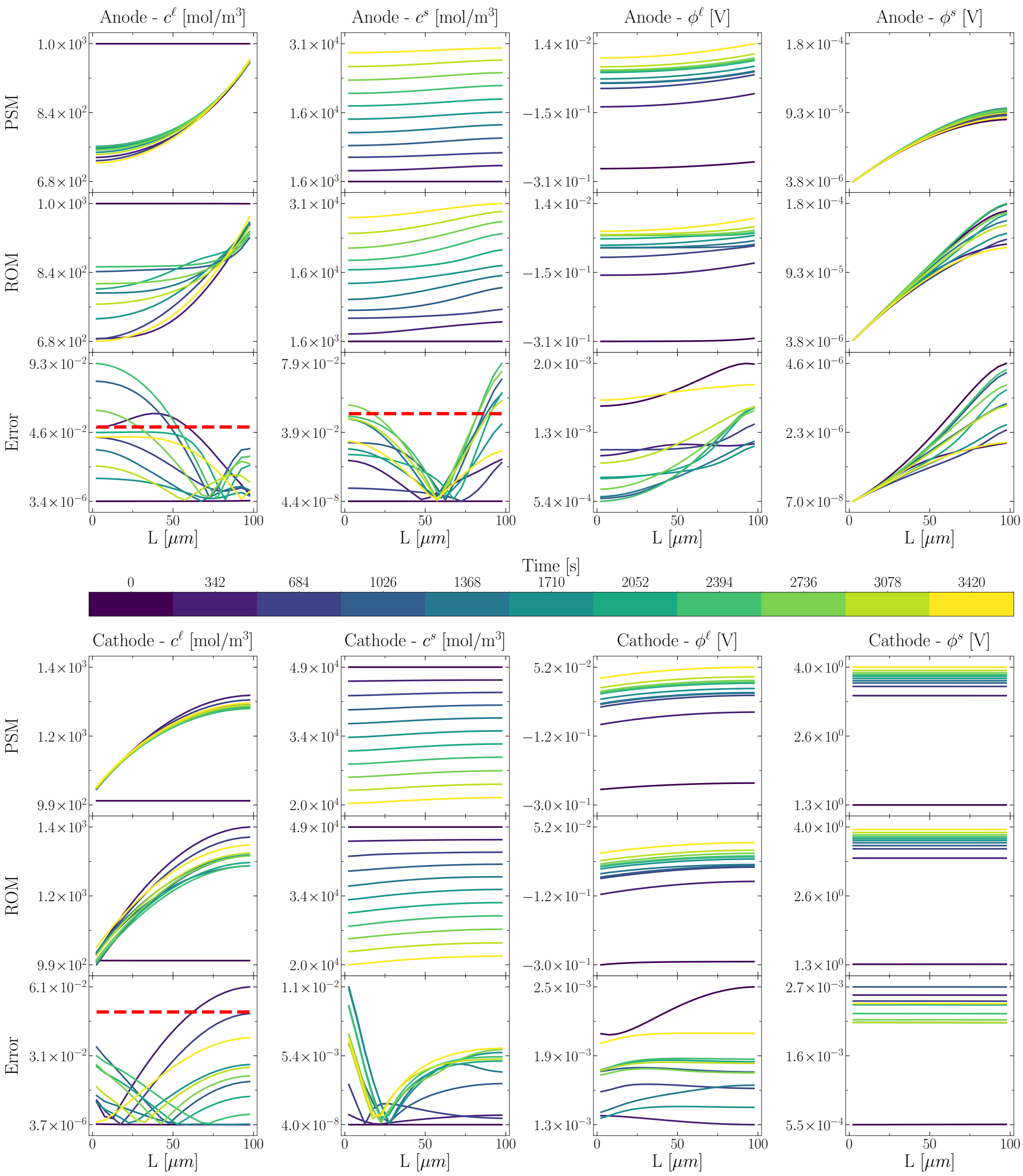

Fig. B.1 Charge at $C_{rate} = 1C$. In the first row of each group of plots, the Pore Scale Model (PSM) is presented, then, in the second one, there is the Reduced Order Model (ROM), and finally the Error between the two methods.

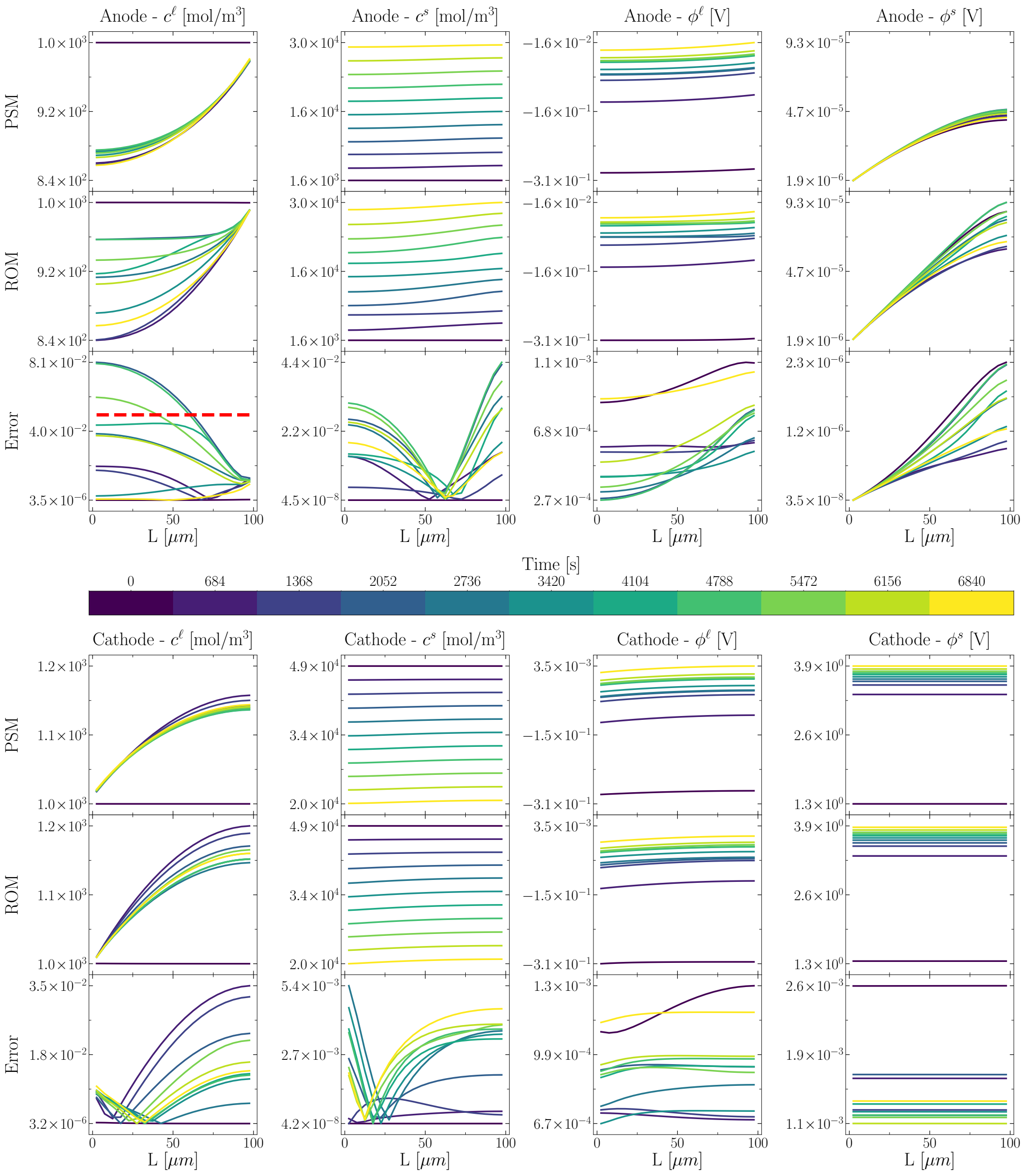

Fig. B.2 Charge at $C_{rate} = C2$. In the first row of each group of plots, the Pore Scale Model (PSM) is presented, then, in the second one, there is the Reduced Order Model (ROM), and finally the Error between the two methods.

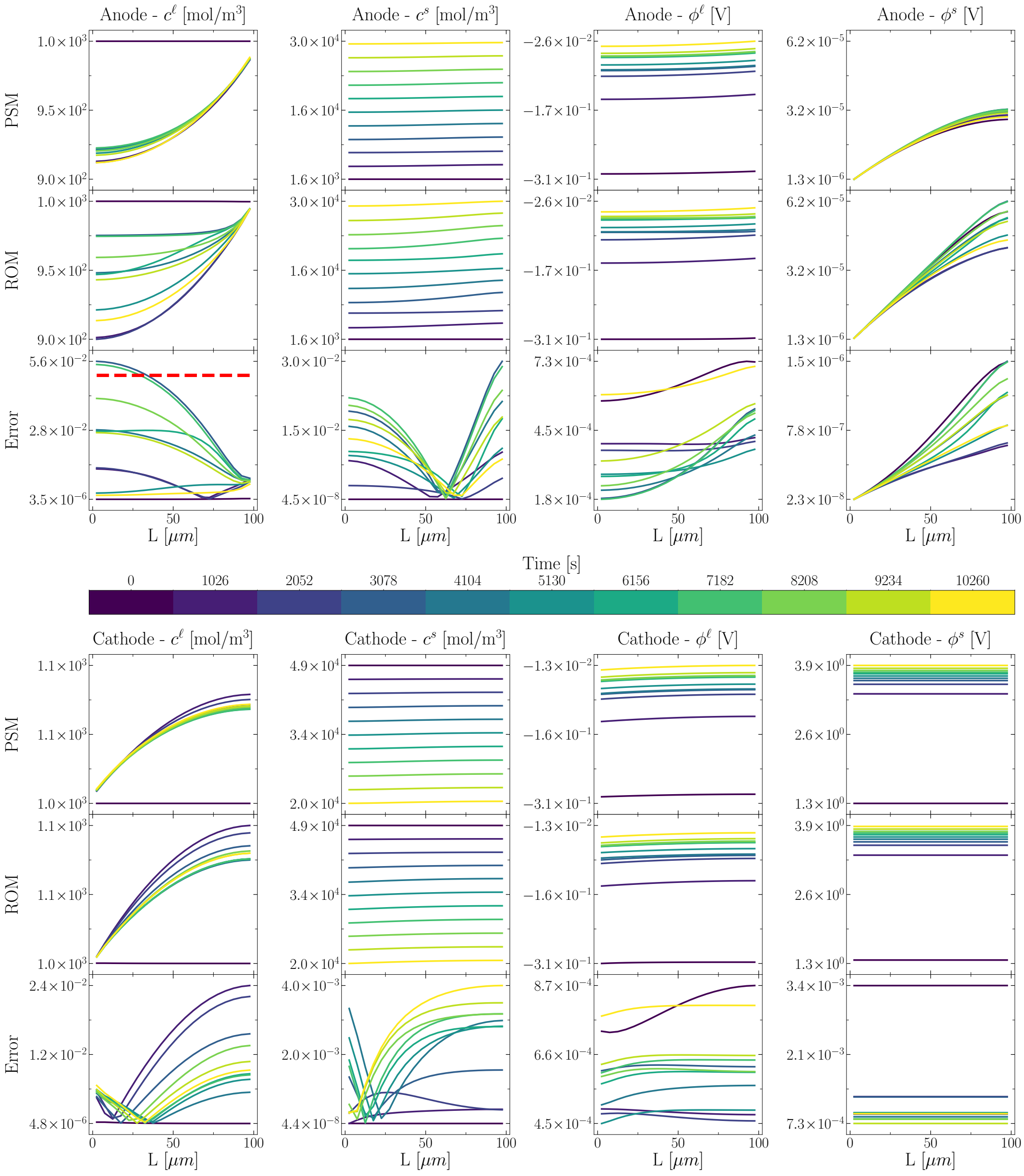

Fig. B.3 Charge at $C_{rate} = C3$. In the first row of each group of plots, the Pore Scale Model (PSM) is presented, then, in the second one, there is the Reduced Order Model (ROM), and finally the Error between the two methods.

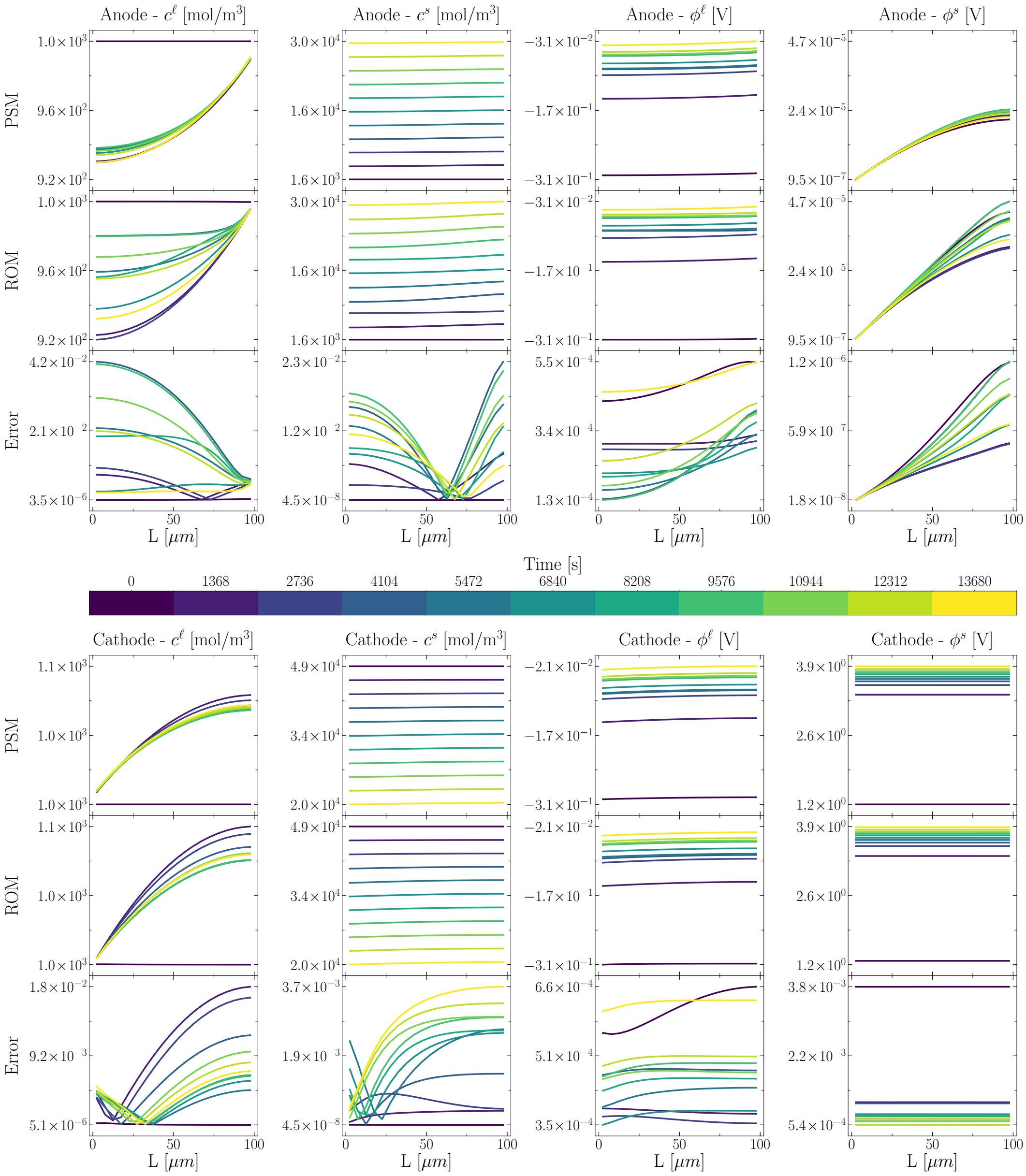

Fig. B.4 Charge at $C_{rate} = C4$. In the first row of each group of plots, the Pore Scale Model (PSM) is presented, then, in the second one, there is the Reduced Order Model (ROM), and finally the Error between the two methods.

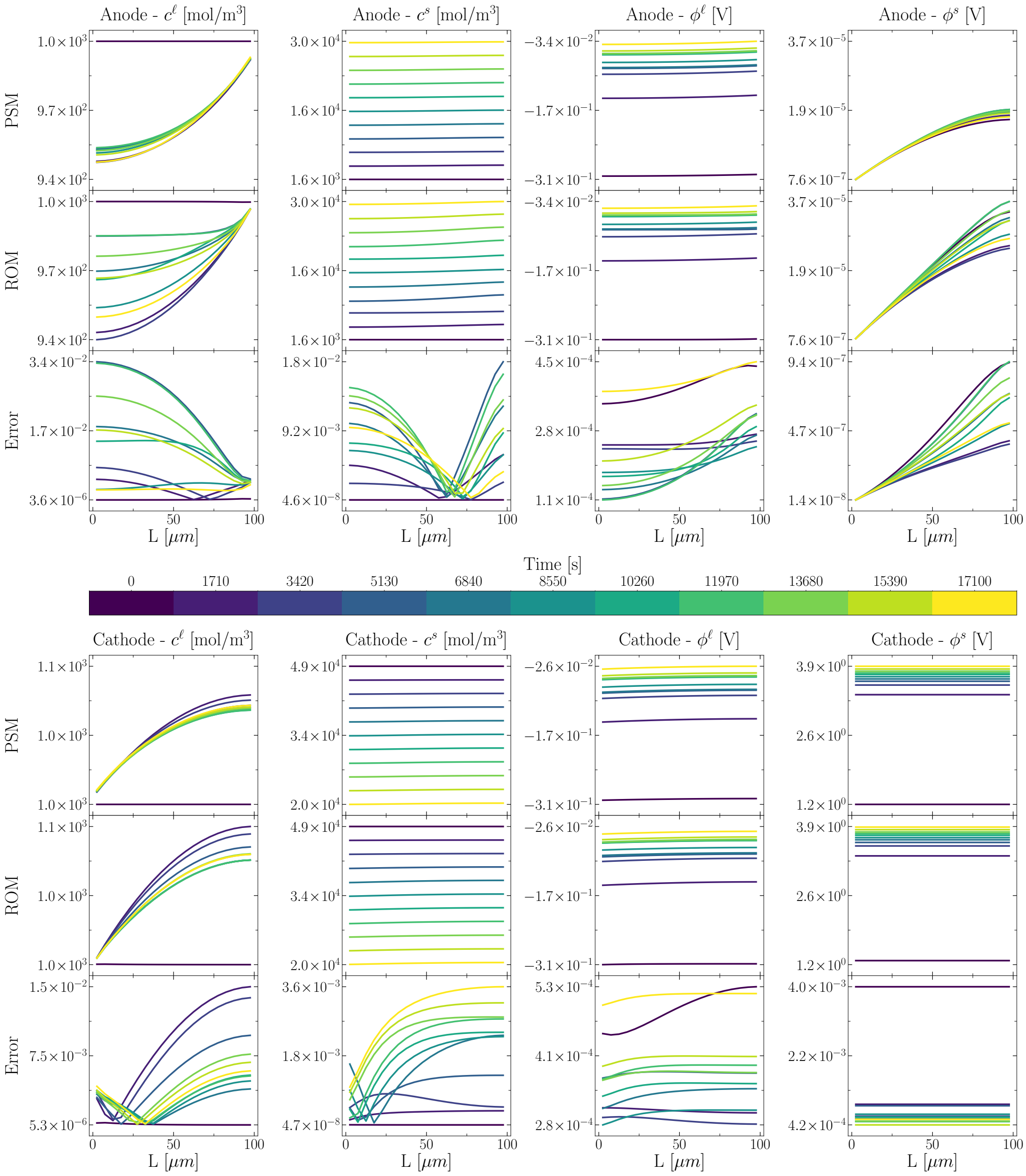

Fig. B.5 Charge at $C_{rate} = C5$. In the first row of each group of plots, the Pore Scale Model (PSM) is presented, then, in the second one, there is the Reduced Order Model (ROM), and finally the Error between the two methods.

Da=0.5

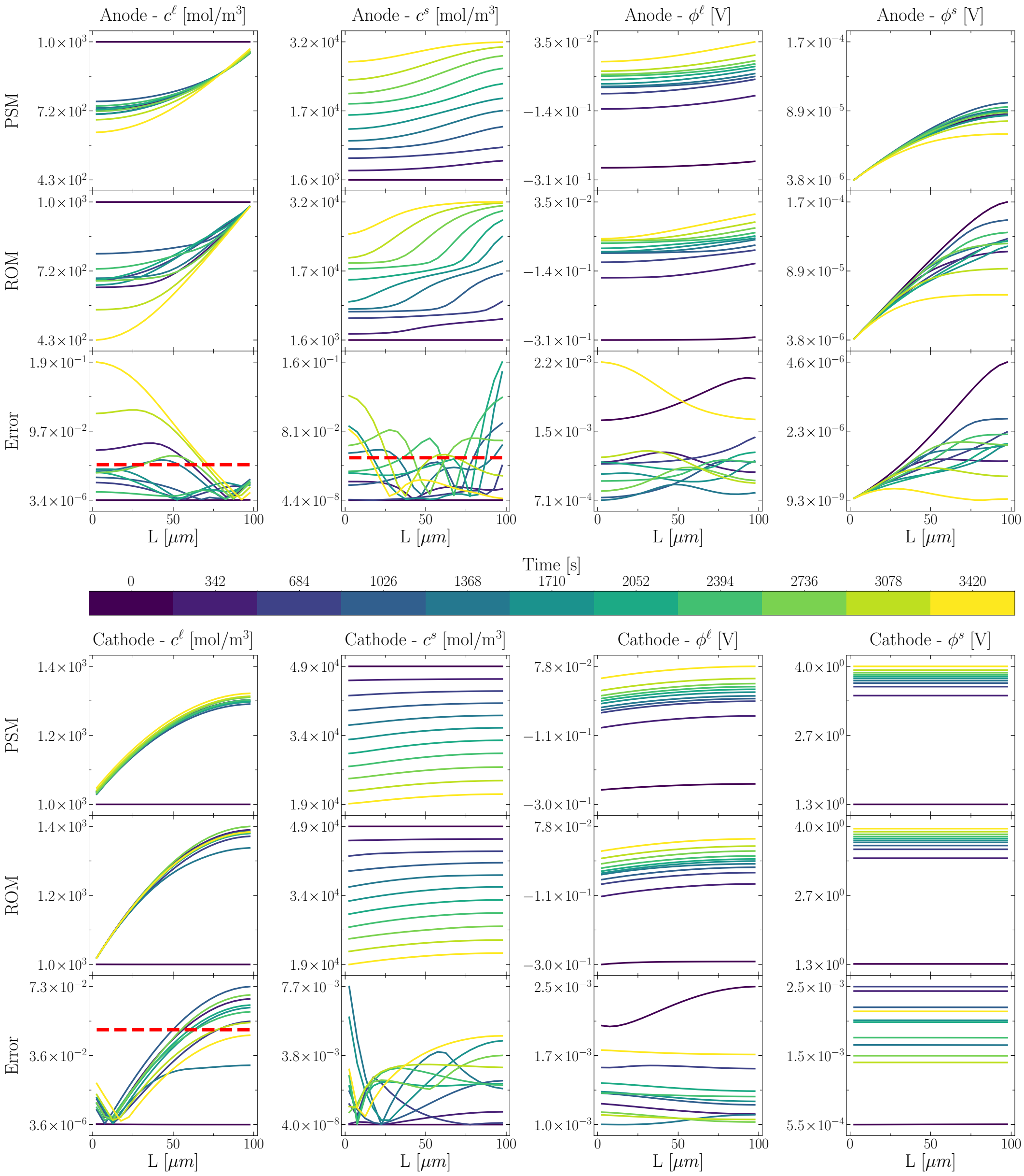

Fig. B.6 Charge at $C_{rate} = 1C$. In the first row of each group of plots, the Pore Scale Model (PSM) is presented, then, in the second one, there is the Reduced Order Model (ROM), and finally the Error between the two methods.

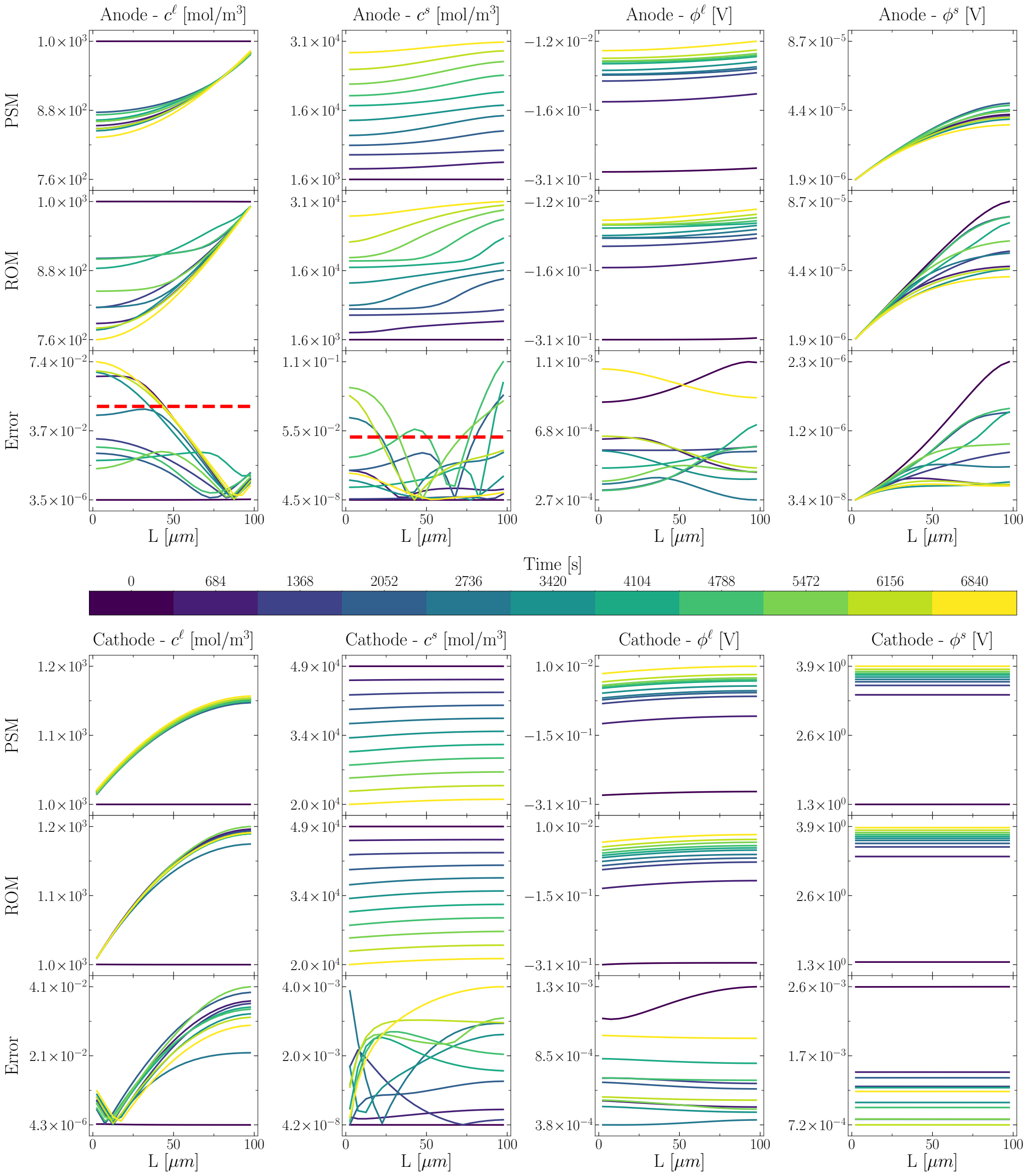

Fig. B.7 Charge at $C_{rate} = C2$. In the first row of each group of plots, the Pore Scale Model (PSM) is presented, then, in the second one, there is the Reduced Order Model (ROM), and finally the Error between the two methods.

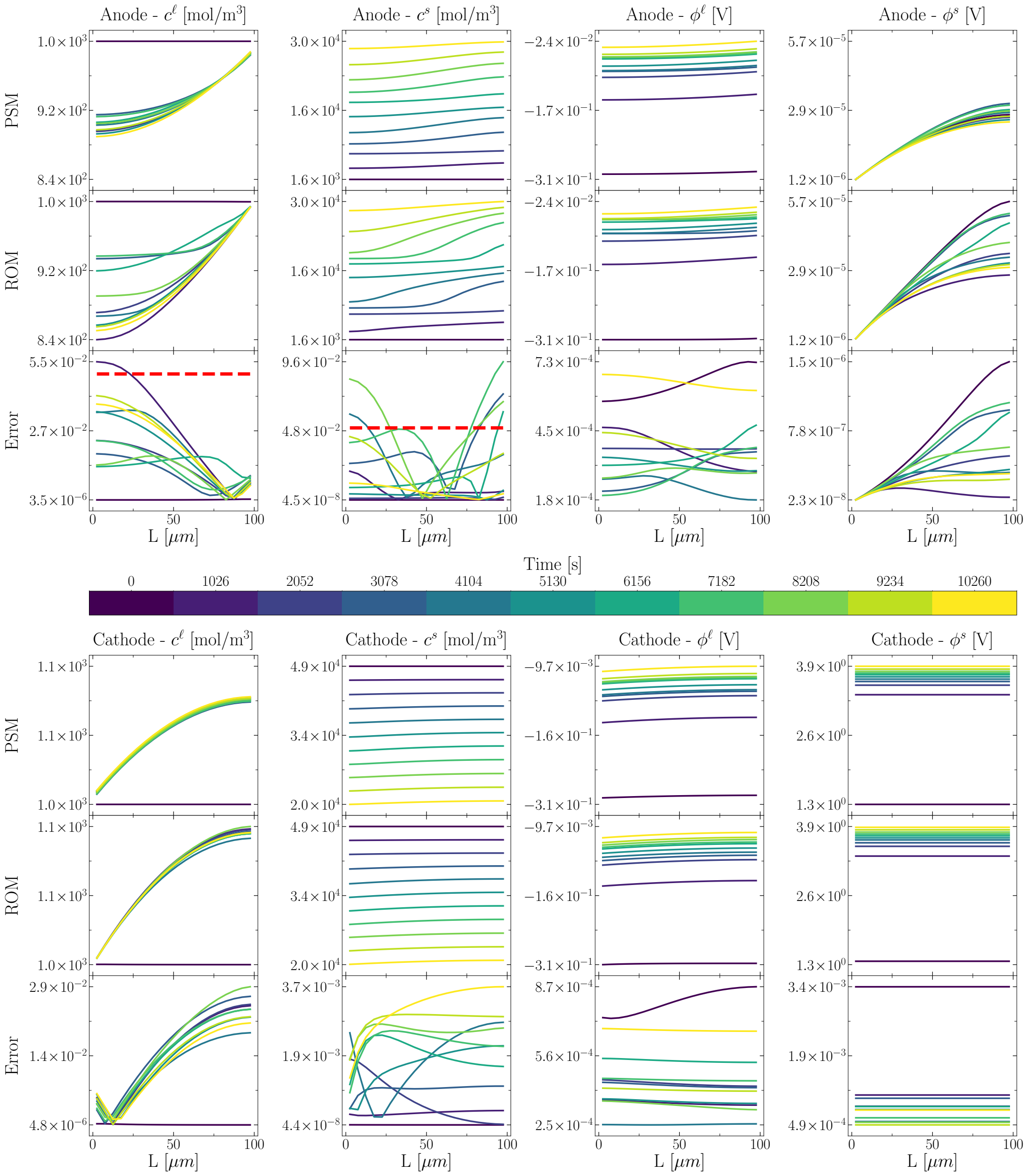

Fig. B.8 Charge at $C_{rate} = C3$. In the first row of each group of plots, the Pore Scale Model (PSM) is presented, then, in the second one, there is the Reduced Order Model (ROM), and finally the Error between the two methods.

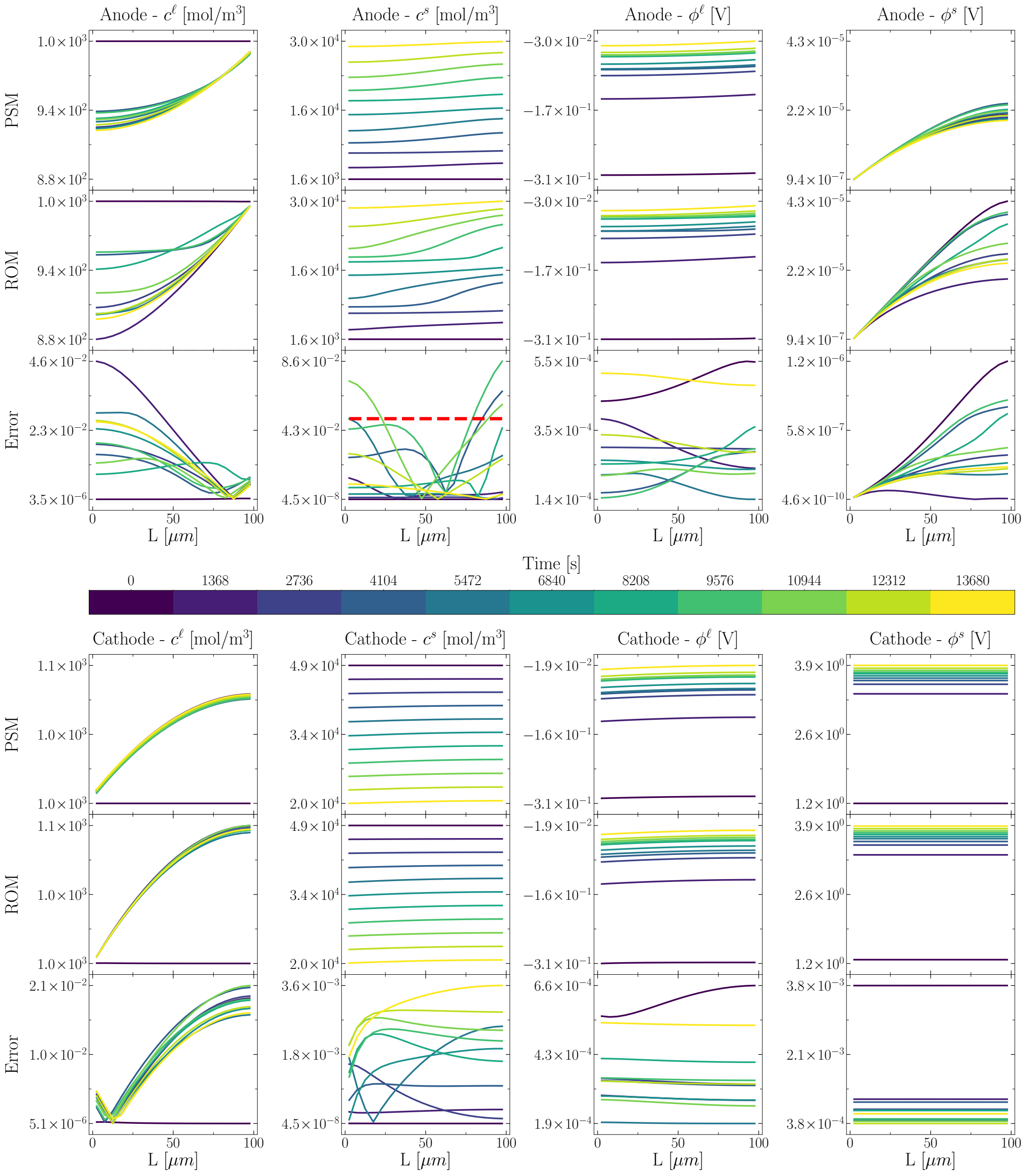

Fig. B.9 Charge at $C_{rate} = C4$. In the first row of each group of plots, the Pore Scale Model (PSM) is presented, then, in the second one, there is the Reduced Order Model (ROM), and finally the Error between the two methods.

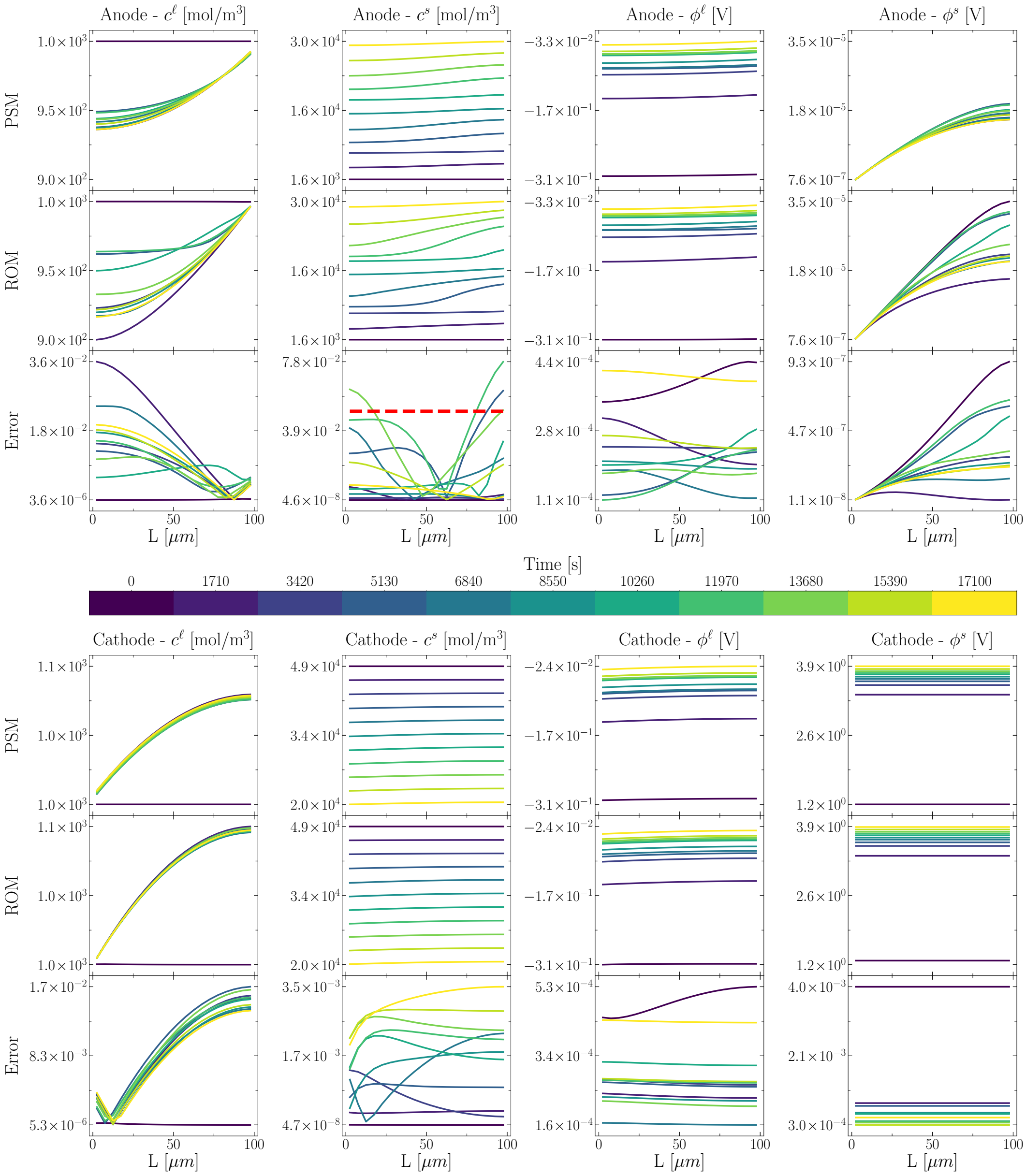

Fig. B.10 Charge at $C_{rate} = C5$. In the first row of each group of plots, the Pore Scale Model (PSM) is presented, then, in the second one, there is the Reduced Order Model (ROM), and finally the Error between the two methods.

Da=5

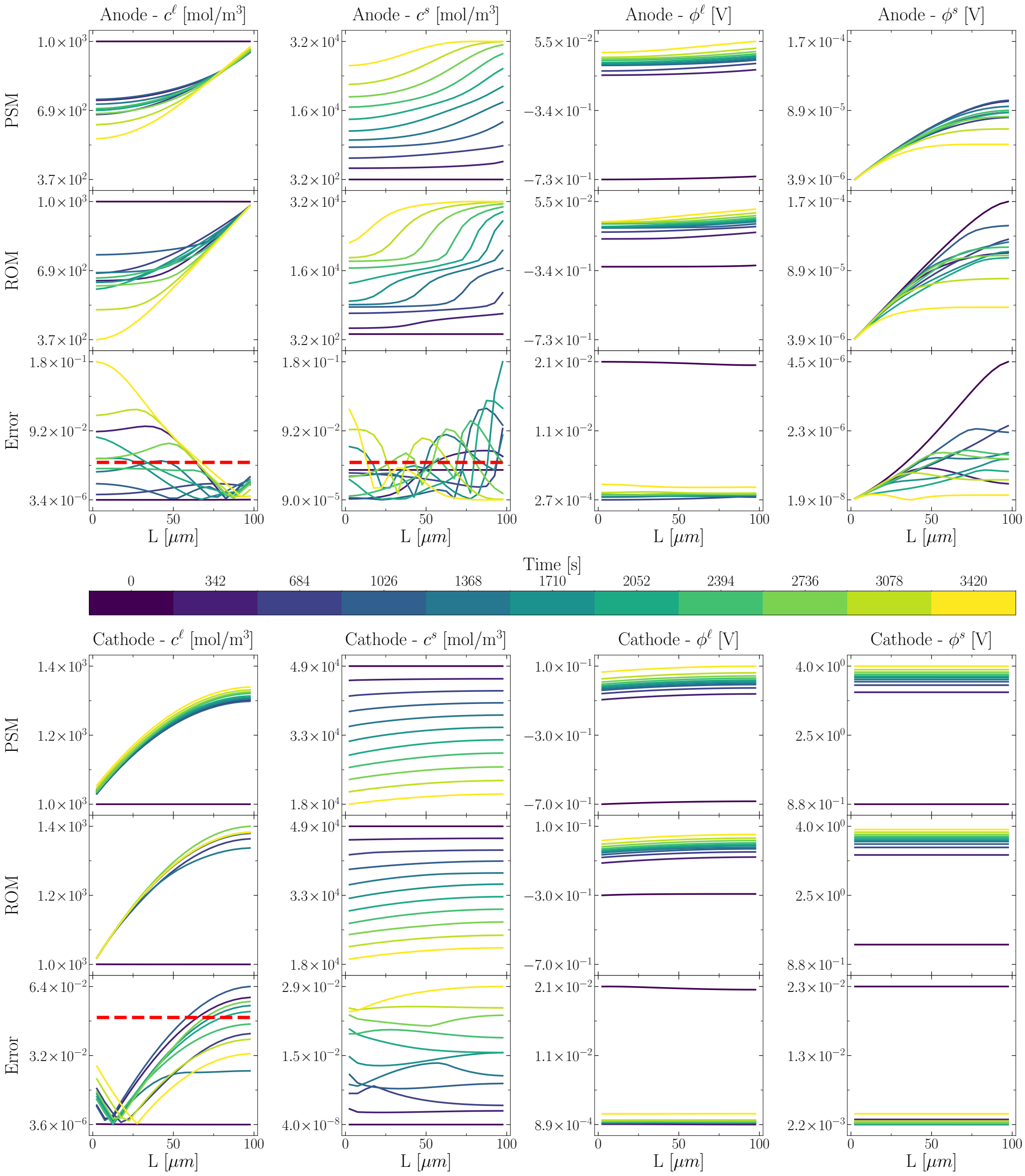

Fig. B.11 Charge at $C_{rate} = 1C$. In the first row of each group of plots, the Pore Scale Model (PSM) is presented, then, in the second one, there is the Reduced Order Model (ROM), and finally the Error between the two methods.

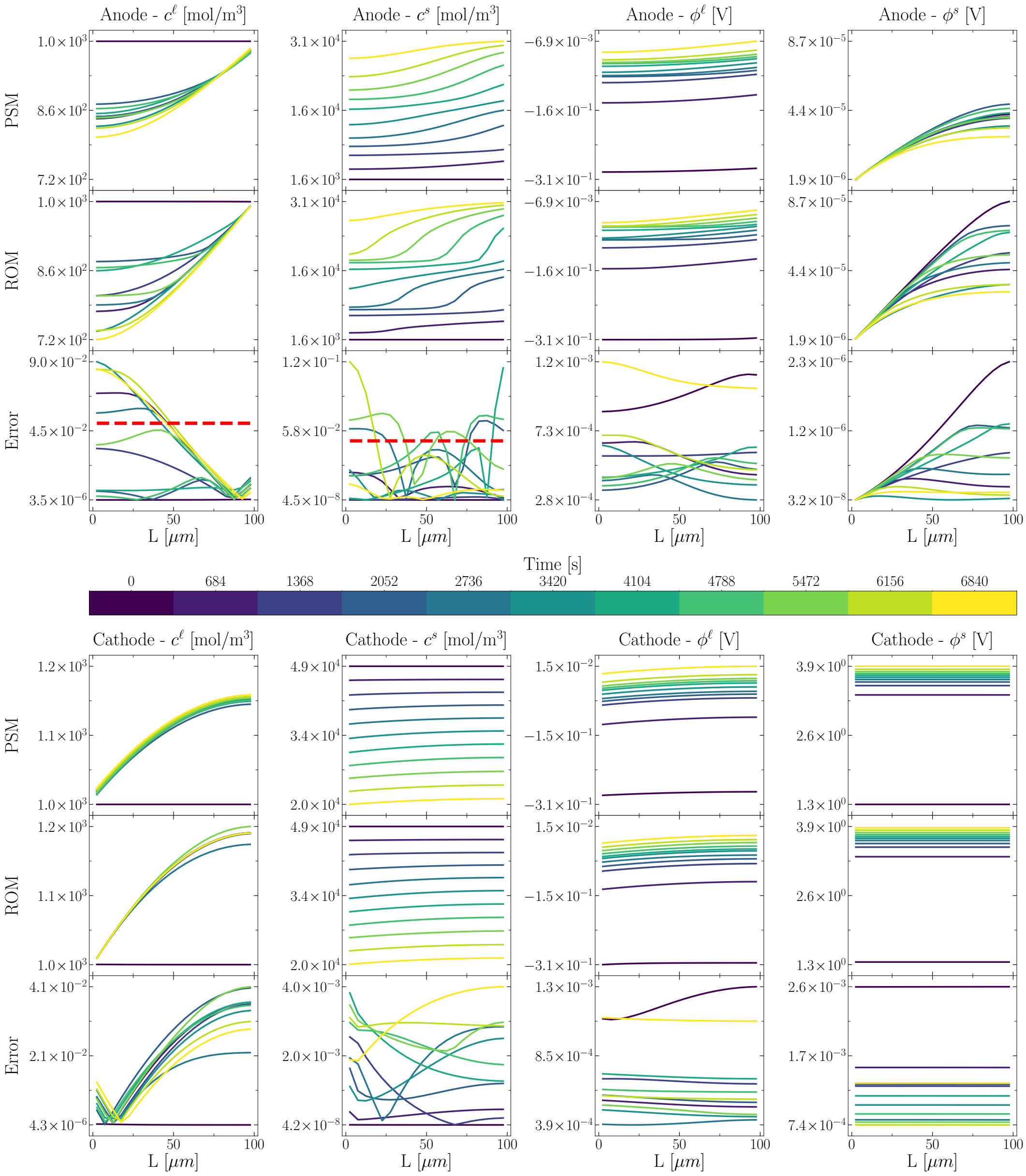

Fig. B.12 Charge at $C_{rate} = C2$. In the first row of each group of plots, the Pore Scale Model (PSM) is presented, then, in the second one, there is the Reduced Order Model (ROM), and finally the Error between the two methods.

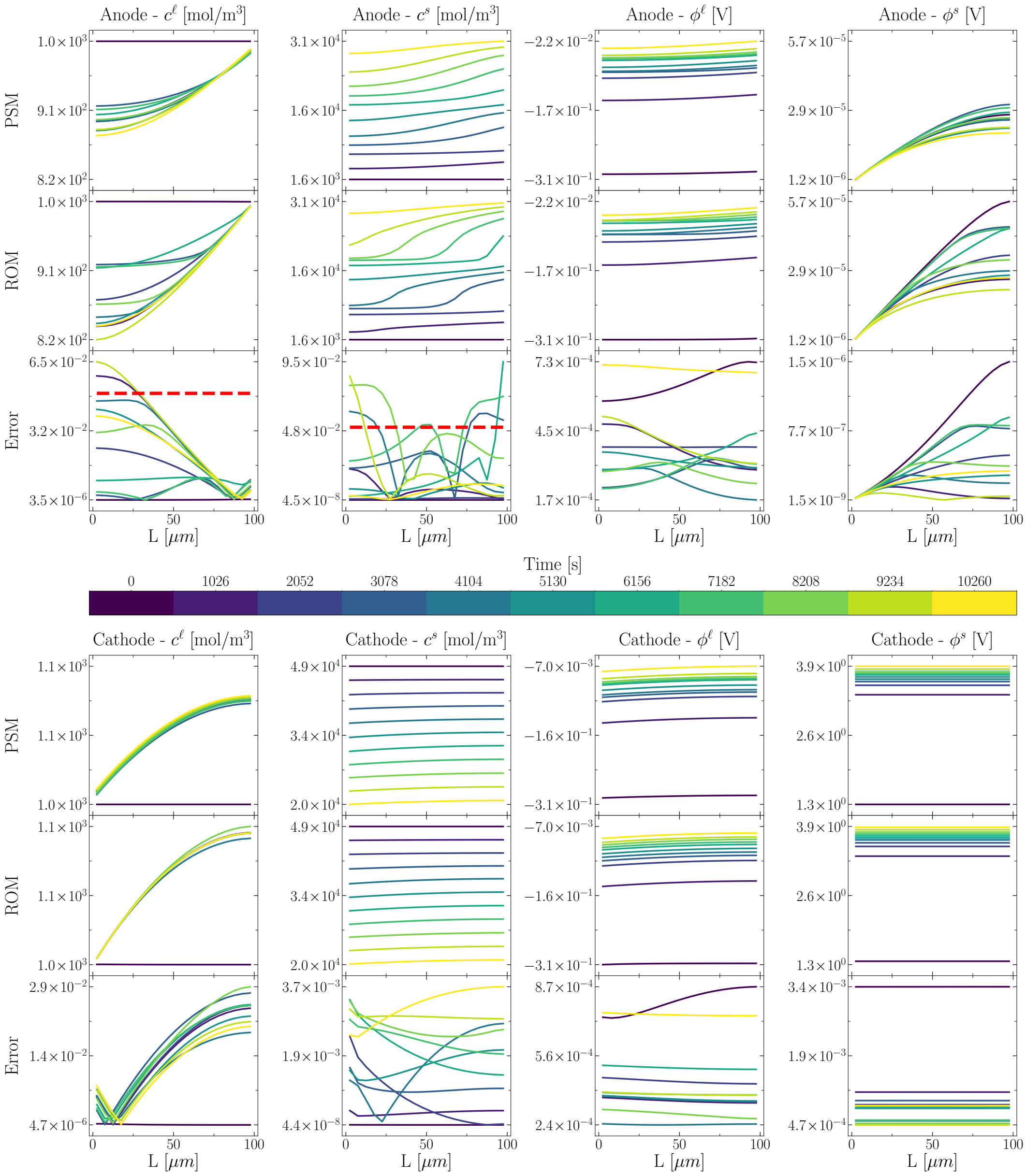

Fig. B.13 Charge at $C_{rate} = C3$. In the first row of each group of plots, the Pore Scale Model (PSM) is presented, then, in the second one, there is the Reduced Order Model (ROM), and finally the Error between the two methods.

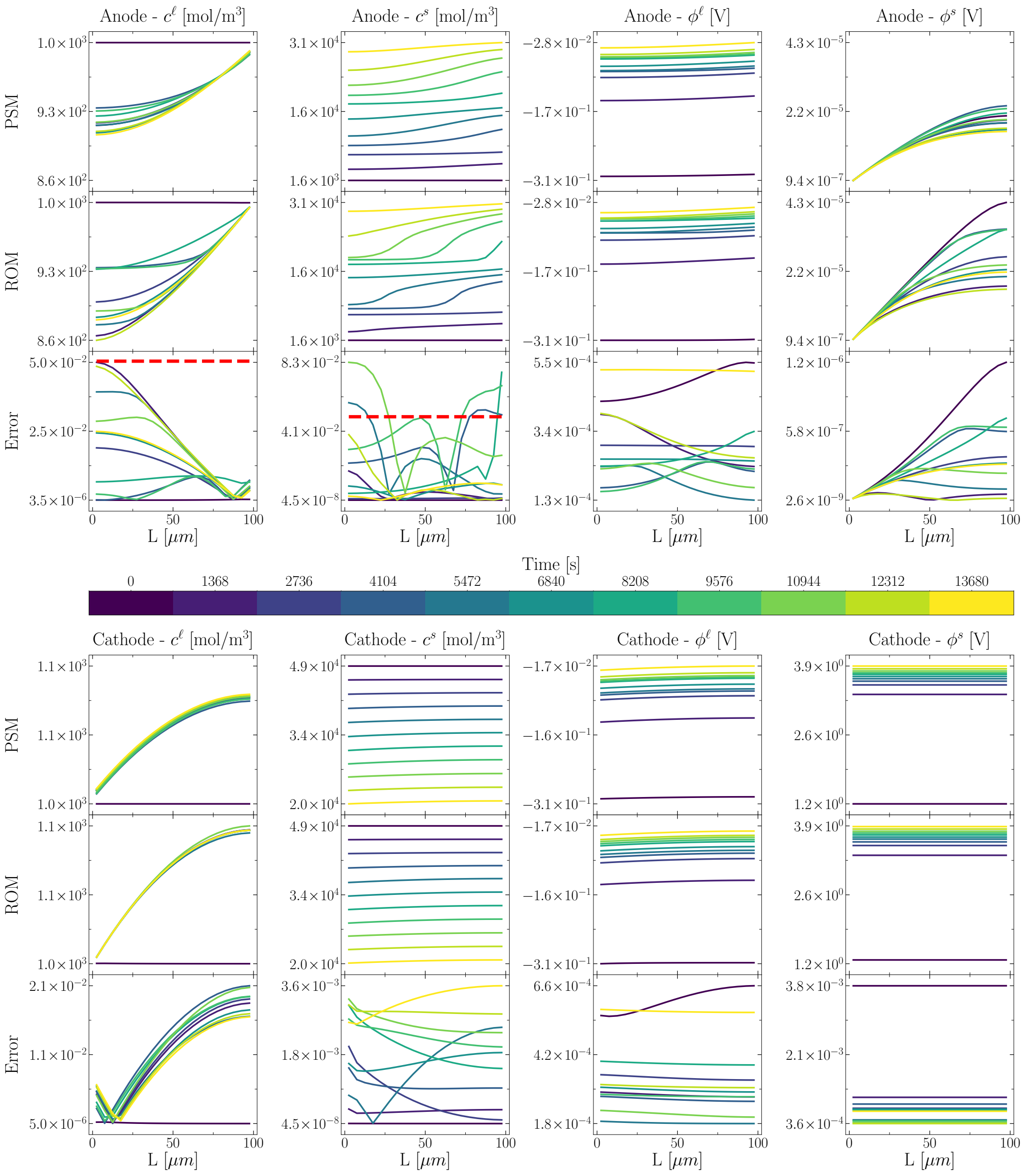

Fig. B.14 Charge at $C_{rate} = C4$. In the first row of each group of plots, the Pore Scale Model (PSM) is presented, then, in the second one, there is the Reduced Order Model (ROM), and finally the Error between the two methods.

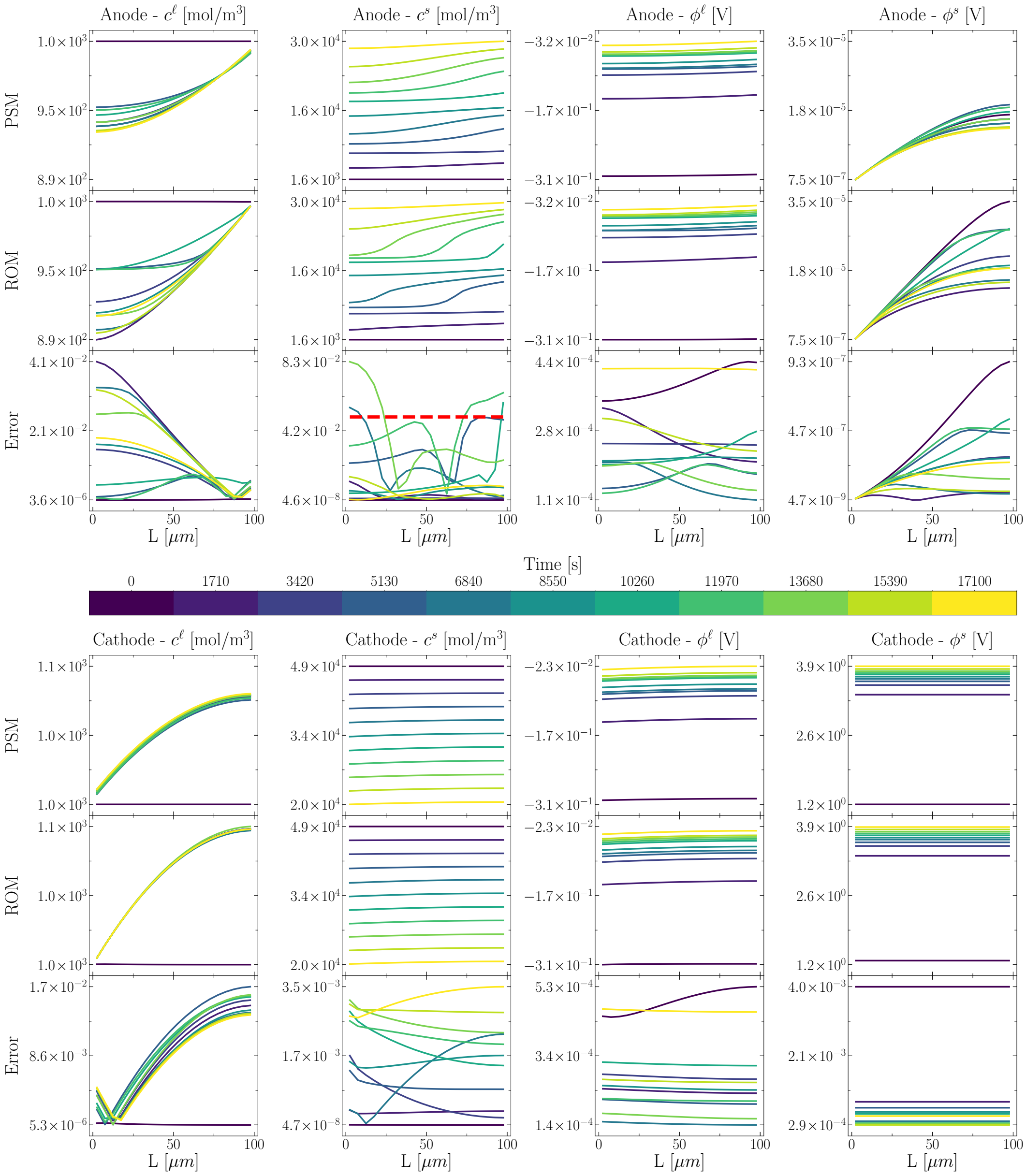

Fig. B.15 Charge at $C_{rate} = C5$. In the first row of each group of plots, the Pore Scale Model (PSM) is presented, then, in the second one, there is the Reduced Order Model (ROM), and finally the Error between the two methods.